Investigation of Capacitive-Sharing Pixel Micromegas Detectors



Master Thesis at the Faculty of Physics at the Ludwig-Maximilians-University Munich

submitted by

Nirmal Renji Mathew

born in Thiruvalla

Munich, September 15th, 2025

Charakterisierung von Capacitiv-Sharing-Pixel Micromegas Detektoren



Masterarbeit der Fakultät für Physik der Ludwig-Maximilians-Universität München

vorgelegt von

Nirmal Renji Mathew

geboren in Thiruvalla

München, den 15. September 2025

Abstract

Micro-MEsh GAseous Structure (Micromegas) detectors are Micro Pattern Gaseous Detectors (MPGD's) used for their high-rate capability and excellent spatial resolution achieved through a narrow amplification gap and fine strip/pixel pitch readouts. However, this performance comes at the expense of requiring a large number of readout channels for individual strips/pixels, which makes it more costly and power-intensive. The development and testing of large-sized pixels are investigated, which leverage charge-sharing principles across multiple pixel layers, an alternative to strip-based readouts in Micromegas, to strongly reduce the number of readout channels. Each successive layer is designed with larger pixels twice the size of the ones below, culminating in a final layer that aggregates charge information to determine the particle hit position. This approach reduces the number of readout channels while maintaining comparable spatial resolution.

The unique position reconstruction capability of the charge-sharing mechanism, through geometric charge distribution patterns, was validated through simulations.

Furthermore, two detector prototypes were investigated: a five-layer detector (PAD5) and a three-layer hybrid detector (PADH) with novel strip-like readouts. The detectors were optimized with ⁵⁵Fe X-ray source and were systematically studied using 120 GeV muons at the H4 beam line at CERN's SPS and the results are discussed.

Contents

1	Intr	roduction and Motivation		1
	1.1	Gaseous Detectors		1
	1.2	Applications of Micro-Pattern Gaseous Detectors		2
		1.2.1 High Energy Physics		2
		1.2.2 Medical Physics		3
	1.3	Motivation		3
2	The	eoretical Background		5
	2.1	Particle Photon Interaction with Matter		5
		2.1.1 Charged Particles		5
		2.1.2 Photons		8
	2.2	Charge Separation, Transport and Amplification		10
		2.2.1 Electron Drift		10
		2.2.2 Ion Drift		11
		2.2.3 Gas Amplification		12
3	Mic	cromegas Detectors		15
•	3.1	Resistive Micromegas		15
	3.2	Anode readout configurations		15
	0.2	3.2.1 Strip Readout		16
		3.2.2 Pixel Readout		17
	3.3	Capacitive-Sharing Pixel Micromegas Detector		18
	0.0	3.3.1 Readout Configurations		20
4	Evr	perimental Techniques		25
-	4.1	Scalable Readout System (SRS)		25
	4.2	Signal Reconstruction		28
	4.3	Cluster Building		28
	4.3	Track Reconstruction		30
	4.4			30
		8		
		4.4.2 Detector Alignment		31
				31 33
		4.4.4 Detector Rotations		- 33

vi Tabellenverzeichnis

	4.5	Spatial Resolution Determination	
		4.5.1 Residual Analysis	
	4.6	Inclined Track Reconstruction	
		4.6.1 Detection Efficiency	7
5	Sim	lation of Charge Sharing Concept 39	9
	5.1	Charge Sharing	9
	5.2	Simulation Framework	0
		5.2.1 Charge Deposition Model	1
		5.2.2 Charge Propagation Algorithm	1
		5.2.3 Position Reconstruction	1
	5.3	Simulation Results	1
		5.3.1 Single Pixel Performance	2
		5.3.2 Symmetric Pixel Performance	2
		5.3.3 Gaussian Distribution Performance	6
		5.3.4 Noise Profile	
		5.3.5 Gaussian Distribution with Noise	
	5.4	Conclusion	
6	Cha	acterization with ⁵⁵ Fe source and Cosmic Muons 55	
	6.1	Characterization with $^{55}\mathrm{Fe}$	
		5.1.1 Measurement Setup	7
		6.1.2 PADH	7
		6.1.3 PAD5	0
		$6.1.4$ X-Ray imaging with 55 Fe	1
	6.2	Hit Multiplicity with $^{55}\mathrm{Fe}$ $$	4
	6.3	Characterization with Cosmic Muons	4
		6.3.1 Measurement Setup	5
		6.3.2 Cosmic Muon Measurements	6
7	Cha	acterization with 120 GeV Muons 73	1
•	7.1	Experimental Setup	
	7.2	Perpendicularly Incident Particles	
	1.2	7.2.1 PADH	
		7.2.2 PAD5	
	7.3	Periodic Substructures	
	7.3	Inclined incident particles	
	1.4	7.4.1 Pulse Height Analysis	
		7.4.2 Spatial Resolution	
		1	
		7.4.3 Efficiency	U
8	Sun	mary and Outlook 8'	7

Chapter 1

Introduction and Motivation

The fundamental challenge in experimental particle physics lies in the reality that, out of all the particles and bosons predicted by the Standard Model, only a handful of them are sufficiently stable or long lived to reach particle detectors to be directly detected (Navas et al. 2024; Particle Data Group et al. 2022). Even the ones that can be detected do not make it to the outer detectors in the large detector setups. The vast majority of fundamental particles like the quarks, W^{\pm} , Z^{0} , Higgs boson, decay within very short timescales making them invisible to direct observation even at relativistic speeds. This observational constraint has transformed the field of particle physics into a very sophisticated exercise in event reconstruction to the interaction point, where the existence and identification of short-lived particles must be inferred from the measurable traces they leave while traversing the detector volume. This necessitates the need for detectors capable of high position and timing precision in order to obtain precise reconstruction, which would provide insight into the underlying physics of particle interaction, decay products, and fundamental forces governing matter at the most elementary scales and hopefully into the physics beyond the standard model. Among the various detector technologies developed to meet these demanding requirements, gaseous detectors have emerged as a particularly versatile and cost-effective solution.

1.1 Gaseous Detectors

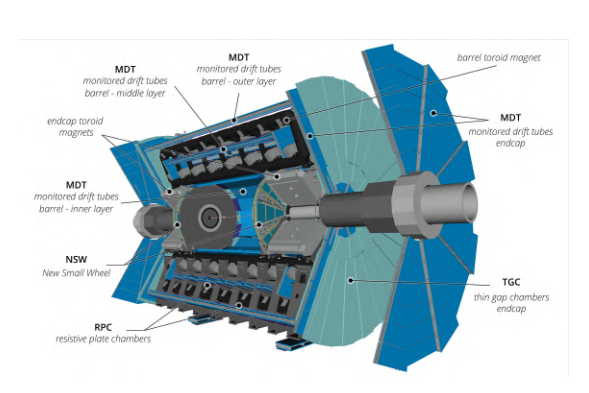
Gas detectors have played a fundamental role in particle and radiation detection systems for over a century. The fundamental principle of ionization of gas molecules by incident radiation provides a robust and versatile way of detecting radiation across a broad source of radiation types like e^{\pm} , μ^{\pm} , α , γ and so on. The unique combination of the fundamental detection capabilities when coupled with the practical advantages, gaseous detectors becomes an irreplaceable technology in the field of experimental particle physics. The ability to tune gas composition, pressure and electric field configuration allows for optimization across different radiation types and energy ranges. Whether detecting minimum ionizing particles such as muons, heavily ionizing alpha particles, or electromagnetic ra-

diation, gaseous detectors can be configured to provide optimal response characteristics (Kleinknecht 1998). This versatility extends to geometric considerations, where detector architectures can be adapted from simple cylindrical shapes to planar structures or even more complex geometries. They offer excellent scalability and remarkable flexibility in terms of detector design at very low cost, making gaseous detector one of the most affordable options for large scale experiments like ATLAS. The ever-growing demands of modern high-energy physics, experiments at energies $\mathcal{O}(10)$ TeV have led to high particle rates, radiation doses, and a need for detectors with even higher precise time and spatial resolution. This has exposed some inherent limitations that traditional wire based gaseous detectors had. This led to the development of Micro-Pattern Gaseous Detectors (MPGDs). They offer excellent spatial and temporal resolutions and high rate capabilities over their predecessors. In this thesis, MICRO MEsh GAseous Structure (Micromegas) (Giomataris et al. 1996) are studied. Among the different types of readout that Micromegas can have, the most common ones include strips or pixels (pads) printed on a supportive plate.

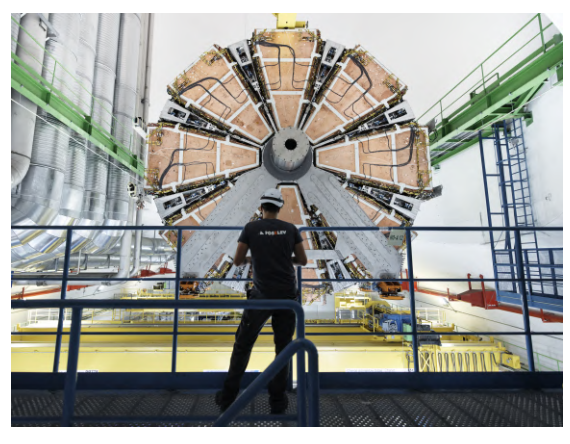
1.2 Applications of Micro-Pattern Gaseous Detectors

1.2.1 High Energy Physics

In the field of high-energy physics, MPGDs are part of large experiments like ATLAS (A Toroidal LHC Apparatus) (Collaboration 2024) and CMS (Compact Muon Solenoid) (CMS Collaboration 2008) experiments at the LHC (Large Hadron Collider)



(a) View of the multi-purpose ATLAS detector with different subsystems for detection of particle trajectories, momentum etc. Figure taken from (Collaboration 2024)



(b) New Small Wheel being lowered into the ATLAS experiment. The wheel is 10m in diameter. The beam pipe is also visible. Figure taken from (Brice et al. 2021).

In the phase 1 upgrade of ATLAS, the New Small Wheel (NSW) was installed (Kawamoto et al. 2013). The NSW includes the Micromegas detector spanning several square meters. Figure 1.1b shows the NSW, with a diameter of 10 m. This illustrates the importance of the scalability of detectors.

1.3 Motivation 3

1.2.2 Medical Physics

MPGD's are also used in ion and X-ray based radiography (Gutierrez et al. 2012) owing to their excellent spatial resolution, high rate capability and sensitivity towards charged ions. Since treatment methods like ion therapy can induce radiation damage to cells, it is important to constantly monitor the treatment. This again requires scaling up the detectors to large sizes at low costs while maintaining good precision which makes MPGDs a good candidate.

1.3 Motivation

The demands of modern particle physics experiments for improved spatial resolution and higher rate capabilities have driven the development of pixelated detector systems. However, finer granularity poses a fundamental challenge: the number of readout channels scales quadratically with detector area when maintaining constant pixel size, leading to exponential growth in readout electronics, power consumption, and cost. To address this critical limitation, a novel detector architecture has been developed that fundamentally decouples spatial resolution from channel count. The capacitive-sharing pixel Micromegas detectors concept introduces a multi-layered charge-sharing architecture that maintains the fine granularity of micro-pixels for charge collection while dramatically reducing the number of required readout channels. The fundamental advantage of this approach lies in its ability to encode charge signals into fewer channels. This thesis presents a comprehensive investigation of capacitive-sharing pixel Micromegas detectors, focusing on the systematic characterization of their spatial resolution capabilities and detection efficiency performance.

Chapter 2

Theoretical Background

2.1 Particle Photon Interaction with Matter

The physics of particles and photons in a detector is dictated by their interaction with the detector's active medium. According to contemporary models of particle physics, the interactions of particles and photons with matter are governed by the four fundamental forces: electromagnetic, weak nuclear, strong nuclear and gravitational forces. However, for charged particle and photon detection in gaseous media, the electromagnetic interaction dominates due to its significantly larger cross-section compared to the other fundamental interactions, which can therefore be neglected in this context.

2.1.1 Charged Particles

1

Within electromagnetic interactions, several distinct processes must be considered. Five primary interaction mechanisms are relevant for charged particles traversing gas detector media: excitation, ionization, bremsstrahlung, Cherenkov radiation and transition radiation. The photon absorption ionization model by Allison and Cobbs allows calculation of the mean energy loss of charged particles starting from the interaction of virtual photons in matter (Allison et al. 1980). This gives the Bethe Bloch formula for heavy charged particles (Particle Data Group et al. 2022).

$$-\left\langle \frac{dE}{dx} \right\rangle = 4\pi N_A r_e^2 m_e c^2 z^2 \frac{Z}{A} \frac{1}{\beta^2} \left(\frac{1}{2} \ln \frac{2m_e c^2 \beta^2 \gamma^2 T_{\text{max}}}{I^2} - \beta^2 - \frac{\delta(\beta \gamma)}{2} \right) \tag{2.1}$$

 $10^{-1}N_A$ the Avogadro's number, r_e the classical electron radius, m_e the electron mass, c the speed of light, c the charge number of the incident particle, c the atomic number of the absorber, c the particle velocity c divided by the speed of light c, c the Lorentz factor c = $\frac{1}{\sqrt{1-\beta^2}}$, r $\frac{1}{10^{-1}}$, r $\frac{1}{10^{-1}}$ the maximum possible energy that can be transferred to an electron in a single collision, r the mean excitation energy and r $\delta(\beta \gamma)$ the Fermi density effect correction to ionization energy loss (Fermi 1940).

The mean energy loss $\frac{1}{\rho} \left\langle \frac{dE}{dx} \right\rangle$ of muon in copper is shown as a function of $\beta\gamma$ in Figure 2.1. Four distinct regions can be observed. The mean energy loss falls off as $\frac{1}{\beta^2}$ for $\beta\gamma \leq 1$. Energy loss is minimum for $2 \leq \beta\gamma \leq 8$. The particles that populate this region are called Minimum Ionizing Particles (MIP). The mean energy loss of MIP is in the order of 2–3 MeVcm² g⁻¹ for almost all materials. The collision energy loss described by the Bethe-Bloch formula exhibits a logarithmic rise proportional to $\ln(\beta^2\gamma^2)$ before reaching a plateau region for highly relativistic particles. But radiative energy loss mechanisms dominate at very high energies, causing the total energy loss to rise approximately linearly with energy, which can be seen towards the end of Figure 2.1. At the critical energy $E_{\mu c}$, radiative energy losses and ionization effects are equal. For low-energy particles with $\beta\gamma \lesssim 0.1$, the Bethe-Bloch formula (equation (2.1)) becomes invalid as shell corrections accounting for atomic binding effects become significant.

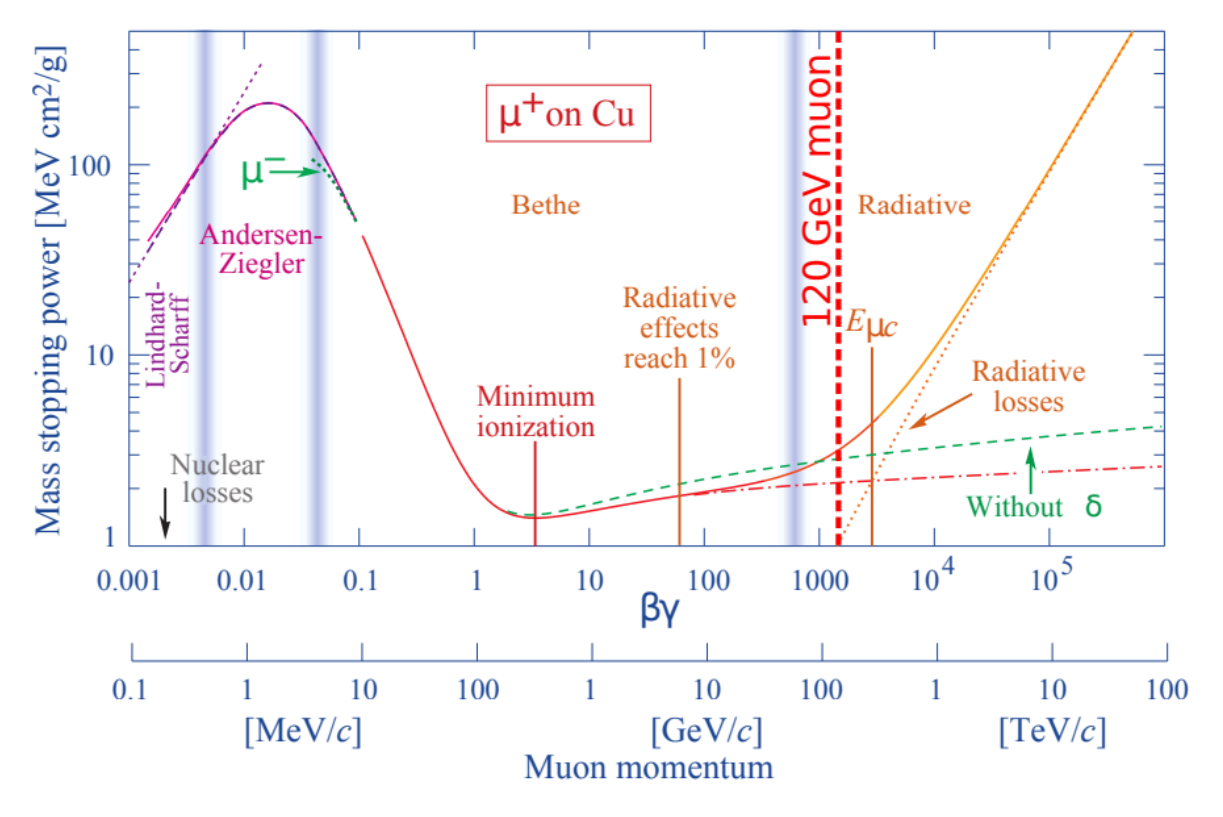


Figure 2.1: Mean energy loss per unit density $\frac{1}{\rho} \left\langle \frac{dE}{dx} \right\rangle$ for muons in copper as a function of $\beta \gamma$.

The central limit theorem predicts that energy loss should follow a Gaussian distribution when particles undergo many independent collision events. However, in thin detector media, the observed energy loss distribution deviates significantly from a purely Gaussian form due to the limited number of collision events and the discrete nature of energy transfer processes (Sjue et al. 2017). The asymmetric distribution arises primarily from rare,

high-energy collisions that produce δ -electrons—energetic secondary electrons that are capable of inducing additional ionization events. These infrequent but high-energy transfers create an extended tail toward higher energy losses, resulting in a characteristic asymmetric distribution where the arithmetic mean exceeds the most frequently observed value.

For such thin detector configurations, Landau's theoretical framework provides a more accurate description by focusing on the most probable energy loss rather than the mean (Beringer et al. 2012). The most probable energy loss $\left(\frac{\Delta E}{\Delta x}\right)_p$ corresponds to the peak of the energy loss distribution and represents the value most commonly observed experimentally. As detector thickness increases, the collision events increase, and the energy loss distribution gradually approaches the Gaussian limit predicted by the central limit theorem. In this thick detector regime, the most probable energy loss converges toward the mean energy loss described by the Bethe-Bloch formula.

Some tx	mical	detector	gases	and	their	properties	are	shown	in	Table 2.1
DOME U	picai	actedor	Sanco	and	ULICII	properties	αr	DIIOWII	111	10010 2.1

Gas	ρ	$E_{\mathbf{x}}$	$\mathrm{E_{I}}$	$W_{\rm I}$	$dE/dx _{min}$	N_{P}	N_{T}
	$[\mathrm{mg}\ \mathrm{cm}^{-3}]$	[eV]	[eV]	[eV]	$[{ m keV~cm^{-1}}]$	$[\mathrm{cm}^{-1}]$	$[\mathrm{cm}^{-1}]$
He	0.179	19.8	24.6	41.3	0.32	3.5	8
Ne	0.839	16.7	21.6	37	1.45	13	40
Ar	1.66	11.6	15.7	26	2.53	25	97
Xe	5.495	8.4	12.1	22	6.87	41	312
CO_2	1.84	7.0	13.8	34	3.35	35	100
CF_4	3.78	10.0	16.0	35 - 52	6.38	52 - 63	120
iC_4H_{10}	2.49	6.5	10.6	26	5.67	90	220

Table 2.1: Properties of common detector gases. ρ (gas density), E_x and E_I (first excitation and ionization energies), W_I (mean energy required to produce one electron-ion pair), $\left(\frac{dE}{dx}\right)_{\min}$ (minimum differential energy loss for MIPs), and N_P and N_T (primary and total electron-ion pairs generated per cm by minimum ionizing particles). Values correspond to standard conditions of 20°C and 1013 mbar. Data adapted from (Particle Data Group et al. 2022)

As particles move beyond the minimum ionizing region of the Bethe-Bloch curve and reach increasingly relativistic velocities, an additional electromagnetic phenomenon becomes relevant: Cherenkov radiation. This effect occurs when a charged particle traverses a dielectric medium with a velocity v exceeding the phase velocity of light in that medium, c/n, where n is the refractive index (Čerenkov 1937). The threshold condition for Cherenkov emission is thus

$$\beta \ge \frac{1}{n} \tag{2.2}$$

Above this threshold, the charged particle polarizes the medium along its trajectory, creating molecular dipoles whose electric fields sum coherently to produce electromagnetic radiation. This coherent emission occurs because the particle effectively "outruns" its own electromagnetic field in the medium. The radiation is emitted in a characteristic cone with half-angle θ_C given by

$$\cos \theta_C = \frac{1}{(\beta n)} \tag{2.3}$$

forming a wavefront that propagates at an angle θ_C relative to the particle's direction.

2.1.2 Photons

Unlike the continuous energy loss mechanism in charged particles through multiple minor collisions, photons either traverse the material unperturbed or are completely removed from their original trajectory upon interaction. The interaction of photons in matter, based on their energy, occurs in three different ways: photoelectric effect, compton scattering and pair production. This discrete interaction behavior results in an exponential attenuation of the photon beam intensity. For a monoenergetic narrow photon beam with initial intensity I_0 traversing a material of thickness d, the transmitted intensity I follows the Beer-Lambert law (Leo 1994):

$$I(x) = I_0 exp(-\mu d) = I_0 exp(\frac{-\mu}{\rho}x)$$
(2.4)

where ρ is the density, $x := d\rho$ is the mass thickness, and μ/ρ is the mass attenuation coefficient of the material. The mass attenuation coefficient μ/ρ as a function of the photon energy E_{γ} is shown in the Figure 2.2

At low energies, $E_{\gamma} < 100$ KeV, the photoelectric effect dominates. A photon of energy E_{γ} is absorbed by an atom, and a shell electron of energy $T_{\rm e}$ is emitted, where

$$T_e = E_{\gamma} - E_b \tag{2.5}$$

where E_b is the binding energy of the electron. When the ejected photoelectron originates from an inner atomic shell, the atom remains in an excited state following the photoelectric interaction. The atom subsequently de-excites through the emission of characteristic X-rays or Auger electrons with total energy approximately equal to the binding energy E_b of the original shell.

In gas detectors, if the photoelectric interaction occurs within the active volume and the detector is sufficiently thick to absorb the subsequent de-excitation photons, the entire incident photon energy is deposited and detected. This complete energy deposition makes the photoelectric effect particularly valuable for photon spectroscopy applications. The photoelectric cross-section exhibits a strong dependence on the atomic number Z of the absorbing material:

$$\sigma_{\rm photo} \propto Z^5$$
 (2.6)

This pronounced Z-dependence enables the use of high-Z noble gases in gaseous photon detectors to significantly enhance detection efficiency compared to lower-Z alternatives (Kleinknecht 1998).

Compton effect is the inelastic scattering of photons on a quasi-free electron while transferring part of the energy it possesses. This transfer of energy can be calculated through the conservation laws of energy and momentum. The corresponding energies are given by Equation 2.7 and Equation 2.8 (Kleinknecht 1998).

$$E_{\gamma}' = \frac{E_{\gamma}}{1 + \frac{E_{\gamma}}{m_e c^2} (1 - \cos \Theta)} \tag{2.7}$$

$$T'_{e} = \frac{E_{\gamma}^{2}}{m_{e}c^{2}} \cdot \frac{1 - \cos\Theta}{1 + \frac{E_{\gamma}}{m_{e}c^{2}}(1 - \cos\Theta)}$$
 (2.8)

When $\Theta = 0^{\circ}$, no energy is transferred between the photon and the electron. When $\Theta = 180^{\circ}$, the photons are backscattered and the maximum transfer of energy occurs between the photon and the electron. The sharp cutoff at the maximum is called the compton edge. For photon energies above $E_{\gamma} > 2m_e c^2$, the photon can annihilate into

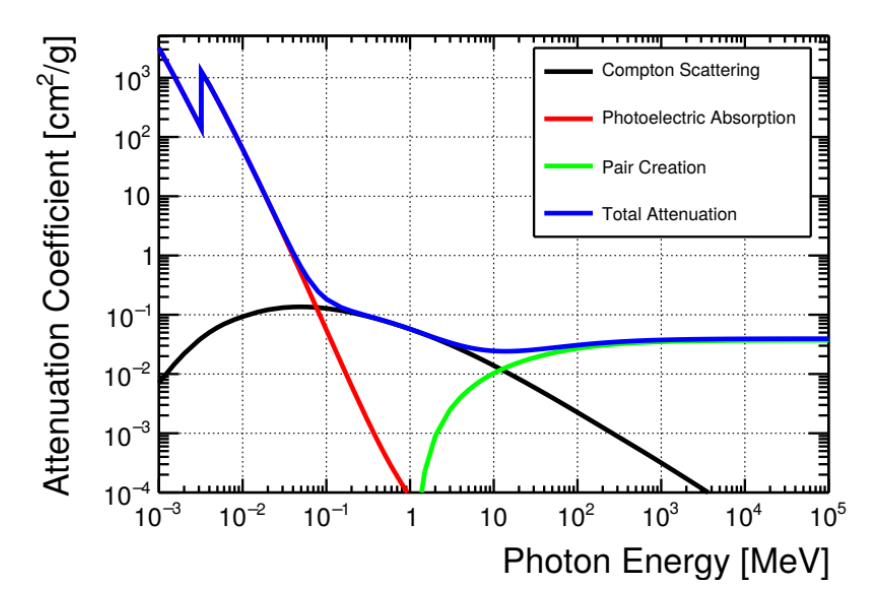


Figure 2.2: Total attenuation coefficient for different photon energies in Argon (blue line). photoelectric absorption (red), compton scattering (black), and pair production (green) are drawn separately, showing their dominating energy ranges. Data taken from XCOM database(Berger M.J. 2010).

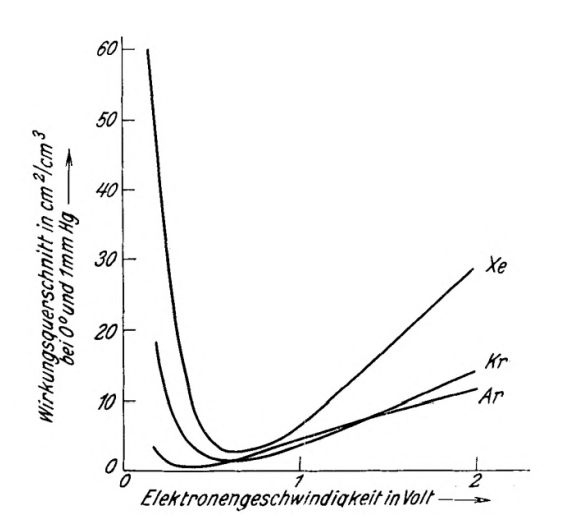
an electron-positron pair, in the vicinity of a third body, usually the nucleus, to conserve energy and momentum simultaneously. This process is called nuclear pair production.

When the third body is an electron, it is called an electron pair production. In Figure 2.2, it can be seen that pair production becomes the dominant process above $E_{\gamma} > 10$ MeV.

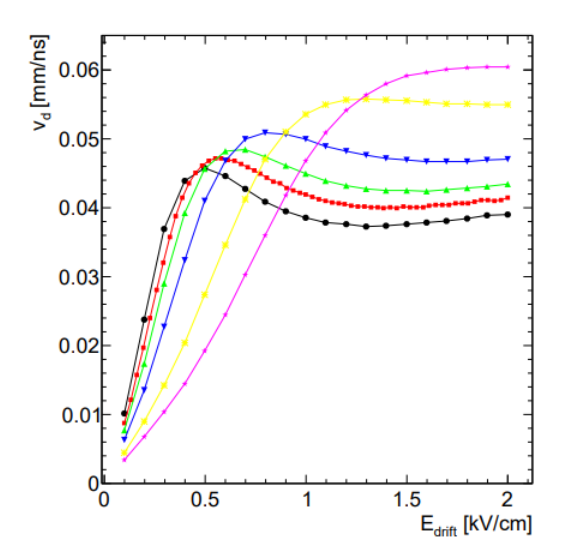
2.2 Charge Separation, Transport and Amplification

The electron ion pairs that are produced through the production mechanisms described in the sections above are measured as a signal. But this requires that the charges that are produced are not recombined prior to the measurement. So the electron-ion pairs are subject to an electric field under which the charges drift, without recombination. The mechanism by which this is precisely done in Micromegas will be discussed in chapter 3. The initial electron-ion pairs that are produced cannot be directly measured, as they are too few in number. The charges are thus amplified through the process of Townsend amplification. The physical details of the above-mentioned process will be discussed in the following sections.

2.2.1 Electron Drift



(a) Energy dependency of the elastic scattering cross-section of electrons in different noble gases. Graphic taken from (Ramsauer et al. 1929).



(b) Electron drift velocity as a function of the electric drift field for various $Ar:CO_2$ gas mixtures at 20°C and 1013 mbar, Fig from (Bortfeldt 2014).

In the absence of a magnetic field, the electrons follow the field lines and are accelerated within the mean free path. At energies of a few eV, de Broglie wavelength of electrons becomes comparable to their atomic dimensions. At these scales, electrons should be treated as waves rather than classical particles. This leads to quantum interference effects - the electron wave can interfere constructively or destructively with itself as it scatters

off atoms. This is the Ramsauer effect, which causes the scattering cross-section to vary dramatically with electron energy, creating the characteristic minimum leading to a maxima in the drift velocity (Kleinknecht 1998). In Figure 2.3a, the characteristic minimum in the scattering cross-section can be observed, leading to the local maxima that can be seen in Figure 2.3b. This effect leads to large variations in the interaction cross sections of the electron with gases. Furthermore, slight changes in the gas compositions lead to a huge effect in the electron cross-sections, and by extension, the drift velocities. This effect is highly used in choosing the composition of gases in a gas detector, depending on the requirements of the detector.

Polyatomic gases, like CO_2 and C_4H_{10} , in addition to modifying the drift properties, can also act as quenching gases. They absorb photons that are emitted with the recombination of electrons with the noble gas ions. This absorption takes place through the excitation of rotational and vibrational states that they poses due to extra degrees of freedom. As a result, they prevent discharges in the detector from photon induced ionization (Leo 1994).

2.2.2 Ion Drift

Ions drift under the same electric field the electrons experience. But because of the higher mass and the shorter mean free path, ions experience less acceleration under the electric field. Furthermore, ions have less mobility compared to electrons. This makes it easier to describe the ion transport, unlike the complicated dynamics of electron transport (Grupen et al. 2008).

$$\vec{v}_{\rm ion} = \mu_{\rm ion} \vec{E} \frac{p_0}{p} \tag{2.9}$$

Where \vec{v}_{ion} is the ion drift velocity and μ_{ion} is the gas-dependent ion mobility that exhibits constant behavior over an extensive electric field range and are not strongly influenced by the admixture of molecular gases. \vec{E} denotes the electric field, p is the actual pressure and p_0 is 1 Bar, which is the value of pressure at NTP.

Mobilities for ions of type $i(\mu_i)$ in compound gas mixtures can be calculated using

$$\frac{1}{\mu_i} = \sum_{k=1}^n \frac{c_k}{\mu_{ik}} \tag{2.10}$$

with c_k being the concentration of a gas k and μ_{ik} being the mobility of the ions of type i in the gas of type k (Kleinknecht 1998).

Typical ion mobilities for some gases are given in Table 2.2

Gas	Ion	$\mu \ [\mathrm{cm^2 V^{-1} s^{-1}}]$
Ar	Ar^{+}	1.7
Ar	$iC_4H_{10}^+$	1.56
Ar	CO_2^+	1.72
iC_4H_{10}	$iC_4H_{10}^+$	0.61
CO_2	CO_2^+	1.09

Table 2.2: Ion mobility in gases (Kleinknecht 1998))

2.2.3 Gas Amplification

The electrons produced through the interaction mechanisms discussed in the section 2.1, are finally measured as signals in MicroMegas detectors. But these charges need to be amplified significantly in order to be seen by the electronics. This is achieved through gas amplification under very high electric fields $\mathcal{O}(10\text{--}100 \text{ keV cm}^{-1})$. Under these high electric fields, electrons gain enough kinetic energy between collisions with gas atoms to further ionize other gas atoms to create more electron-ion pairs by impact ionization. This process repeats for each newly generated secondary electron, subsequently producing additional electrons and forming an electron avalanche (Townsend 1910). During this multiplication process, the number of electrons N(x) experiences an incremental increase dN over an infinitesimal drift distance dx, described by the differential equation:

$$dN = N(x)\alpha(x)dx \tag{2.11}$$

where α represents the first Townsend coefficient. The coefficient α quantifies the ionization probability per unit path length and is formally defined as $\alpha = 1/\lambda$, where λ denotes the mean free path of an electron.

The solution to this differential equation yields the total electron population as:

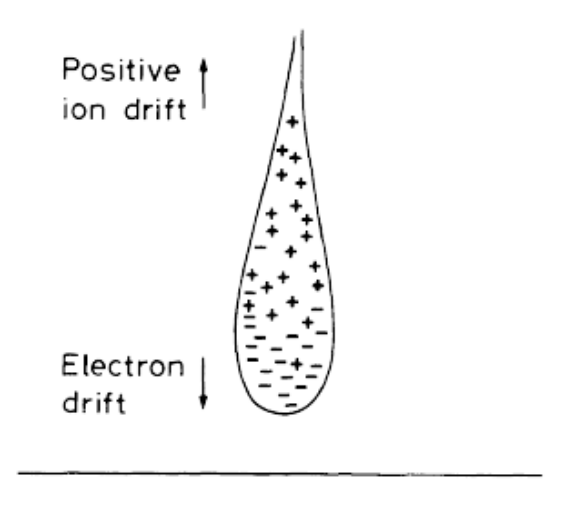
$$N = N_0 \exp\left(\int \alpha(x) \, dx\right) \tag{2.12}$$

where N_0 represents the number of initial electrons and $\alpha(x)$ is the position-dependent Townsend coefficient, which exhibits a functional dependence on both the local electric field strength and the gas composition and density.

The first Townsend coefficient can be parameterized through the empirical relation given by Korf (Townsend 1910):

$$\alpha(|\vec{E}|) = \frac{Ap}{T} \exp\left(-\frac{Bp}{|\vec{E}|T}\right) \tag{2.13}$$

where $A_0 = k_B A$ and $B_0 = k_B B$ represent gas-dependent empirical parameters, with k_B denoting the Boltzmann constant. The parameters A and B are material-specific constants that characterize the ionization properties of the particular gas medium.



Anode Wire

Figure 2.4: Droplet-shaped avalanche charge distribution near a thin anode wire. High-mobility electrons concentrate near the wire (bottom), while low-mobility positive ions form the broader droplet shape. Figure taken from (Leo 1994)

Using Equation 2.12 and Equation 2.13 the gas gain is expressed as:

$$G = \exp\left[\frac{Ap}{T}\exp\left(-\frac{Bp}{|\vec{E}|T}\right)x\right]$$
 (2.14)

where x is the drift distance over which electron multiplication occurs.

From Equation 2.14 we would expect a limitless exponential gas gain. But it is constrained by the Raether limit (Raether 1964) given by $G < 10^8$ or $\alpha x < 20$. To comprehensively understand this phenomenon, it is essential to examine the distinct operational regimes of gas-filled detectors and their corresponding influence on detector performance. These operational regions are illustrated in Figure 2.5.

Gas-filled radiation detectors operate in distinct regimes that are characterized by different charge multiplication mechanisms and signal responses. These operational regions can be understood by examining how the detector behavior changes as a function of the applied voltage in Figure 2.5.

At low voltages, detectors operate in the recombination region where the electric field is insufficient to prevent the recombination of ion-electron pairs created by incident radiation. This results in poor charge collection efficiency and weak signal output. As the voltage increases, the detector enters the ionization chamber region, where the electric field becomes strong enough to collect all primary charge carriers without secondary multiplication. In this regime, the output signal is directly proportional to the initial ionization energy, providing excellent energy resolution but limited sensitivity due to small signal amplitudes. Further voltage increases lead to the proportional region, where gas multiplication begins through the avalanche process governed by the Townsend mechanism. Here, primary elec-

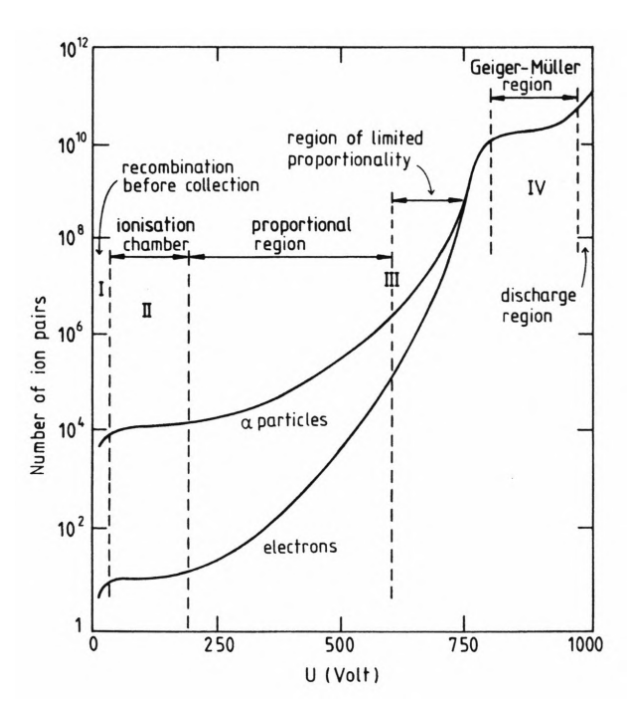


Figure 2.5: Characteristic operation regions of gaseous detectors showing the dependence on applied voltage (adapted from (Melissinos 1966)).

trons gain sufficient energy between collisions to ionize additional gas molecules, creating secondary electrons that participate in further multiplication. The crucial characteristic of this region is that the multiplication factor remains proportional to the primary ionization and, by extension, to the energy loss in the drift region, thereby preserving spectroscopic information while significantly enhancing signal amplitude.

At even higher voltages, the detector transitions to the limited proportional region, where space charge effects begin to influence the multiplication process, causing deviations from strict proportionality. Eventually, the detector enters the Geiger–Müller region, where the avalanche spreads throughout the entire sensitive volume, producing uniform output pulses regardless of the initial ionization energy.

The fundamental boundary between controlled multiplication and uncontrolled discharge is defined by the Raether limit (Raether 1964). This limitation arises from space charge effects that distort the electric field distribution when the electron density becomes too high during the avalanche process. Exceeding the Raether limit results in the formation of self-propagating streamers and electrical breakdown events that can cause permanent damage to the detector. The transition occurs because the accumulated positive ions from the avalanche create sufficient space charge to significantly alter the applied electric field, leading to uncontrolled discharge phenomena. Practical detector operation, therefore, requires careful optimization of the applied voltage to maximize gain while maintaining stable operation with appropriate safety margins below this fundamental threshold. The detectors used in this thesis are operated in the proportional region.

Chapter 3

Micromegas Detectors

3.1 Resistive Micromegas

The Resistive Micromegas detector is a three-electrode gaseous detector (Alexopoulos et al. 2011), developed as an advancement of the Micromegas detector (Giomataris et al. 1996). It has a cathode, a grounded stainless steel micro-mesh, and a resistive anode. In the drift region, charges from the primary ionization are collected. The drift region between the cathode and the micro mesh is a few millimeters wide (exemplary values are 5 mm wide drift gap) and operates under a relatively weak electric field ($\mathcal{O}(<1\,\mathrm{keV\,cm^{-1}})$). Insulating pillars determine the height of the amplification region (0.1 mm) and ensure homogeneity of the fields. This small amplification gap leads to high electric fields in the region ($\mathcal{O}(40\,\mathrm{keV\,cm^{-1}})$ to $50\,\mathrm{keV\,cm^{-1}})$). This difference in the fields results in funneling of the drift fields through the mesh increasing the electron transparency (Bortfeldt 2015). Electrons entering the amplification region, under the high electric fields undergoes Townsend avalanches following the discussion from subsection 2.2.3. The readout layer is placed below the resistive anode. The charges are capacitively coupled to the readout structure. A DLC (Diamond Like Carbon) layer has been used as the resistive layer for the detectors investigated throughout this work.

The anode readout structure usually consists of strips or pixels that are then read out. The detector volume is filled with gas. The choice of the gas mixture is crucial to the geometry and the operational goal of the detector. The usual choice of gas includes a selection of Argon gas (Ar) mixture along with carbon dioxide (CO_2) or isobutane (iC_4H_{10}). The Argon gas provides efficient primary ionization while CO_2 and iC_4H_{10} are used as quenching gases. Combining the geometry and the choice of gas, Micromegas are capable of achieving spatial resolutions up to 50 µm and excellent timing resolutions of up to 1 ns.

3.2 Anode readout configurations

The selection of readout geometry is critical in detector development. The constraints regarding experimental requirements and available resources lead to a trade-off between

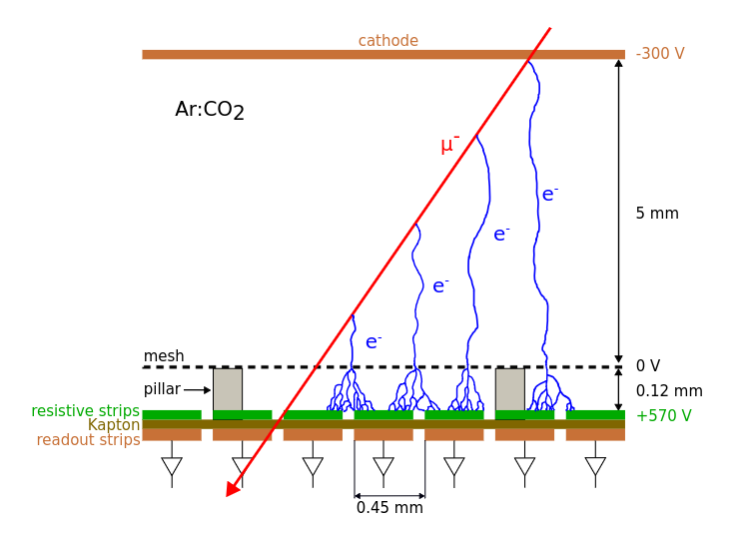


Figure 3.1: Schematic diagram of a Micromegas detector showing the three-electrode configuration. The detector consists of a cathode at negative potential, a grounded micromesh, and an anode at positive potential. The drift region (5 mm) allows primary ionization collection, while the narrow amplification region (120 μ m) between mesh and anode creates high electric fields for electron avalanche multiplication. Figure adapted from (Vogel 2024).

spatial resolution, rate capability, and system complexity. So, detector must prioritize performance metrics according to experimental objectives. Two major readout architectures are employed in Micromegas detectors: strip and pixel geometries.

3.2.1 Strip Readout

Strip readout represents the most common and well-established configuration for resistive Micromegas detectors. In this geometry, the readout layer beneath the resistive anode consists of parallel conductive strips. The strip pitch, defined as the center-to-center distance between adjacent strips, typically ranges from 200 µm to 1 mm, depending on the required spatial resolution and the specific application (Giomataris et al. 1996).

Each strip functions as an independent readout channel through capacitive coupling. Since the signal is capacitively coupled to the strips from the resistive anode, it is possible to have a 2D readout. The resistive layer, in strip readout configurations, enables charge spreading across multiple readout strips before being capacitively coupled to the underlying strips. In addition, in the amplification region, due to the repulsion between the electrons, the charge spreads over multiple strips. This spread-out charge distribution can be analyzed to achieve spatial resolutions significantly better than the statistical limit given by

$$\sigma = \frac{L}{\sqrt{12}} \tag{3.1}$$

where σ is the maximum achievable resolution and L is the strip pitch (Grupen et al. 2008). Typical spatial resolutions of 50-100 µm have been demonstrated with strip pitches

of 400-500 µm (Manjarres et al. 2012), and can reach better resolution with smaller strip pitches. But more readout strips translate into more extensive electronics.

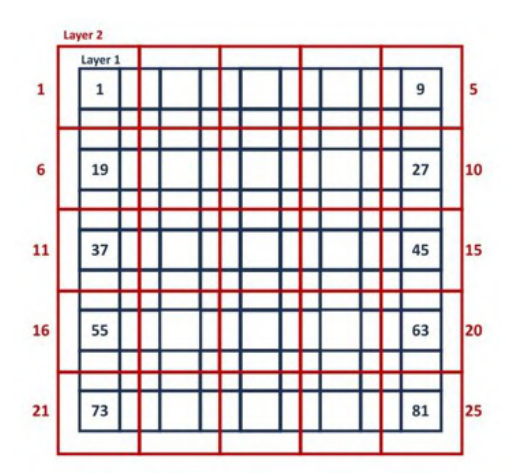
3.2.2 Pixel Readout

Pixel readout represents a more sophisticated approach where the readout layer beneath the resistive anode is segmented into discrete two-dimensional elements, typically square or rectangular in shape. Modern implementations include small-pad configurations with sizes ranging from 1 mm \times 3 mm to pixel arrays as fine as 55 µm \times 55 µm in GridPix detectors. (Alviggi et al. 2019; Scharenberg et al. 2025).

The fundamental advantage of pixel readout in resistive Micromegas is its ability to provide unambiguous two-dimensional position information from a single detection layer while maintaining discharge protection through the resistive layer. Each pixel functions as an independent detector element, enabling excellent performance in high-rate environments by eliminating the ghost hit ambiguities inherent to crossed-strip configurations. The primary limitations of pixel readout stem from increased complexity in terms of readout channels. For an active area of 10 cm $\times 10$ cm, with pixels of size 55 µm \times 55 µm, 3304900 pixels are required and hence 3304900 readout channels. The number of readout channels scales quadratically with the detector area when maintaining constant pixel size , leading to significantly higher channel counts compared to strip configurations.

3.3 Capacitive-Sharing Pixel Micromegas Detector

An approach to reducing channel proliferation involves the implementation of charge-sharing architectures across multiple layers. In this approach, a first collection layer of micro-pixels with high granularity collects the charges from the anode. Instead of reading out this layer, which would require a large number of channels, the collected charges are coupled to another layer of larger pixels separated by a dielectric medium through the principles of capacitive coupling and charge sharing (Gnanvo et al. 2023). This process can be continued over multiple layers. The largest pixel layer is then read out. This reduces the number of pixels in each layer by a factor of 4. The fundamental advantage of this approach lies in its ability to maintain the excellent spatial resolution associated with fine pixelation while reducing the channel count. This effectively decouples the read-out channel from spatial resolution, allowing us to go beyond the limit of Pitch_{Readout}/ $\sqrt{12}$. The charge-sharing mechanism exploits the same lateral charge spreading principle utilized



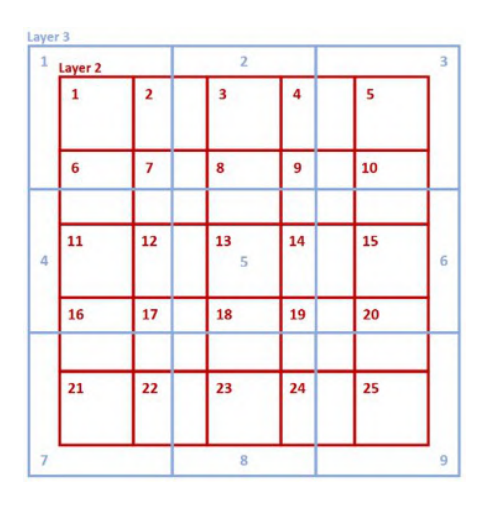


Figure 3.2: A schematic for three-layer pixel coupling is shown in the figure. On the left, 9*9 pixels are coupled to a larger 5*5 layer. On the right, the 5*5 layer is coupled to a larger 3*3 pixel layer. An initial number of 81 pixels is reduced to 9 pixels in the third layer. Figure taken from (Kumar 2026)

in resistive strip configurations, but extends it vertically through the detector structure. When an avalanche occurs, the charge initially deposits on multiple micro-pixels in the collection layer. Through capacitive coupling, this charge distribution induces signals on the pads of subsequent layers. This enables position reconstruction using the charge centroid method section 4.3.

Capacitive Charge sharing

The concept of capacitive-sharing involves two parts. It starts with the physics of capacitive coupling across multiple layers. In the simplest approximation, this can be viewed as a system of linear capacitors separated by a dielectric medium. Starting with just two layers,

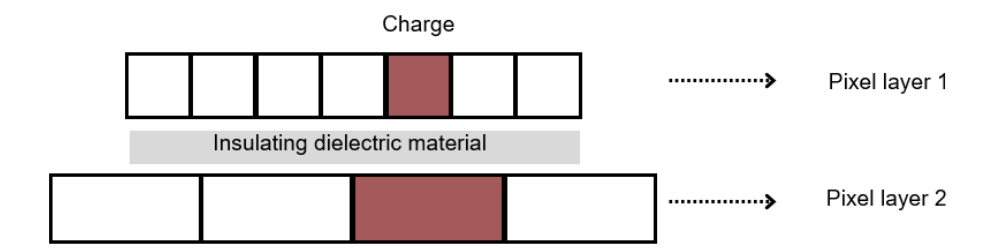


Figure 3.3: Schematic representation of capacitive coupling between two pixel layers separated by a dielectric medium. Each overlapping region between micro-pixel i in layer 1 and readout pixel j in layer 2 forms a parallel-plate capacitor with capacitance $C_{ij} = \epsilon_0 \epsilon_r A_{ij}/d$. The charge collected on the micro-pixel is distributed among the connected capacitors based on their geometric overlap areas, enabling controlled charge sharing for position reconstruction. The pixels in a single layer are separated by the vertical black lines. This separation leads to a lateral capacity coupling between the pixels, which is small due to the area of geometric overlap is small compared to the pixel layer above. (Figure not to scale)

in the simplest approximation, the capacitive coupling between pixel layers can be modeled as a network of parallel-plate capacitors. Consider a micro-pixel in layer 1 positioned above multiple readout pixels in layer 2, separated by a dielectric of thickness d. Each overlapping region forms a distinct capacitor with capacitance

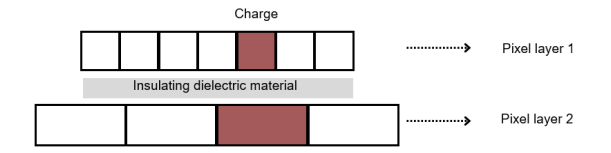
$$C_{ij} = \epsilon_0 \epsilon_r A_{ij} / d \tag{3.2}$$

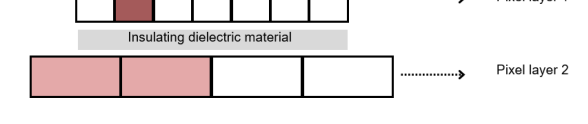
where C_{ij} represents the coupling capacitance between micro-pixel i and readout pixel j, ϵ_0 is the vacuum permittivity, ϵ_r is the relative permittivity of the dielectric, and A_{ij} is the overlapping area between the two pixels (Griffiths 2017). When a charge Q_i is collected on micro-pixel i, it is distributed among all capacitors connected to that pixel (See Figure 3.3). This linear model shows that the charge distribution depends solely on the geometric overlap ratios in the ideal case.

Having established charge coupling, the next step is to adapt a geometry such that the coupled charges do not create an ambiguity when reconstructing the position. In this thesis, following the idea proposed by (Gnanvo et al. 2023) for strip readout, each bigger layer of pixels is twice the size of the smaller layers. The bigger pixel is shared between 9 smaller pixels. The bigger pixel is aligned to share its center with one smaller pixel (see Figure 3.2). This ensures an entirely symmetric arrangement of pixels on each layer. This symmetry can be exploited for position reconstruction. In Figure 3.4a, Figure 3.4b, Figure 3.4c, the proposed geometry for 2 layers is shown. It can be clearly observed how the charges are uniquely coupled to the next layer, based on the symmetry and geometric overlap of the system. Depending on the area of geometric overlap, the charges are split between the pixels on the bigger layer. This principle can then be applied to another bigger layer as seen in Figure 3.4d. This splitting shifts the position when reconstructing the position

using charge centroid method (See section 4.3). This will be discussed in more detail in chapter 5.

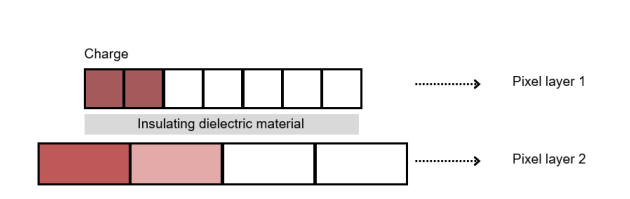
Charge



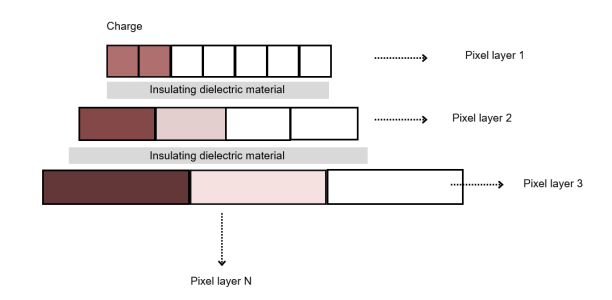


(a) Charge coupled to exactly one pixel below

(b) Charges shared equally to two geometrically overlapping pixels below



(c) Asymmetric charge sharing based on geometric overlap of pixels



(d) Charge coupling cascade over three layers

Figure 3.4: Illustration of charge coupling in charge sharing detectors. Multiple cases are shown illustrating how the ambiguity in charge coupling is removed.

3.3.1 Readout Configurations

Two prototypes of Micromegas detectors were tested throughout this thesis, hereafter called PADH and PAD5. Both use the concept of charge sharing through multiple pixel layers. However, they are different regarding the number of layers and the readout structure, which is discussed below.

PAD5

The PAD5 detector implements a five-layer pixel structure with geometric scaling between layers. The micro-pixel pitch increases progressively from 0.625 mm in layer 1 to 1.25 mm in layer 2, 2.5 mm in layer 3, 5 mm in layer 4 and finally 10 mm in the readout layer (layer 5), spanning an active area of 10×10 cm². This configuration comprises 145×145 micro-pixels in the collection layer, while requiring only 10×10 readout channels

The advantage of charge sharing becomes evident here. Reading out the pixels from layer 1 would require 21025 readout channels compared to just 100 readout channels on layer 5. This is almost 210-fold fewer electronics than are necessary. The readout schematic of PAD5 is shown in Figure 3.5. The 100 pixels from layer 5 are individually read out through the front-end electronics. The detector operates with an 8 mm drift gap and a 100

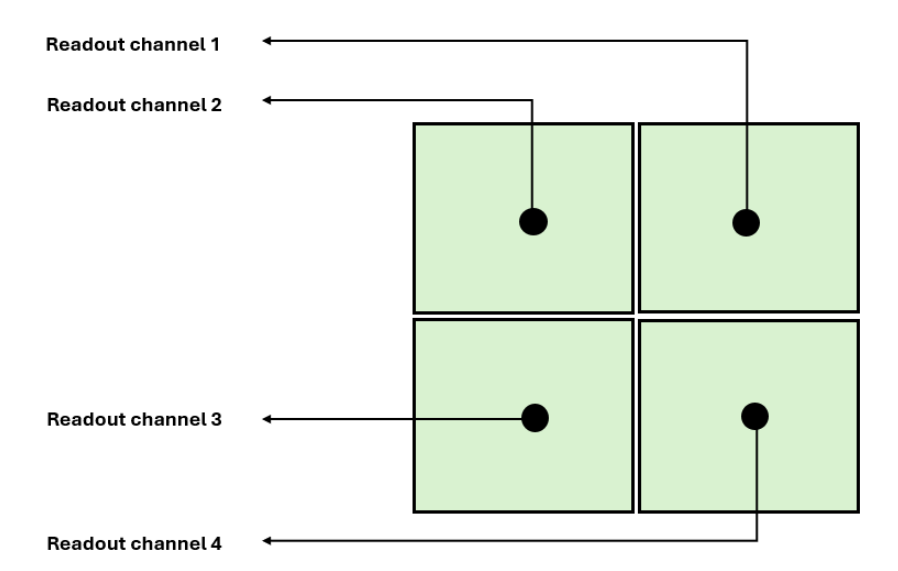


Figure 3.5: Readout schematic of the PAD5 detector. Each pixel in the final layer is individually connected to dedicated readout channels.

µm amplification gap, incorporating a DLC (Diamond Like Carbon) resistive layer. The schematic of the PAD5 detector is illustrated in Figure 3.6. The 5-layer coupled pixel layer is visible.

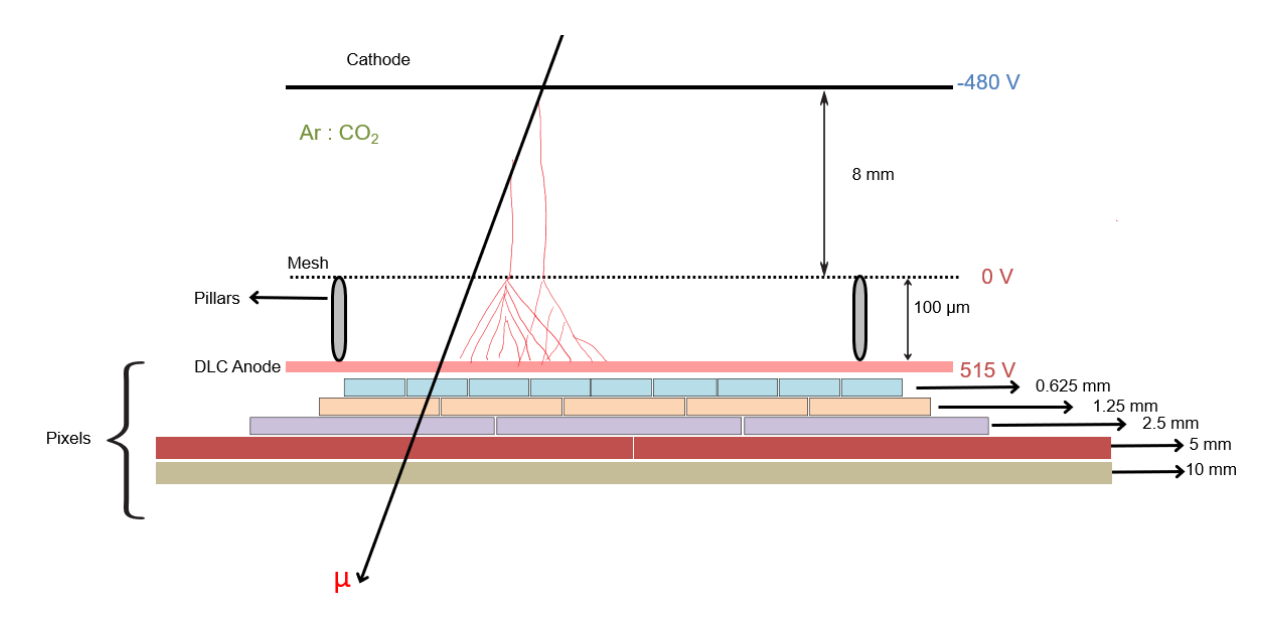


Figure 3.6: Schematic cross-section of the PAD5 detector showing the five-layer charge-sharing architecture. The detector features a cathode, micromesh, and five pixelated layers with progressively increasing pixel sizes from 0.625 mm (layer 1) to 10 mm (layer 5). The 145×145 micro-pixels in the collection layer are reduced to 100 readout channels in the final layer through capacitive charge sharing across the intermediate layers. The detector features a drift gap of 8 mm and 100 μ m amplification gap.

PADH

The PADH detector employs a more compact three-layer design with progressive doubling of pixel pitch: 0.3 mm, 0.6 mm, and 1.2 mm. Despite maintaining the same $10 \times 10 \text{ cm}^2$ active area, this configuration has 340×340 pixels in the collection layer. The readout layer contains 85×85 channels, reducing the channel count from 115,600 to 7,225—a 16-fold decrease. While this reduction is less dramatic than PAD5, the finer initial pixelation offers superior spatial resolution. Reading out 7225 channels is a heavy task in terms of readout channels. To mitigate this problem, a hybrid strip-pixel readout scheme is employed. The pixels in layer 3 are segmented diagonally into two triangular parts. The upper triangular sections of pixels along each row are connected together by a copper strip, while the lower triangular sections along each column are similarly connected.

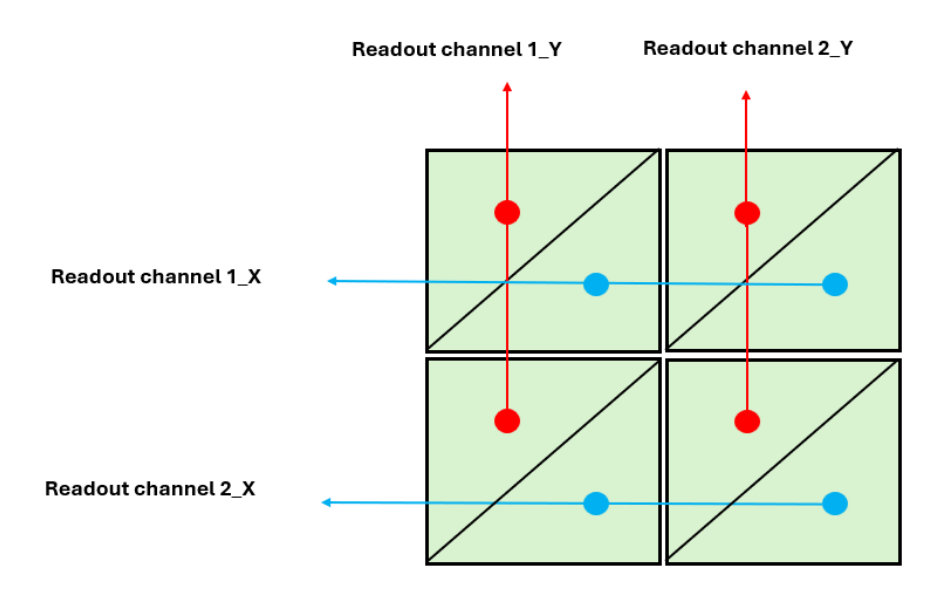


Figure 3.7: Readout schematic of the PADH detector illustrating the hybrid strip-pixel configuration. The 85×85 pixels in layer 3 are segmented diagonally, with lower triangular sections connected as horizontal strips (X-direction) and upper triangular sections connected as vertical strips (Y-direction). This innovative readout scheme reduces the required electronics from 7,225 individual pixel channels to just 170 strip channels (85 X + 85 Y), while preserving full 2D position reconstruction capability through the combination of orthogonal strip signals.

This configuration creates orthogonal strip readouts as shown in Figure 3.7. By combining the row and column strip signals, full 2D position reconstruction is achieved while reducing the readout channels from 7,225 (85×85) to just 170 (85 + 85) channels—a further 42-fold reduction. The detector operates with a 5 mm drift gap and a 100 μ m amplification gap, incorporating a DLC resistive layer. The schematic of the PADH detector is illustrated in Figure 3.8. The 3-layer coupled pixel layer is visible.

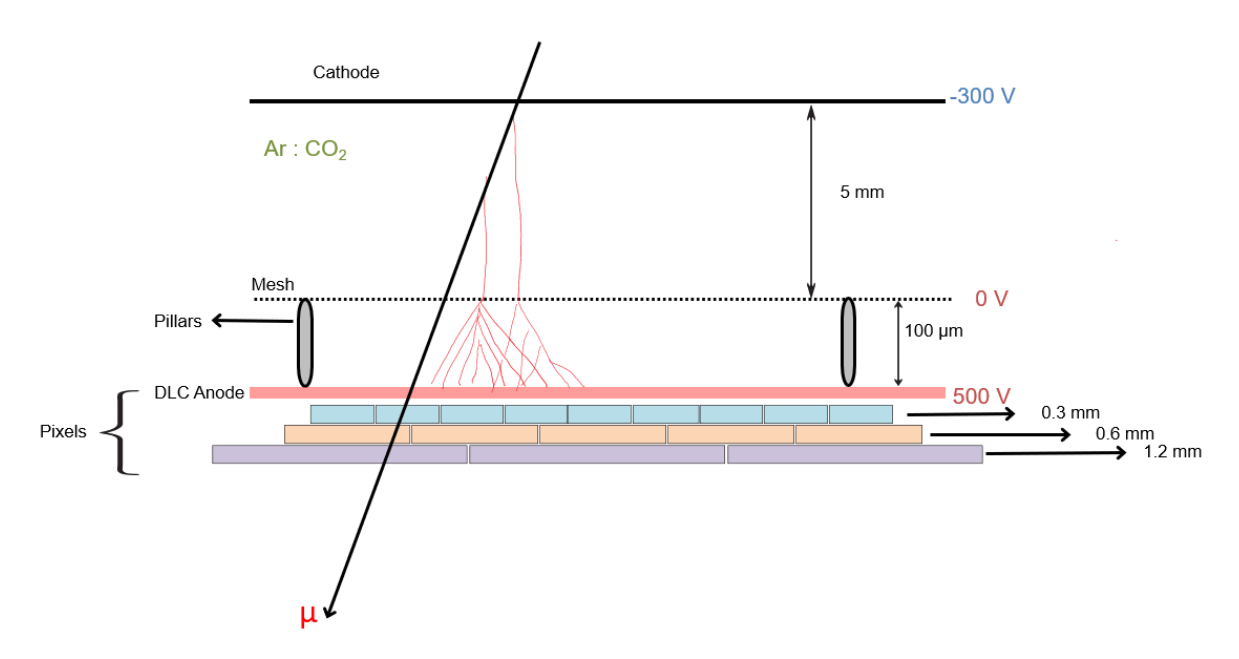


Figure 3.8: Schematic cross-section of the PADH detector illustrating the three-layer charge-sharing structure with hybrid readout. The pixel pitch doubles sequentially from 0.3 mm (layer 1) to 1.2 mm (layer 3), reducing 340×340 collection pixels to 85×85 intermediate pixels.

Chapter 4

Experimental Techniques

Following chapter 2 and chapter 3, the physics of charge collection and amplification within the detector volume is discussed. These charges form signals that must be collected, processed, and interpreted meaningfully. The readout electronics and subsequent reconstruction algorithms transform these raw signals into meaningful particle information. Later, this information is used to characterize the detector's performance and further enable its use in real experiments.

4.1 Scalable Readout System (SRS)

The measurements in this thesis utilize a readout architecture based on the Scalable Readout System (SRS), which uses APV25 Application Specific Integrated Circuits (ASICs) mounted on hybrid boards. Originally developed by Martoiu et al. (Martoiu et al. 2013), the SRS is a flexible system for signal acquisition and processing. The system consists of various parts.

- The APV25 hybrid board as the front-end electronics
- The Analog to Digital Converter (ADC) card to digitize the signal
- The Front End Concentrator (FEC) card
- A Data Acquisition (DAQ) PC

The front-end hybrid boards on the detector have discharge protectors, power regulators, and the APV25 readout ASIC (see Figure 4.1). The protection circuits protect the readout electronics against potentially high current signals from discharges. Initially designed for the CMS silicon tracker (Jones 2001), these chips preamplify and shape the incoming analog signals from the detector. The APV25 has 128 readout channels, each with its own preamplifier, shaper and analog pipeline memory. The signal is sampled across 27 or a shorter 24 time bins, each 25 ns wide $(27 \times 25 \ ns)$ or $24 \times 25 \ ns$. The latter is used to sample the signals in this thesis. Signal saturation occurs between 1400 and 1800 ADC, defining the system's dynamic range. Information beyond this is lost and cannot be used efficiently to reconstruct the charge.

The data from the hybrid board is read out via an HDMI cable. Two hybrid boards can

be operated in the master-slave configuration via a flatband cable. In this configuration, a single HDMI can read out information from two hybrid boards, translating to information from 128×2 channels.

The hybrid boards are connected to the ADC via the HDMI cable, which also powers the APV25 with 5 V, eliminating the need for an additional power source. The ADC digitizes the analog input signal. A maximum of 8 HDMI's or 16 APV25 hybrid boards in the master slave configuration can be connected to one ADC card. After digitization, the ADC is connected to the FEC via PCIe (Peripheral Component Interconnect express)interface. The Front-End Concentrator (FEC) card manages the front-end electronics configuration, processes trigger signals for readout, and serves as the primary interface to the DAQ PC through an ethernet cable.

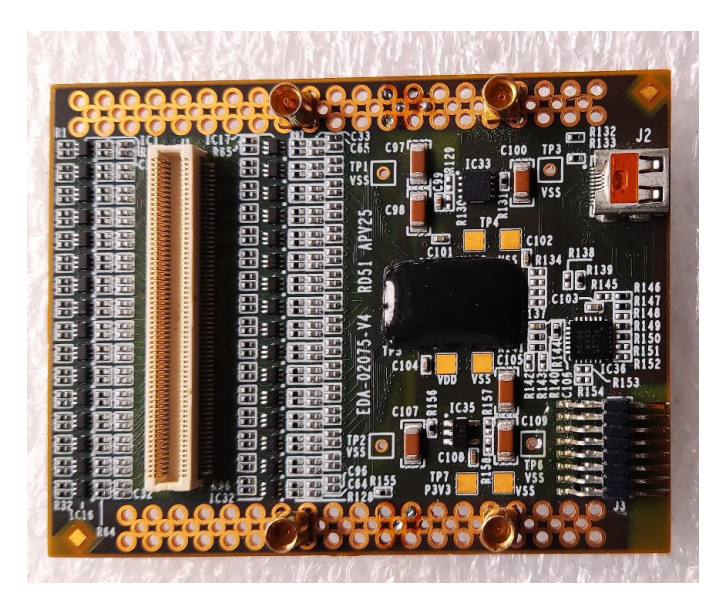


Figure 4.1: APV25 hybrid board showing the front-end electronics with discharge protectors, power regulators, and the APV25 readout ASIC. The board features 128 readout channels, each with its own preamplifier, shaper, and analog pipeline memory.

The data taking is initialised and stored for later analysis on the DAQ PC. When multiple FEC cards are utilized, synchronization is implemented by using ethernet cables of equal length. This ensures that the data arrives at the same time.

Data taking is initialized when the FEC receives a trigger. The trigger system is configured differently depending on the measurement type and optimized for detection requirements. Detector characterization is carried out through measurements with a ⁵⁵Fe source and with muons. The trigger logic for the two is different.

For measurements using the ⁵⁵Fe radioactive source, a simplified trigger logic is adopted due to the single-detector configuration and the characteristic X-ray emission properties of the source. The detector mesh signal is amplified using a preamplifier and serves as the direct trigger source. The preamplified mesh signal is then fed to a timing filter amplifier, where the signal is appropriately shaped. This signal is then fed to a low threshold discriminator.

The threshold is set to distinguish genuine X-ray events from electronic noise. Since ⁵⁵Fe emits characteristic X-rays with well-defined energies, the discriminator threshold can be optimized to trigger on these events while rejecting background signals selectively. The discriminated signal is then processed through the dual timer operating in fixed-rate mode before being sent to the FEC card. The FEC card takes these trigger signals and reads out the signals from the APV hybrid boards on the detector and sends them to the DAQ PC for further analysis (See Figure 6.2 for the trigger logic schematic).

The muon detection readout sequence begins when the FEC card receives a coincidence trigger signal. Figure 6.12 illustrates the trigger determination architecture, which relies on a pair of scintillators coupled to photomultiplier tubes (PMTs). These components serve as fast-response triggers that differentiate actual muon events from background events.

When muons pass through the scintillators, they produce light pulses that the photomultipliers convert into electrical signals. These signals are sent to discriminators through Nuclear Instrumentation Standard (NIM) cables. When the input pulse exceeds the set threshold, the discriminators generate a fixed duration NIM pulse. These pulses are routed to a coincidence logic unit where an AND operation is performed.

A valid trigger emerges from the coincidence unit only when signals from both scintillators and the discriminator pulse durations from the two scintillators overlap. This coincidence criterion provides robust rejection of both random background radiation and electronic noise, since the likelihood of noise appearing simultaneously in both channels remains far below that of a muon passing through both scintillators.

The dual timer can be configured for synchronized operation in two modes. One, with its pulse duration set to a fixed value. Data acquisition from the APV25 happens within this set time. After this, the system is ready for the next trigger. This mode is used when taking data with one FEC in low-rate environments. In the thesis, the measurements with cosmic muons utilize this mode of operation (See Figure 6.12 for the trigger logic schematic for muons).

In the second mode of operation, the pulse duration of the dual timer is set to "infinity." Following the generation of an initial trigger, the system blocks all subsequent triggers until it receives an external reset command. An Arduino, connected to the DAQ PC, handles reset control. The Arduino transmits a NIM-format reset signal to the dual timer exclusively after completing data processing for the current event, thereby enabling acceptance of the next muon trigger. This is required for high-rate environments or multiple FEC operations. During this thesis, measurements at the H4 test beam at SPS CERN, utilize this mode of operation (See Figure 7.2 for beamtime trigger logic).

In single FEC arrangements, the trigger from the dual timer connects directly to the FEC card. However, when using multiple FEC cards, all the FECs require a simultaneous trigger. For this purpose, a Fan-In Fan-Out (FIFO) logic module replicates and routes the dual timer output to all associated FEC cards, guaranteeing coherent triggering across the entire system for synchronized muon detection spanning multiple detector channels.

4.2 Signal Reconstruction

A typical signal of a muon event is shown in Figure 4.2. The signal has a fast rising edge from the drift of the electrons and a slow tail from the slower ion drift. This signal is parametrized using an inverse Fermi function:

$$q(t) = \frac{Q}{1 + \exp\left(\frac{t_0 - t}{t_{\text{rise}}}\right)} + q_0 \tag{4.1}$$

where Q represents the total induced charge on the readout strip, t_{rise} characterizes the rise time and t_0 denotes the point of inflection. q_0 accounts for the baseline offset from the zero value of ADC. The amplitude parameter Q directly yields the charge deposited

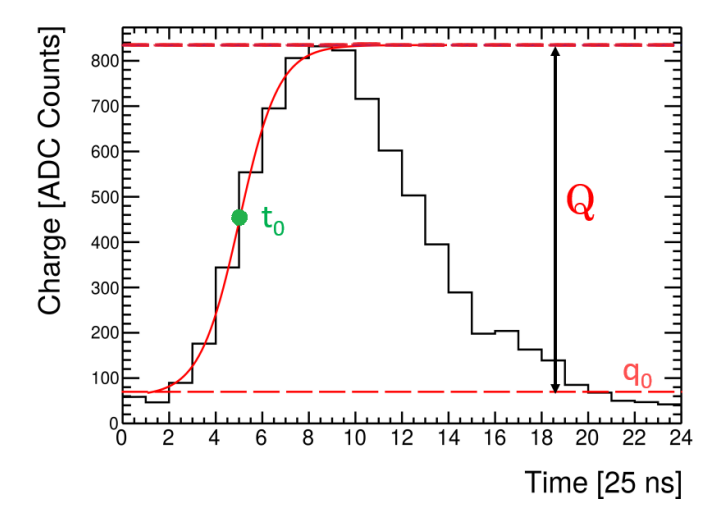


Figure 4.2: Example of a typical APV25 signal. The signal is fitted with an inverse Fermi function (Equation 4.1) to extract timing and amplitude information. The inflection point t_0 provides signal timing, while the height Q of the function gives the charge.

on each readout strip. This fitting procedure provides timing resolution superior to the APV25's 25 ns sampling interval. The inflection point of the Fermi function, occurring at $t=t_0$, defines the precise signal timing. Such timing information proves essential for track reconstruction algorithms when particles traverse the detector at inclined angles. In contrast, perpendicularly incident particles require only charge information for position determination.

4.3 Cluster Building

Ionized particles that traverse a detector volume produce a localised charge distribution that spreads over multiple strips or pixels. This distribution usually has a Gaussian shape.

The signals from multiple channels that are collected by the APV25s have to be merged in a meaningful way to extract charge information of a single event and to reconstruct the position. This process is called clustering.

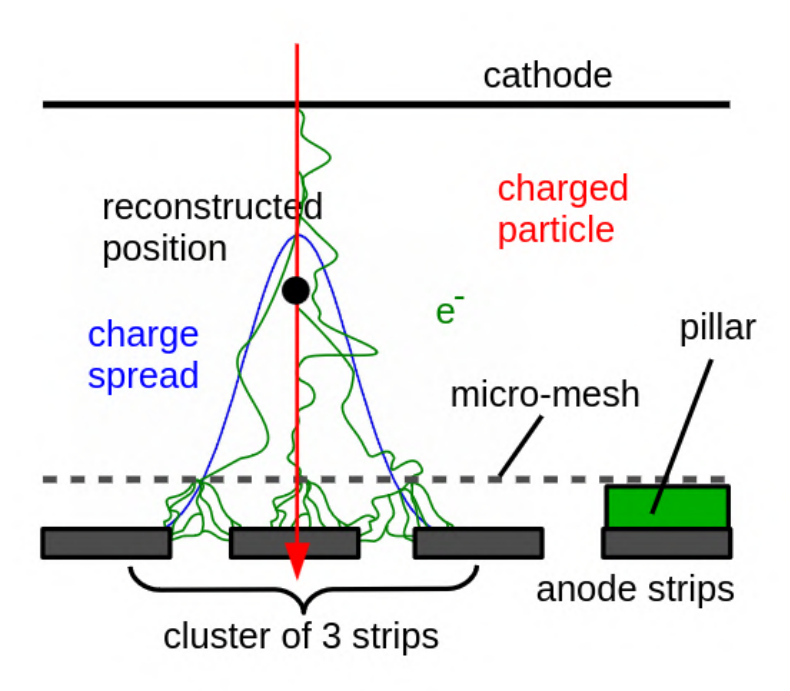


Figure 4.3: Clustering algorithm grouping adjacent fired strips. Strips above threshold are grouped into clusters, allowing one missing strip to account for dead channels. The total cluster charge is obtained by summing individual strip charges, and the position is calculated using charge-weighted centroid methods. Figure adapted from (Klitzner 2019).

The clustering algorithm reconstructs the spatial extent of charge deposition by grouping adjacent fired strips into coherent clusters. To account for channel inefficiencies and noise, the algorithm permits one missing strip within a cluster, provided it has valid signals on both sides. This gap prevents artificial cluster splitting due to dead channels while maintaining rejection of noise-induced false clusters. Clusters usually contain at least two strips above threshold, and no more than one non-consecutive gap is permitted. After cluster formation, the total cluster charge is calculated by summing the individual channel charges, while the position is determined using either a simple charge-weighted mean (centroid) algorithm for perpendicular tracks. Determining the position for inclined tracks requires more sophisticated methods.

For pixel clustering, a graph theory-based Depth-First Search (DFS) algorithm is employed to efficiently identify clusters of pixels. The DFS systematically explores the cluster topology by evaluating all eight adjacent neighbors (horizontal, vertical, and diagonal connections) using directional vectors, starting from a seed pixel. For each identified cluster, the position is calculated by charge-weighted mean (centroid).

Charge Centroid Method:

A symmetric Gaussian distribution is expected for perpendicular tracks, as no inhomogeneities in ionization are expected for perpendicularly incident particles. Making use of this fact, a simple symmetric charge-weighted centroid algorithm can be used for determining cluster position for perpendicular particle tracks.

$$Y_{\text{cluster}} = \frac{\sum_{\text{strips}} Q_{\text{strip}} \times Y_{\text{strip}}}{\sum_{\text{strips}} Q_{\text{strip}}}$$
(4.2)

where Q_{strip} denotes the strip charge and Y_{strip} represents the physical position of the strip. This charge-weighted averaging technique exploits the charge sharing between adjacent strips to achieve position resolution significantly better than the intrinsic strip pitch. For typical charge distributions, this method yields spatial resolution on the order of pitch/ $\sqrt{12}$.

4.4 Track Reconstruction

4.4.1 Reference Tracking

To determine the performance of a detector, the reconstructed position within the detector is not enough. Furthermore, the true position of the particle should also be known to parameterize the resolution of the detector. However, the true position of the particle is not known a priori. To determine this, a precise reference track is needed.

This reference track is obtained using a detector hodoscope consisting of multiple tracking detectors positioned along the beam axis. Each tracking detector provides a hit position determined via the centroid method. By combining hit positions from all tracking detectors with their known z-coordinates along the beam axis, a linear reference track is fitted through the tracking detectors.

The track reconstruction employs χ^2 minimization to find the optimal track (Klitzner 2019). For a reference system with n detectors, the resolution of the tracking detectors should also be taken into consideration. The track accuracy at any position z is given by (Horvat 2005):

$$\sigma_{\text{track}}^2(z) = \frac{\Lambda_{22} - 2z\Lambda_{12} + z^2\Lambda_{11}}{\Lambda_{11}\Lambda_{22} - \Lambda_{12}^2}$$
(4.3)

The matrix elements Λ_{ij} incorporate the position and resolution of each tracking detector:

$$(\Lambda_{11}, \Lambda_{12}, \Lambda_{22}) = \sum_{i=1}^{n} \frac{(1, z_i, z_i^2)}{\sigma_i^2}$$
(4.4)

where z_i denotes the position of detector i along the beam axis and σ_i represents its spatial resolution.

The resolution of individual reference detectors is determined through the geometric mean method. This involves reconstructing tracks twice for each detector and determining the corresponding resolutions: once with the detector included in the track fit (σ_{in}) and once with it excluded (σ_{ex}). When all detectors have comparable spatial resolution, the geometric mean provides (Carnegie et al. 2005):

$$\sigma = \sqrt{\sigma_{\rm in} \cdot \sigma_{\rm ex}} \tag{4.5}$$

Between reference detectors, the interpolated track resolution exceeds that of individual detectors due to multiple measurement points. Track reconstruction is performed independently for each detector coordinate. Only events where all reference detectors register at least one hit and the extrapolated track passes through the active detector area are used to build a track. This eliminates false tracks from inefficient areas of detectors or random noise triggers.

4.4.2 Detector Alignment

The track reconstruction methods are most efficient when the detectors are aligned with each other. If it is not, the reconstructed position is not exact and is not a good measure of the true resolution of the detector under test. Two types of detector alignment are employed while setting up a tracking hodoscope. The initial alignment is a hardware alignment where the detectors are aligned mechanically in the tracking hodoscope with a precision of a few millimeters. The fine alignment, where the detectors are aligned with micrometer precision, is done with software.

The software alignment is an iterative process, where the trackers are aligned first with each other. The alignment procedure relies on analyzing residuals—the difference between predicted and measured particle positions. The detector being aligned is excluded from track reconstruction to avoid any bias in the reference trajectory. The residual $P_{\rm res}$ is defined as:

$$P_{\rm res} = P_{\rm extrapolated} - P_{\rm cluster} \tag{4.6}$$

where $P_{\text{extrapolated}}$ represents the particle position predicted by reference tracking chambers, and P_{cluster} denotes the reconstructed position within the detector under investigation. P could be the direction X or Y along which the particle is tracked (Vogel 2024).

Systematic dependencies between residuals and various track parameters manifest as detector misalignment. The alignment procedure corrects for these correlations (Jagfeld 2023). In the following discussion, residuals along Y are considered as a prescription. The procedure is repeated along the X direction as well.

4.4.3 Detector Shifts

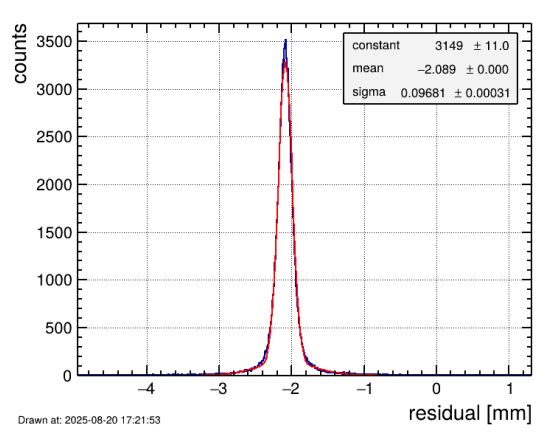
The simplest misalignment is a constant position offset with respect to the reference track, shifting the entire residual distribution away from zero (illustrated in Figure 4.4). This systematic shift is corrected by applying a constant offset:

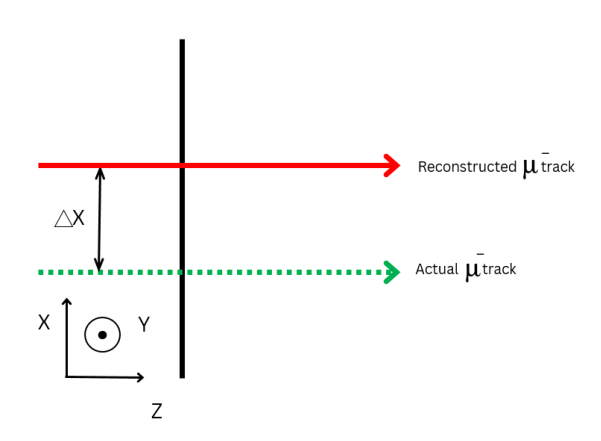
$$X_{\rm corr} = X + \Delta X \tag{4.7}$$

Misalignments along the beam axis (Z-direction) present a more subtle challenge. While perpendicular tracks show no sensitivity to Z-shifts, inclined trajectories reveal these offsets through a correlation between residuals and track angles (Figure 4.5). This correlation is parametrized using a linear fit:

$$\Delta X = p_1 \times \text{Slope} + p_0 \tag{4.8}$$

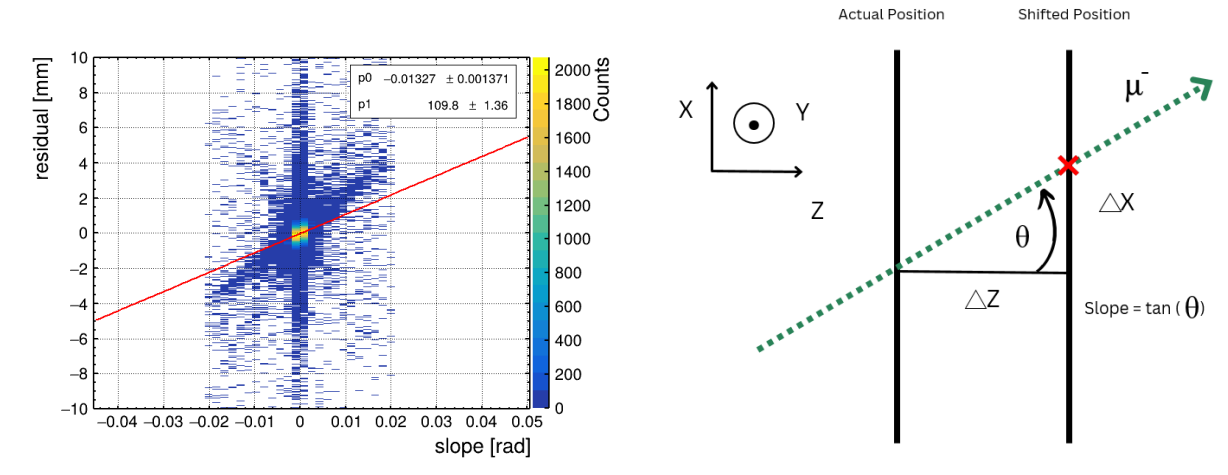
where p_1 represents the fit slope, p_0 is the offset.





- (a) Residual distribution showing constant Y-offset
- (b) Schematic of detector Y-shift misalignment

Figure 4.4: X-direction shift misalignment: (a) Measured residual distribution shifted from zero indicating a constant position offset. (b) Schematic representation showing the detector displaced by ΔX from its true position (dashed outline).



- (a) Residual vs. track slope correlation for Z-shift
- (b) Schematic of detector Z-shift misalignment

Figure 4.5: Z-direction shift misalignment: (a) Linear correlation between X-residuals and track slope revealing Z-position offset. The slope of the fitted line equals ΔZ . (b) Schematic showing how Z-displacement causes position errors for inclined tracks while perpendicular tracks remain unaffected.

4.4.4 Detector Rotations

Following the correction of detector shifts, rotational misalignments between detectors must be corrected for.

Rotation Around X and Y Axes

Rotation around the Y-axis manifests as a linear correlation between the X-residual and the X-position (Figure 4.6). Similarly, rotation around the X-axis produces a correlation between the X-residual and the X-position.

Rotation Around the Z-Axis

Z-axis rotation creates cross-correlations between residuals and orthogonal positions. Specifically, Y-residuals correlate with X-positions, while X-residuals correlate with Y-positions (Figure 4.7).

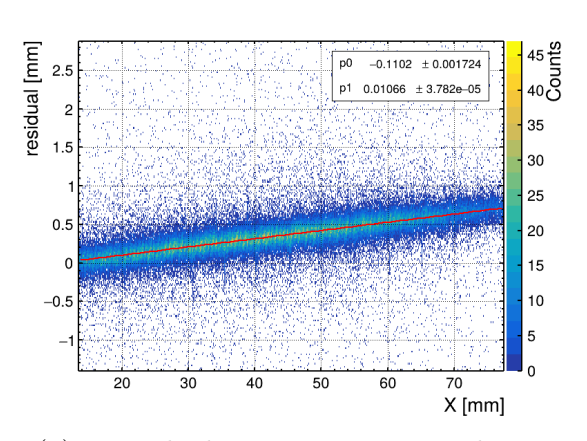
Implementation Strategy

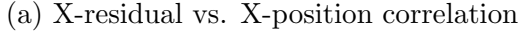
The complete alignment procedure follows an iterative approach:

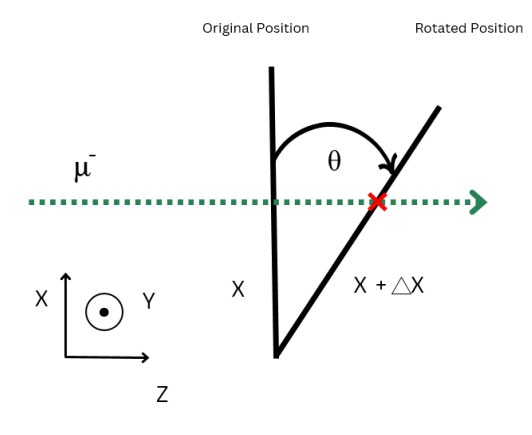
- 1. Apply translational corrections (subsection 4.4.3)
- 2. Apply rotational corrections (subsection 4.4.4)

3. Iterate until residual distributions show no systematic dependencies

This systematic approach ensures all six degrees of freedom (three translations and three rotations) are properly constrained, yielding optimal detector alignment for precision tracking.

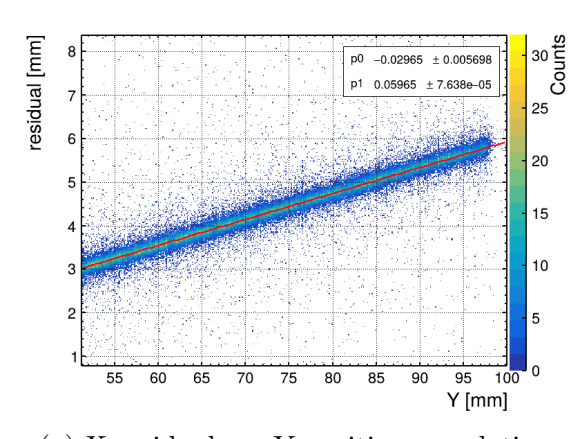




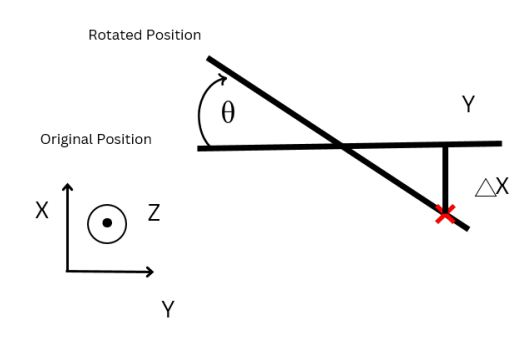


(b) Schematic of Y-axis rotation misalignment

Figure 4.6: Rotation around Y-axis: (a) Linear correlation between X-residuals and X-position indicating rotational misalignment about the Y-axis. The slope determines the rotation angle θ_y . (b) Schematic showing detector rotation around the Y-axis, causing systematic X-position errors that increase with distance from the rotation axis.



(a) X-residual vs. Y-position correlation



(b) Schematic of Z-axis rotation misalignment

Figure 4.7: Rotation around Z-axis: (a) Cross-correlation between X-residuals and Y-position (or vice versa) indicating in-plane rotation. The slope determines the rotation angle θ_z . (b) Schematic showing detector rotation around the Z-axis (beam axis), causing coupled X-Y position errors.

4.5 Spatial Resolution Determination

With an aligned detector hodoscope, the spatial resolution of the detectors under test can be investigated. Misalignment of either the reference detectors or the test detector leads to broader residual distributions and consequently deteriorates the measured resolution.

4.5.1 Residual Analysis

The reference track is extrapolated to the position of the detector under investigation. The residual quantifies the deviation between the measured cluster position x_{hit} and the reference position x_{ref} :

$$\Delta P_{res} = P_{\text{extrapolated}} - P_{\text{cluster}} \tag{4.9}$$

For a properly aligned detector setup, the residual distribution centers around $\Delta P = 0$ mm. The width of this residual distribution characterizes the spatial resolution of the detector.

The residual distribution is parametrized using a double Gaussian function:

$$f(x) = \operatorname{gauss}_{\operatorname{core}}(x) + \operatorname{gauss}_{\operatorname{tail}}(x)$$
 (4.10)

$$f(x) = A_{\text{core}} \exp\left(-\frac{(x - \Delta x_{\text{core}})^2}{2\sigma_{\text{core}}^2}\right) + A_{\text{tail}} \exp\left(-\frac{(x - \Delta x_{\text{tail}})^2}{2\sigma_{\text{tail}}^2}\right)$$
(4.11)

The narrow Gaussian component (σ_{core}) represents the intrinsic detector resolution under ideal conditions. The broader component (σ_{tail}) accounts for physical processes such as delta electron production and multiple scattering of the traversing particle. Delta electrons create secondary ionization tracks that broaden the charge distribution and degrade the apparent spatial resolution.

A combined resolution σ_{weighted} is calculated by weighting each Gaussian component by its relative contribution:

$$\sigma_{\text{weighted}} = \frac{\sigma_{\text{core}} \int \text{gauss}_{\text{core}} + \sigma_{\text{tail}} \int \text{gauss}_{\text{tail}}}{\int \text{gauss}_{\text{core}} + \int \text{gauss}_{\text{tail}}}$$
(4.12)

To extract the intrinsic detector resolution, the tracking accuracy σ_{track} (given by Equation 4.3) must be deconvolved from the measured combined resolution:

$$\sigma_{\text{detector}} = \sqrt{\sigma_{\text{core/weighted}}^2 - \sigma_{\text{track}}^2}$$
 (4.13)

This quadratic subtraction is valid when the tracking accuracy is significantly better than the detector resolution under investigation.

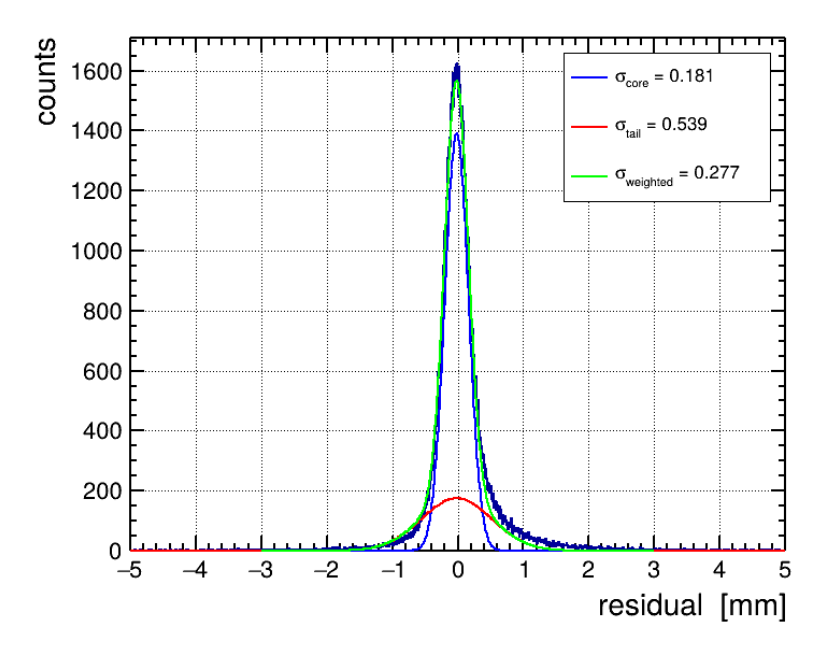


Figure 4.8: Double Gaussian fit to the residual distribution for spatial resolution determination. The histogram shows the measured residuals. The narrow core component (blue dashed line, σ_{core}) characterizes the intrinsic detector resolution under ideal conditions, while the broader tail component (red dashed line, σ_{tail}) accounts for physical effects such as delta electron production and multiple scattering.

4.6 Inclined Track Reconstruction

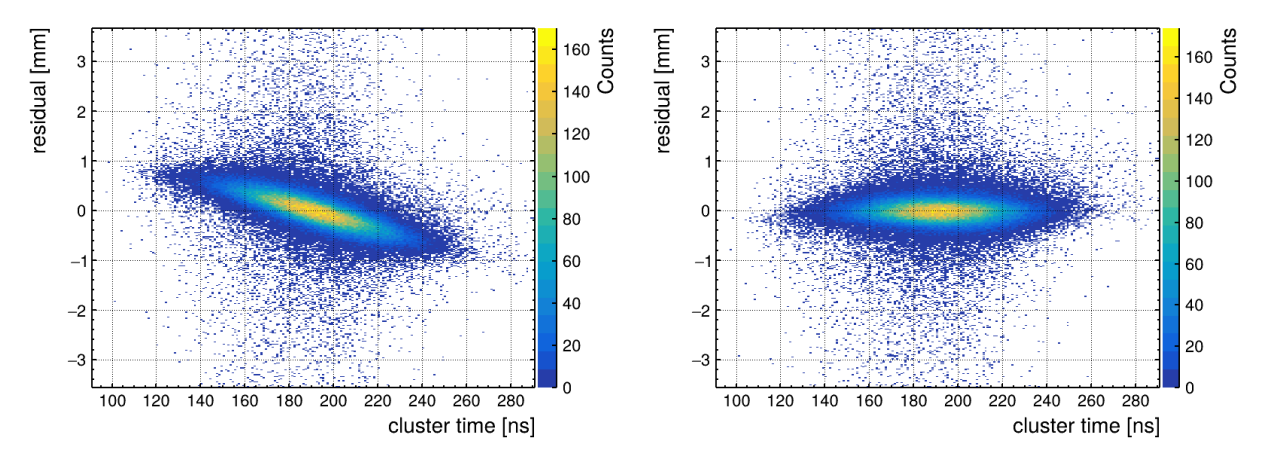
When particles traverse the detector at oblique angles, they ionize gas at different depths within the drift gap, creating an asymmetric charge distribution. Time corrected centroid (Flierl 2018) is a method for determining the position of inclined particle tracks. This approach applies a time-dependent correction to the reconstructed charge-weighted position based on the charge-weighted cluster time $t_{\rm CW}$, defined as:

$$t_{\text{CW}} = \frac{\sum_{\text{Strips}} (Q_{\text{Strip}} \times t_{\text{Strip}})}{\sum_{\text{Strips}} Q_{\text{Strip}}}$$
(4.14)

The method exploits the linear correlation between the centroid position shift Y_{CW} and the corresponding shift in charge-weighted cluster timing t_{CW} . This timing-position relationship can be systematically corrected using:

$$\Delta Y = \Delta t \times v_D \tan(\Theta) \tag{4.15}$$

where $\Delta t = t_{\text{True}} - t_{\text{CW}}$ represents the timing deviation, v_D is the electron drift velocity, and Θ is the track inclination angle. This can be corrected for, analogous to detector rotations, to give a better estimate of the position of particles incident at an incline.



- dependence.
- (a) Uncorrected position residuals vs cluster (b) Corrected position residuals vs cluster time time for 20° inclined tracks, showing clear linear for 20° inclined tracks after applying timedependent correction.

Figure 4.9: Comparison of position residuals before and after time correction for inclined tracks at 20°.

4.6.1 **Detection Efficiency**

The detection efficiency is the probability that a traversing particle produces a detectable cluster. Using the residual distribution, the position reconstruction efficiency is determined as:

$$\epsilon = \frac{N_{\text{hits},|\Delta P| < 3\text{mm}}}{N_{\text{track, ref}}} \tag{4.16}$$

where $N_{\text{hits},|\Delta P|<3\text{mm}}$ represents the number of reconstructed clusters with residuals smaller than 3 mm, and $N_{\text{track, ref}}$ denotes the total number of reference tracks passing through the detector's active area.

Chapter 5

Simulation of Charge Sharing Concept

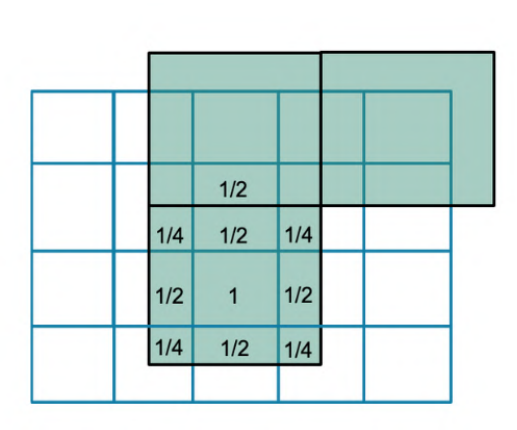
The fundamental challenge in developing a charge-sharing pixilated read-out arises from the ability to determine position uniquely through the charge-sharing process. This requires understanding the charge sharing mechanism on a geometric level, independent of complex physical processes. Since the principle heavily uses geometry in reconstructing the position (Gnanvo et al. 2023) uniquely, a physics-based simulation may obscure the fundamental limitations and capabilities of the chosen geometry. A discrete simulation approach deliberately eliminates these physical complexities to focus on the geometric aspects of charge sharing across pixelated read-out layers. By understanding the fundamental limits imposed purely by read-out geometry and charge sharing patterns, detector designs and reconstruction algorithms can better optimized.

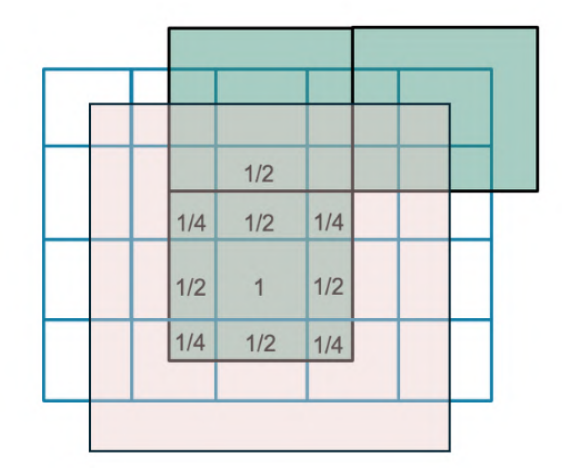
5.1 Charge Sharing

The capacitive coupling facilitates a specific pattern in which charge is shared between the pixels, both in a layer and across multiple layers. The detectors used in this thesis have adopted pixels with a symmetric square-shaped geometry arranged in a hierarchical structure, where each successive layer uses pixels twice the size of the preceding layer. This scaling results in a 4:1 area ratio, where each larger pixel overlaps with nine smaller pixels from the adjacent layer (Figure 5.1).

The charge transfer between layers follows the following rules based on geometric overlap in an ideal scenario:

- Center pixel: The smaller pixel whose center coincides with the larger pixel's center transfers 100% of its collected charge
- Edge pixels: The four pixels sharing an edge with the larger pixel boundary each transfer 50% of their charge, distributed equally between the two adjacent larger pixels





(a) Two-layer charge sharing

(b) Three-layer charge sharing

Figure 5.1: Schematic representation of the charge-sharing pattern between adjacent pixelated layers. The smaller pixels (layer n) transfer charge to larger pixels (layer n+1) according to their geometric overlap: center pixels transfer 100%, edge-adjacent pixels transfer 50%, and corner-adjacent pixels transfer 25% of their collected charge. (a) Two-layer configuration showing charge transfer between consecutive layers. (b) Three-layer configuration demonstrating the hierarchical charge sharing across multiple layers.

• Corner pixels: The four pixels positioned at the corners each transfer 25% of their charge, distributed equally among the four adjacent larger pixels

This specific geometric pattern encodes the position uniquely in the read-out layer based on the charge spread and the intensity of the charge.

5.2 Simulation Framework

The simulation framework implements a simplified charge deposition and propagation model through the pixelated detector structure. The pixel structure is selected such that it simulates the exact geometry of the real detectors in terms of the number of layers and pixel placements. This is important since both the five-layer pad and the three-layer pad have an asymmetry at the edge. The bigger pixels are not completely covered by the smaller pixels on the layer above. This leads to a situation where more area is covered by the bigger pixels than the smaller pixels, leading to an asymmetric charge coupling at the edges. The simulated graph also allows for an inspection of individual layers. An inspection of each layer and the reconstructed position is possible. The selected geometry is such that the smallest layer has 146×146 pixels in layer 1, 74×74 in layer 2, 37×37 in layer 3, 19×19 in layer 4, and 10×10 in layer 5.

The approach consists of three principal components, as explained in the following sections:

5.3 Simulation Results 41

5.2.1 Charge Deposition Model

The simulation treats charge deposition as a discrete event occurring at a specific position (x_0, y_0) on the finest-pitch pixel layer. This initial charge distribution is represented as a local event, where the charge is in abstract units and only the number is essential for the purposes of simulation. This is the case since, devoid of any physical effects, charges do not mean anything in the context of the simulation. Multiple cases are studied where an event is only a single pixel, a collection of symmetric pixels with a symmetric charge distribution, or a Gaussian distribution with appropriate cuts on charge to simulate a more realistic distribution. Also, randomly generated noise is added to see how the behavior changes with noise.

5.2.2 Charge Propagation Algorithm

The deposited charge propagates through successive layers according to the geometric coupling rules established in section 5.1. For each layer transition, the algorithm:

- 1. Identifies the pixels in layer n containing charge
- 2. Determines the geometric overlap with pixels in layer n+1
- 3. Distributes charge according to the overlap fractions
- 4. Iterates until reaching the final read-out layer

5.2.3 Position Reconstruction

The simulation employs the charge-weighted centroid method (Equation 4.2) to reconstruct the interaction position from the charge distribution on the read-out layer. This reconstructed position (x_{rec}, y_{rec}) is then compared with the true deposition position (x_0, y_0) to evaluate reconstruction accuracy. The reconstructed position is shifted by half a pixel on each layer to ensure that the position is at the center of the pixel. Meaningful cuts on charges are applied before reconstruction.

5.3 Simulation Results

In this section, the results are looked at, particularly how uniquely the hit position of a particle can be determined after a reduction in the number of layers, how good can the hit position can be resolved in the case of the presence of noise and how this changes when different types of signals are chosen to depict the realistic scenario.

5.3.1 Single Pixel Performance

Charge sharing across a large number of pixels and layers can be quite difficult to visualize. So, starting with the simplest case of single pixel hits in the smallest layer, the basic working principle of charge sharing can be understood. Looking at Figure 5.2, a charge of 3700 is given to a single pixel at pixel number (72,72) on layer 1. This position is selected such that it represents the center of the detector.

It can be seen how the charges are coupled through different layers from Figure 5.2. In the next step, the same charge is now moved one pixel to the right along the same row (72,73) Figure 5.3. A clear difference can be observed in how unique the new position is from looking at the pixel that the charge couples to and the intensity of the charge on the pixels. This difference in the intensities and positions lets a unique determination of position through the charge-weighted centroid method (Equation 4.2). An insight into the charge-coupling process can be gained through this exercise.

5.3.2 Symmetric Pixel Performance

Understanding the basic nature of charge coupling, a more complicated case can be considered. 9 pixels are considered for the exercise, which have a symmetric charge distribution in both X and Y directions. This has a pseudo-Gaussian shape, with deterministic charge values. Looking through Figure 5.4, the charge coupling can be noticed across multiple layers. A minimum number of 2 pixels on layers 3 and 4 pixels on layer 5 is expected.

5.3 Simulation Results 43

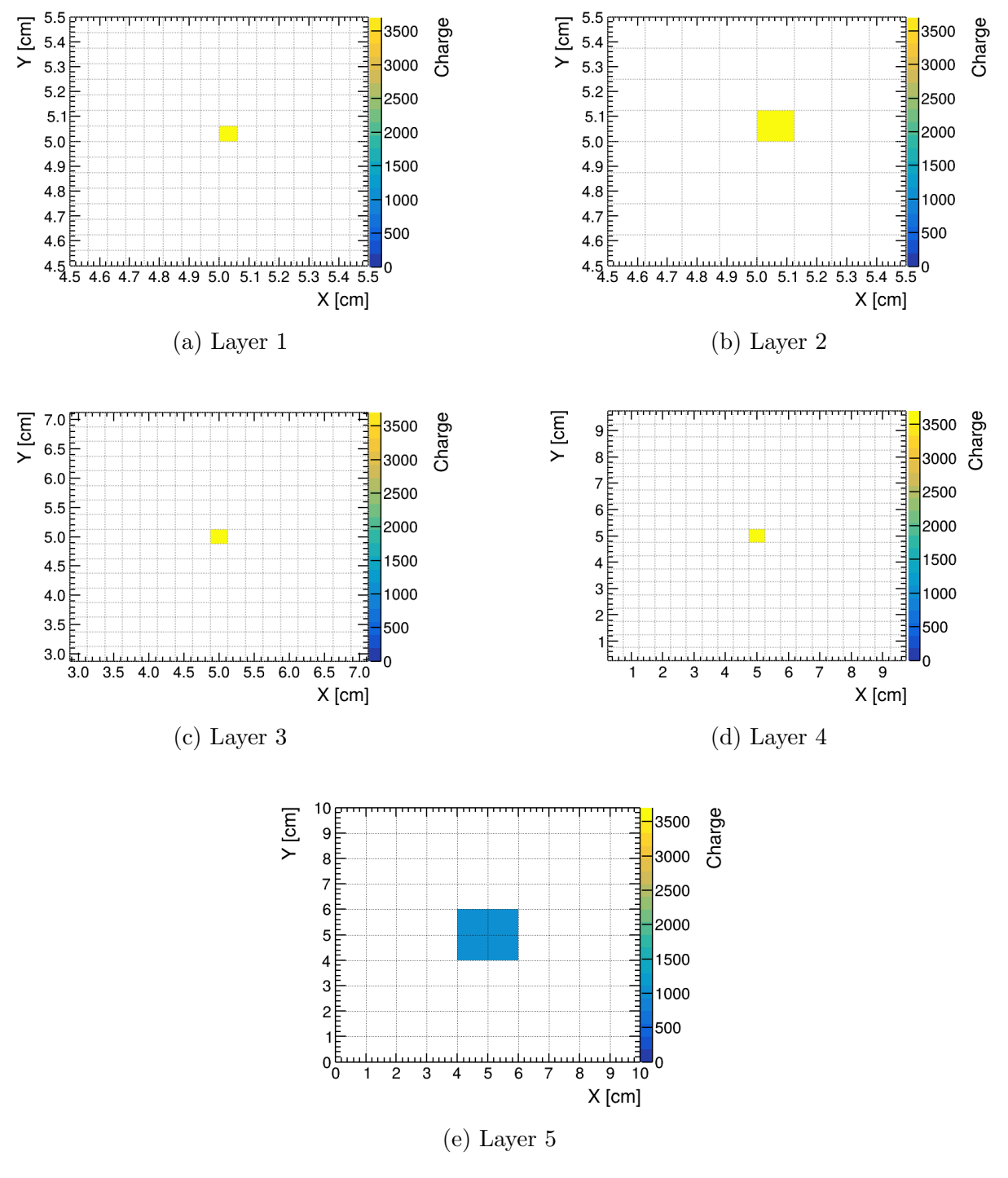


Figure 5.2: Charge distribution across all five layers for a single pixel hit at position (72,72) on Layer 1. The charge of 3700 units propagates through successive layers according to the geometric coupling rules, demonstrating the unique charge-sharing pattern that enables position reconstruction.

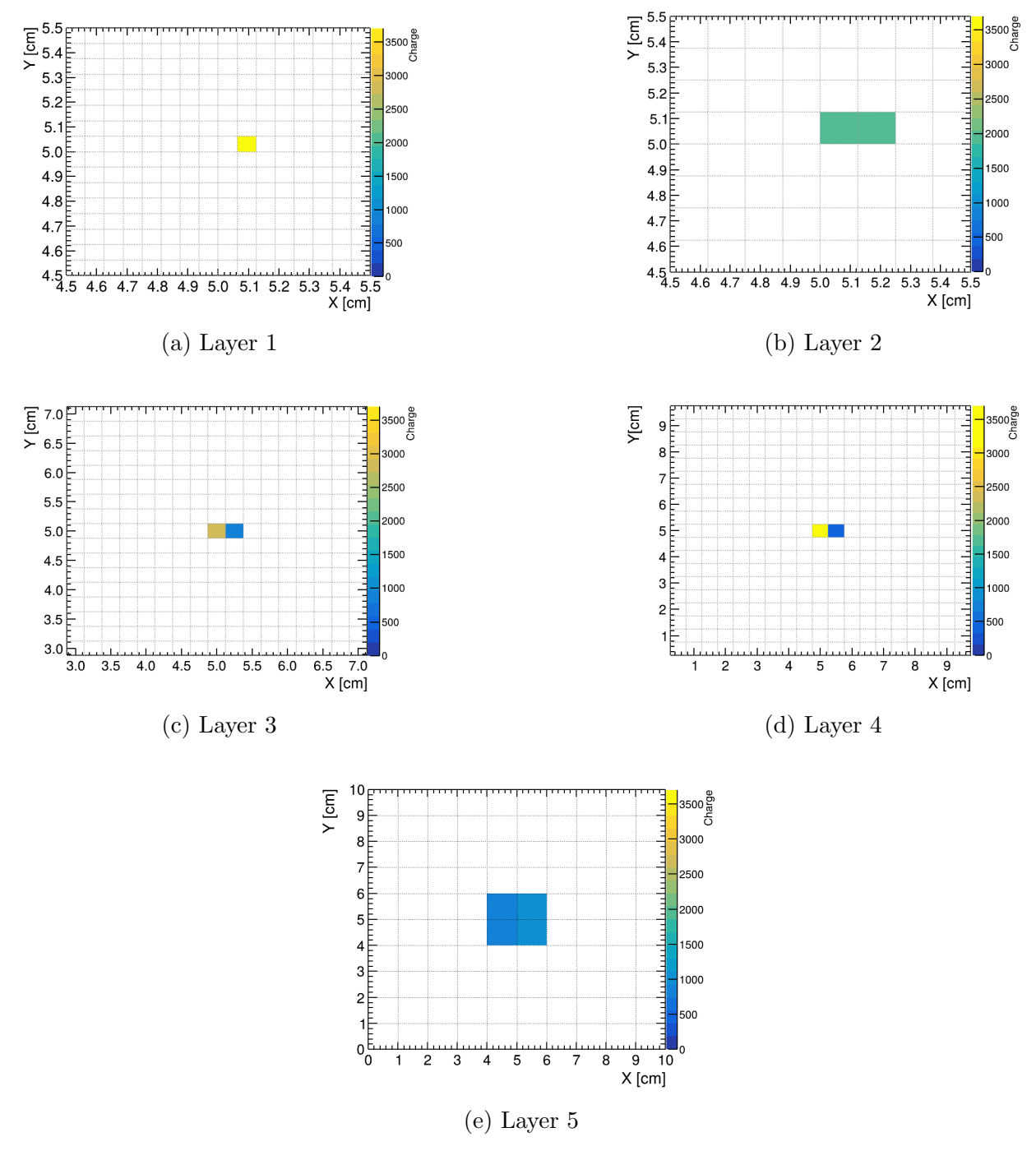


Figure 5.3: Charge distribution across all five layers for a single pixel hit at position (72,73) on Layer 1. The charge of 3700 units propagates through successive layers, showing a distinctly different charge-sharing pattern compared to Figure 5.2, demonstrating the uniqueness of position encoding through charge distribution.

5.3 Simulation Results 45

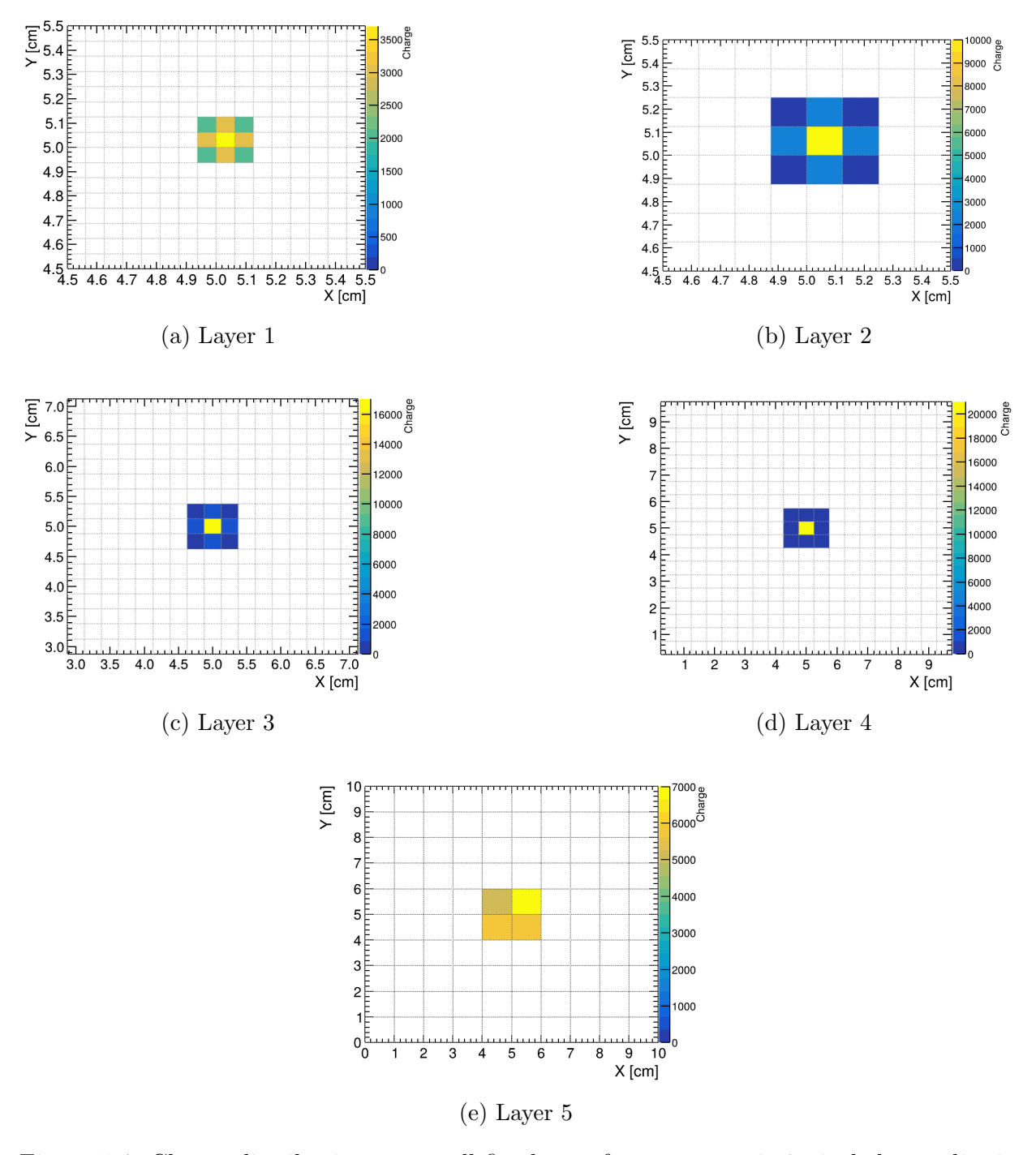


Figure 5.4: Charge distribution across all five layers for a symmetric 9-pixel charge distribution centered at position (72,72) on Layer 1. The pseudo-Gaussian charge propagates through successive layers according to the geometric coupling rules, demonstrating the charge-sharing pattern for extended charge distributions.

5.3.3 Gaussian Distribution Performance

Following the analysis of single pixel (subsection 5.3.1) and symmetric distribution cases (subsection 5.3.2), the more complex scenario of Gaussian charge distributions is considered. This provides a more realistic representation of actual particle interactions, where charge deposition follows a continuous spatial distribution rather than discrete pixel assignments.

The charge distribution is described by a two-dimensional Gaussian function:

$$Q(x,y) = A \cdot \exp\left(-\frac{(x-x_0)^2 + (y-y_0)^2}{2\sigma^2}\right)$$
 (5.1)

where A: amplitude (peak charge value in arbitrary units) (x_0, y_0) : center position of the charge distribution (true interaction point) σ : standard deviation determining the spatial spread of the charge cloud Q(x, y): charge density at position (x, y).

To implement this continuous distribution on the discrete pixel grid, the charge deposited in each pixel (i, j) is calculated by integrating the Gaussian function over the pixel area:

$$Q_{i,j} = \int_{x_i}^{x_{i+1}} \int_{y_i}^{y_{j+1}} Q(x, y) \, dx \, dy$$
 (5.2)

For computational efficiency, this integral is approximated using the charge density at the pixel center multiplied by the pixel area, which provides sufficient accuracy for the spatial scales considered in this study. An amplitude of 3700 for the simulation is selected to match the other cases. A standard deviation of 1 is selected to represent the actual size of the charge cloud, so as not to run into computational limits in evaluating the integral. The pixel positions are also the same to allow for a direct comparison. The charge coupling can be understood in the Figure 5.5. Since a Gaussian distribution asymptotically goes to zero, meaningful cuts on the charges need to be implemented to eliminate any values that do not contribute to meaningful data. In this case, a cut on the charge value at 2 is selected on layer 1.

The charge can be moved diagonally across the pixel plane and the position can be reconstructed (See Figure 5.6). A perfect reconstruction of the position is observed in the absence of noise. 5.3 Simulation Results 47

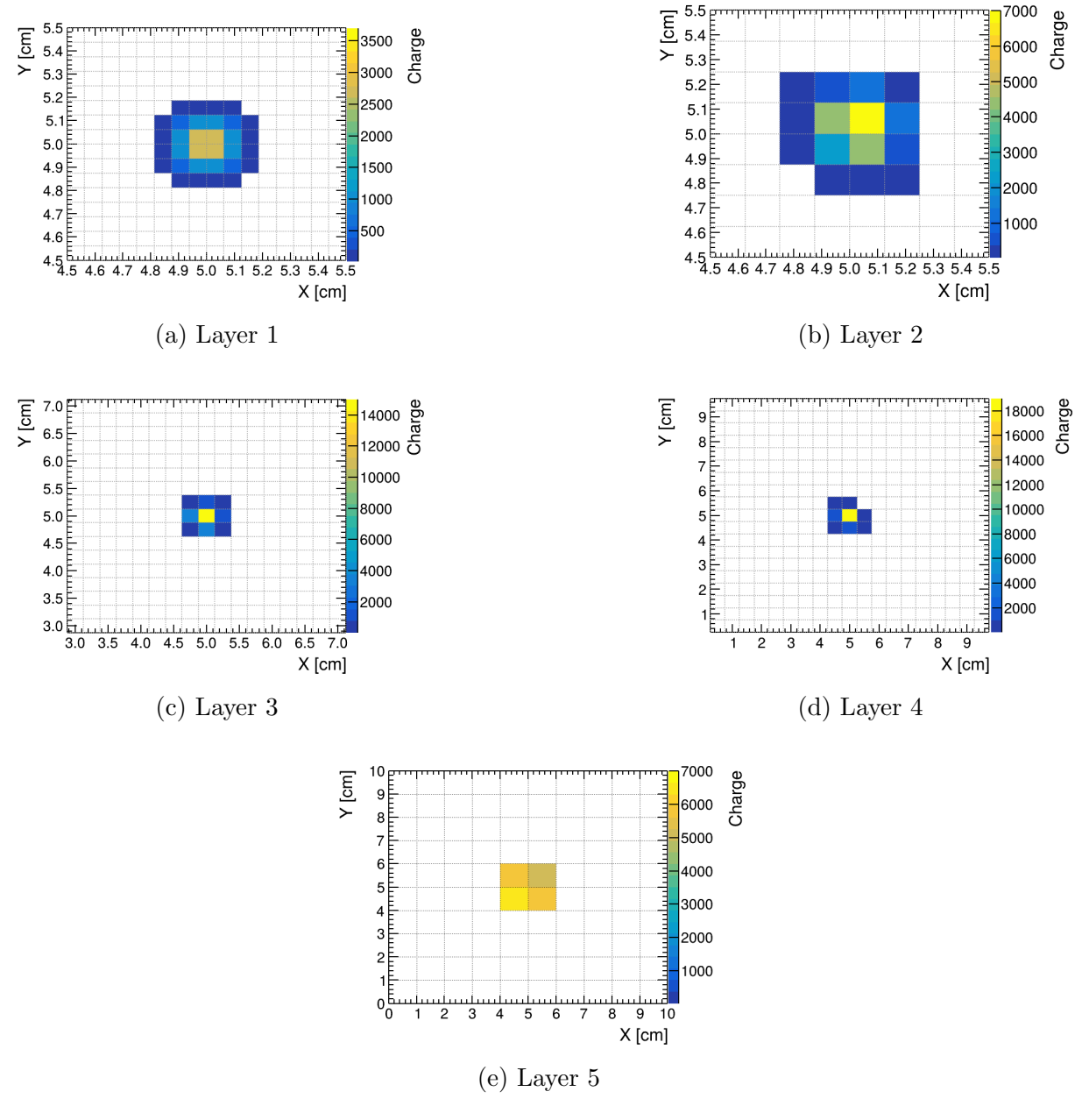


Figure 5.5: Charge distribution across all five layers for a Gaussian charge distribution (amplitude = 3700, σ = 1) centered at position (72,72) on Layer 1. The continuous charge distribution propagates through successive layers according to the geometric coupling rules, demonstrating how realistic particle interactions with spatial charge spread are encoded through the hierarchical pixel structure.

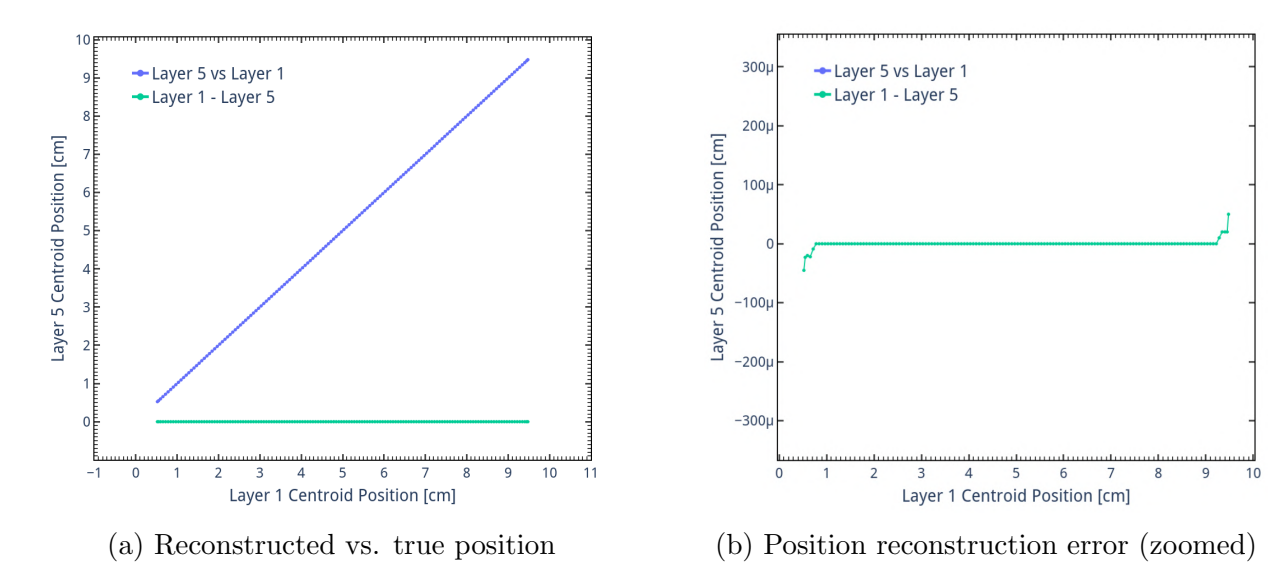


Figure 5.6: Position reconstruction for Gaussian charge distributions moved diagonally across the detector plane. (a) Comparison between true position on Layer 1 and reconstructed cluster position on Layer 5. (b) Zoomed view of the position reconstruction errors showing perfectly reconstructed position. The effects at the edges are visible due to the absence of symmetry at the edges.

5.3.4 Noise Profile

Noise is a fundamental part of any detector setup. To understand how well the signal can be disentangled from the noise, it is of utmost importance to understand how the noise couples across multiple pixel layers. Following the discussion in section 5.1, since each bigger pixel is shared by nine smaller pixels, the noise from these nine pixels will also couple to the bigger pixel. Since this is repeated over multiple layers, the noise adds up to high values. This can be seen from Figure 5.7. A randomly generated noise between 0 and 3 is taken. This choice is such that when the noise couples up, this contributes to approximately 8% of the signal. The pixels along the edges have a lower noise value compared to the others. This stems from the fact that the pixels along the edges in the bigger layer are not shared between 9 pixels on the smaller layer, rather four. The noticeable increase in the noise level starting from a maximum value of 3 in layer 1 to 400 in layer 5 is seen.

5.3 Simulation Results 49

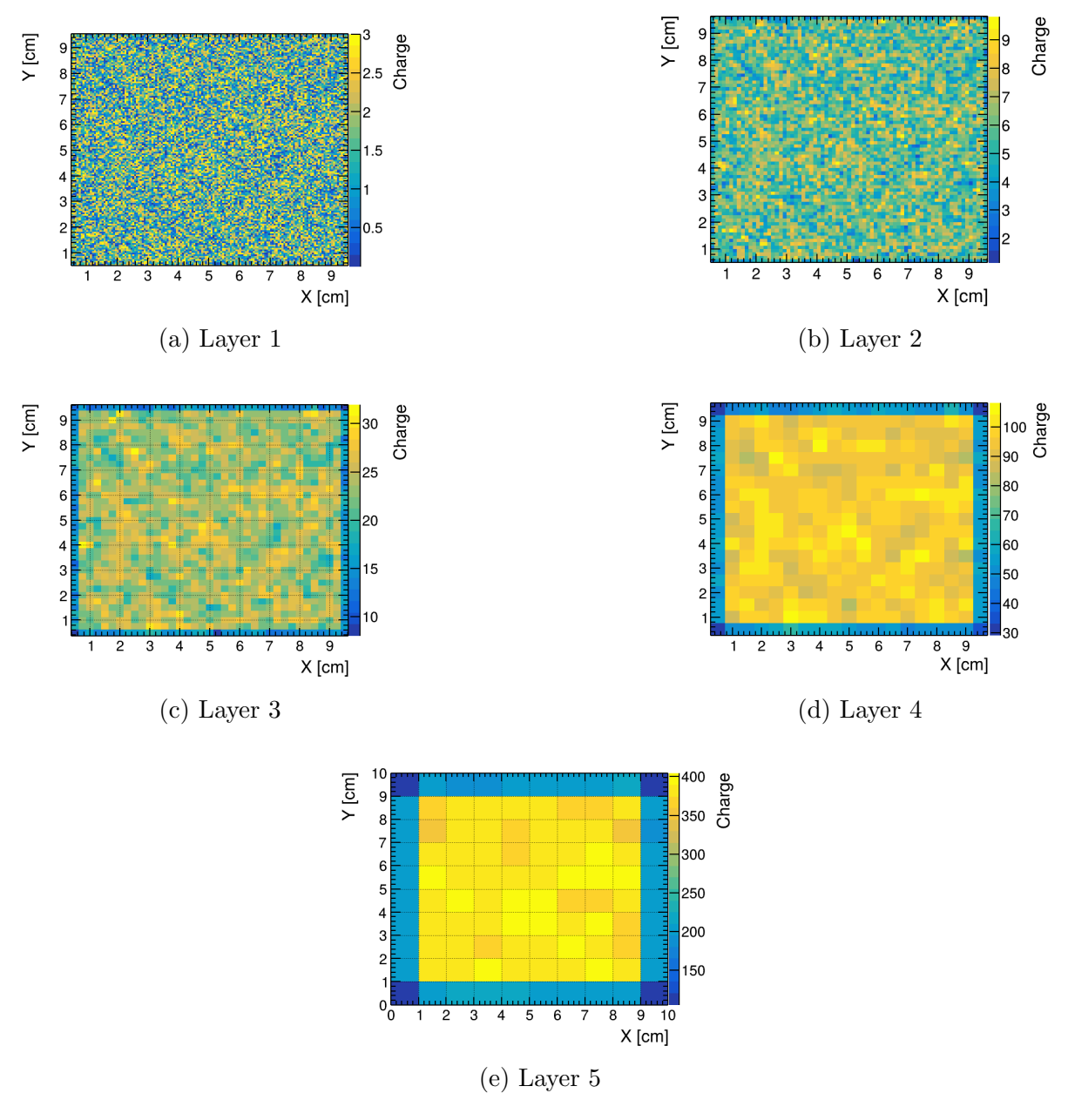


Figure 5.7: Noise propagation across all five layers showing the accumulation of random noise (0-3 units per pixel on Layer 1) through the hierarchical pixel structure. The noise level increases progressively from Layer 1 to Layer 5 due to the geometric coupling rules, with edge pixels showing reduced noise values compared to central pixels due to fewer contributing smaller pixels in the coupling process.

5.3.5 Gaussian Distribution with Noise

Building on the pure Gaussian distribution analysis (subsection 5.3.3) and the noise characterization, the more realistic scenario where Gaussian-distributed charge deposition occurs in the presence of noise is looked at. This combined analysis helps us understand the limitations of the detector in reconstructing the position in an ideal scenario with noise present.

The total charge in each pixel is given by:

$$Q_{i,j}^{\text{total}} = Q_{i,j}^{\text{signal}} + N_{i,j} \tag{5.3}$$

Where $Q_{i,j}^{\text{signal}}$ represents the Gaussian-distributed signal charge (Equation 5.2) and $N_{i,j}$ represents the random noise contribution uniformly distributed between 0 and 3 arbitrary units.

The charge distribution across all five layers when a Gaussian signal (amplitude = 3700, $\sigma = 1$, centered at pixel (72,72)) is combined with the noise profile shown in Figure 5.7. Progressive charge spreading is observed according to the geometric coupling rules, while noise accumulation from multiple contributing pixels begins to affect the charge distribution uniformity in layers 2-5. The reconstruction accuracy in the presence of noise is evaluated by systematically moving the Gaussian distribution center diagonally across the detector plane. The reconstructed positions are calculated using the charge-weighted centroid method (Equation 4.2) with appropriate charge threshold cuts applied to suppress noise contributions.

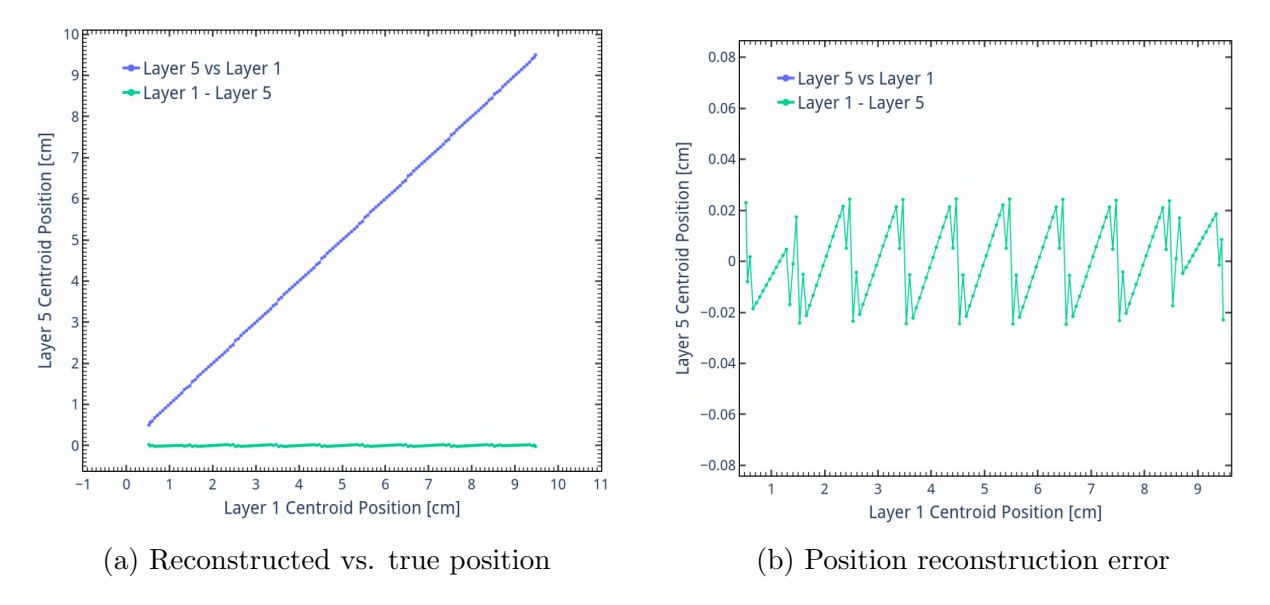


Figure 5.8: Position reconstruction performance for Gaussian distribution with noise on Layer 5 (five-layer configuration). (a) Comparison between true position (Layer 1) and reconstructed cluster position (Layer 5). (b) The difference between reconstructed and true positions shows systematic reconstruction errors introduced by noise.

5.3 Simulation Results 51

Figure 5.8 shows the relation between the true position on Layer 1 and the reconstructed cluster position on Layer 5 when noise is included. Unlike the ideal cases presented in subsection 5.3.2 and subsection 5.3.3, deviations from perfect reconstruction are now observed. The position difference plot (Figure 5.8b) reveals that reconstruction errors are introduced by the noise. A systematic pattern can be observed with an interval of one pixel. This occurs at the center of the pixel because of the shift in position discussed in subsection 5.2.3.

Since two detector configurations are tested—one with five layers and the other with three layers, a comparison of their reconstruction performance in the presence of noise is made. The three-layer configuration exhibits the same systematic reconstruction pattern observed in the five-layer detector, but with notably reduced error amplitude.

Figure 5.9 demonstrates the reconstruction performance of the three-layer configuration. The position difference plot (Figure 5.9b) reveals the same one-pixel interval pattern observed in the five-layer detector. However, the error amplitude is significantly reduced due to the decreased noise accumulation through fewer layer transitions.

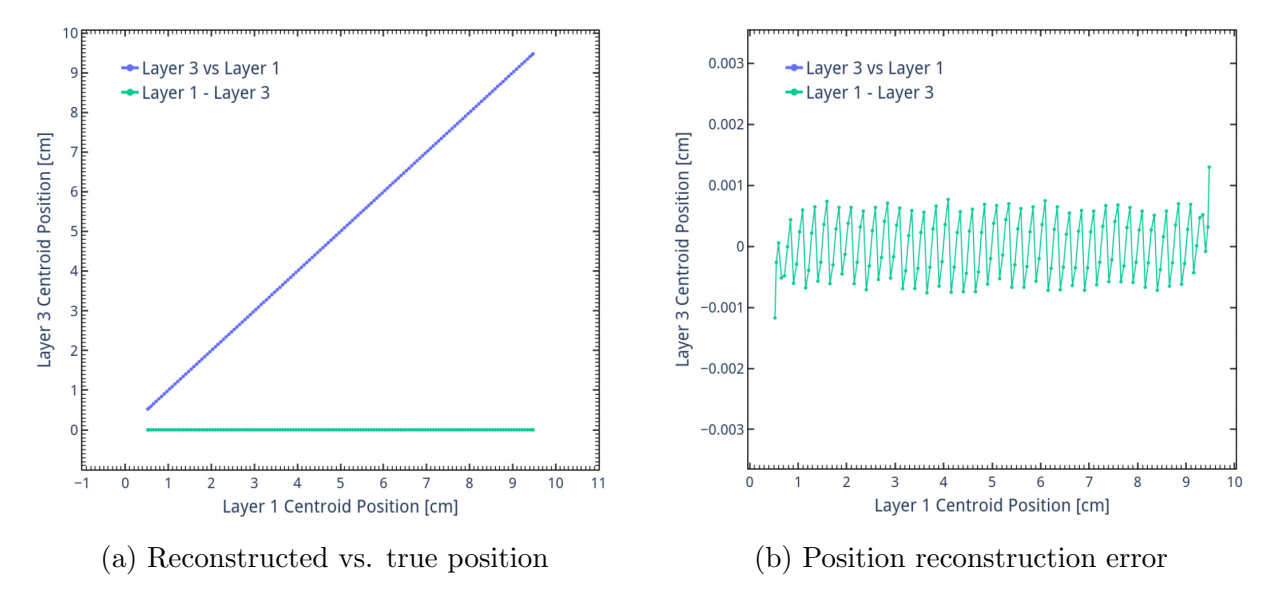


Figure 5.9: Position reconstruction performance for Gaussian distribution with noise on Layer 3 (three-layer configuration). (a) Comparison between true position (Layer 1) and reconstructed cluster position (Layer 3). (b) Difference between reconstructed and true positions showing the same systematic pattern as the five-layer configuration but with reduced amplitude.

The reduced error amplitude in the three-layer configuration can be attributed to:

- Reduced noise accumulation: Fewer layer transitions result in less noise propagation from Layer 1 to the readout layer
- Lower charge dispersion: The shorter propagation path minimizes charge spreading, improving the signal concentration at the readout layer

• Edge Effects: The noise becomes more pronounced at the edges, further away from the center of the Gaussian charge, since a Gaussian distribution asymptotically goes to zero. This leads to an incorrectly reconstructed centroid position. Since the five-layer configuration couples to a larger number of pixels on layer one compared to the three-layer configuration, these Gaussian edges contribute more to the five-layer configuration.

This comparison demonstrates that while both configurations exhibit the same systematic reconstruction behavior dictated by the pixel geometry, the three-layer detector reduces the reconstruction error. More layers might lead to more reconstruction errors, subsequently negatively affecting the resolution of the detector.

Impact of Charge Threshold Cuts

The reconstruction accuracy in the presence of noise is dependent on the application of appropriate charge threshold cuts. To demonstrate this dependency, the reconstruction performance is compared with and without noise suppression cuts.

Without charge threshold cuts, all pixels containing any charge—including those with only noise contributions—are included in the centroid calculation. This leads to a bias in position reconstruction, as noise-only pixels far from the true signal location distort the weighted average. The Gaussian tails, which carry minimal signal charge, become indistinguishable from noise, causing the reconstruction to incorrectly calculate the position.

Figure 5.10 illustrates the difference in reconstruction performance. With appropriate charge cuts (Figure 5.10a), the reconstructed positions maintain a linear relationship with the true positions, exhibiting only the systematic one-pixel periodic error discussed previously. In contrast, without cuts (Figure 5.10b), the reconstruction shows severe non-linear behaviour. The noise contributions from pixels throughout the detector plane pull the reconstructed centroid away from the true position.

This analysis underscores that charge threshold selection represents a critical optimization parameter in the detector operation. The threshold must be set high enough to eliminate noise contributions while remaining low enough to preserve the genuine signal information contained in the Gaussian distribution tails.

5.4 Conclusion 53

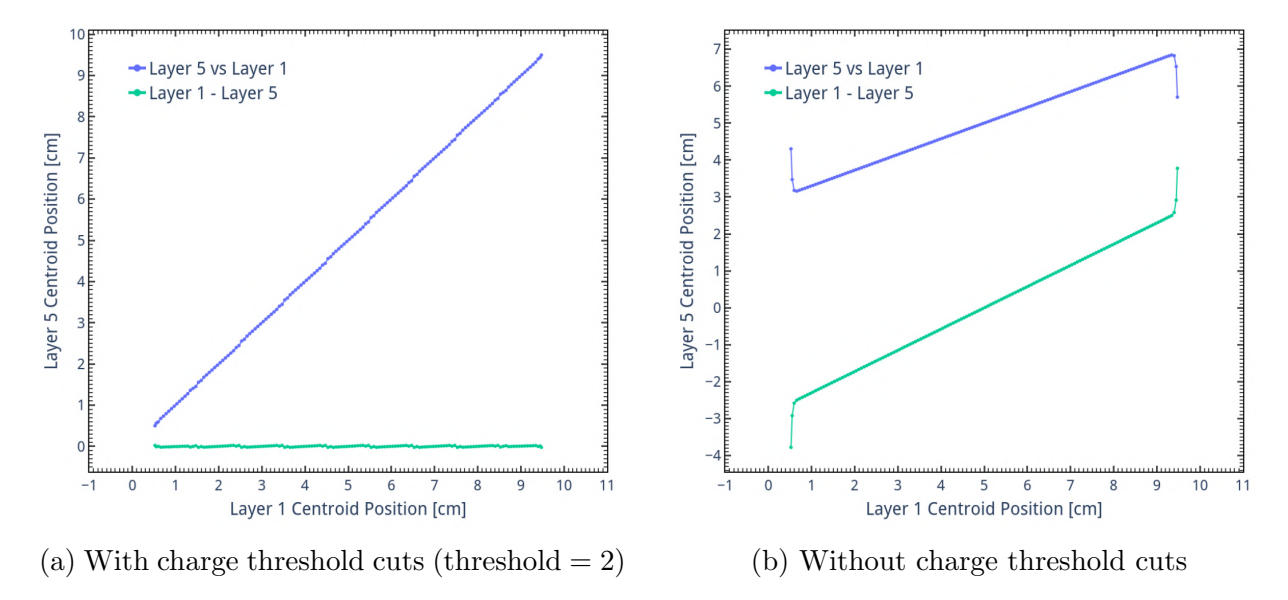


Figure 5.10: Comparison of position reconstruction on Layer 5 for Gaussian distribution with noise. (a) Reconstruction with charge threshold cuts successfully eliminates noise contributions, maintaining linear correlation between true and reconstructed positions. (b) Reconstruction without cuts shows severe position distortion due to noise pixels being incorrectly included in the centroid calculation, resulting in non-linear reconstruction behavior.

5.4 Conclusion

This simulation study demonstrates that the charge-sharing concept successfully enables unique position determination through hierarchical pixelated readout layers. The geometric coupling enables unique charge distribution patterns to reconstruct position unambiguously using the charge-centroid method. In ideal noise-free conditions, perfect position reconstruction is achieved for both three-layer and five-layer configurations. However, when noise is introduced, systematic reconstruction errors with characteristic one-pixel periodicity arises. This effect is amplified with the number of pixel layers, with five-layer configuration showing larger error amplitudes than the three-layer configuration. These findings validate the charge-sharing principle as a viable approach for channel reduction while maintaining unique position reconstruction.

Chapter 6

Characterization with ⁵⁵Fe source and Cosmic Muons

Characterization of a novel detector architecture requires different measurements to probe various aspects of the detector's performance across energy scales. This chapter presents a characterization study of the charge-sharing PAD. To this end, both ⁵⁵Fe X-ray source and cosmic muon measurements have been performed. Together, these two methodologies provide an understanding of the detector's response characteristics and operational parameters through their different physical properties. The main decay product of ⁵⁵Fe source is the characteristic monoenergetic 5.9 keV X-rays. This energy is deposited in highly localized regions through photoelectric absorption. This can be used for precise energy resolution measurements, gas gain properties, and charge sharing at a well-defined energy scale. A complete absorption of low-energy X-rays occurs within a few millimeters of gas, creating point-like charge clouds ideal for studying the energy resolution and giving an estimate of the intrinsic spatial resolution. In contrast, cosmic muons are minimum ionizing particles (MIPs) that traverse the entire detector volume, depositing energy uniformly along their tracks. This property of cosmic muons allows for the investigation of position reconstruction capabilities and efficiency over the entire geometry of the detector.

6.1 Characterization with ⁵⁵Fe

The 55 Fe source, through electron capture decay, emits characteristic X-rays from the daughter 55 Mn nucleus. The primary emissions are the Mn K $_{\alpha}$ line at 5.90 keV (25.4% branching ratio) and the K $_{\beta}$ line at 6.49 keV (2.99% branching ratio). At these energies, the photoelectric effect dominates the photon interactions with the detector gas (see subsection 2.1.2), producing nearly monoenergetic photoelectrons. The dominant peak corresponds to the K $_{\alpha}$ line at 5.90 keV, where the full photon energy is absorbed (blue curve in Figure 6.1). An additional peaks arise from Argon K-shell fluorescence: when a K-shell electron is ejected when an Argon atom in the detector gas volume is ionized by the X-ray photon, an L-shell electron transitions to K-shell emitting a photon. If this

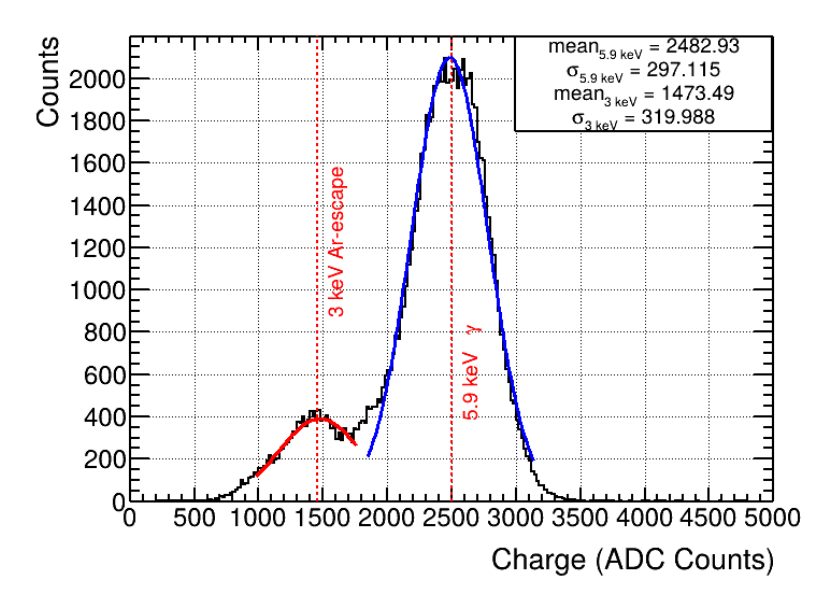


Figure 6.1: Cluster charge spectrum showing the two characteristic ⁵⁵Fe peaks with Gaussian fits. The spectrum displays the 5.9 keV full-energy peak and the 3.0 keV escape peak, fitted with individual Gaussian functions (red curves). At optimal anode voltages, both peaks are clearly resolved, enabling accurate energy calibration through the theoretical energy ratio of 1.97.

photon does not interact with the detector gas, the resulting Argon K_{α} photon (2.9 keV) may escape the detector volume, producing escape peaks at $E_{K\alpha\text{-esc}} = 3 \text{ keV}$ (red curve in Figure 6.1) and $E_{K\beta\text{-esc}} = 3.59 \text{ keV}$. The detectors in this thesis can only resolve the $E_{K\alpha} = 5.9 \text{ keV}$ peak and the $E_{K\alpha\text{-esc}} = 3 \text{ keV}$. The ratio between these characteristic energies provides a calibration relationship, which is a measure of how well the detector can resolve the two peaks:

$$\frac{E_{\gamma}}{E_{\text{escape}}} = \frac{5.9 \text{ keV}}{3 \text{ keV}} = 1.97$$
 (6.1)

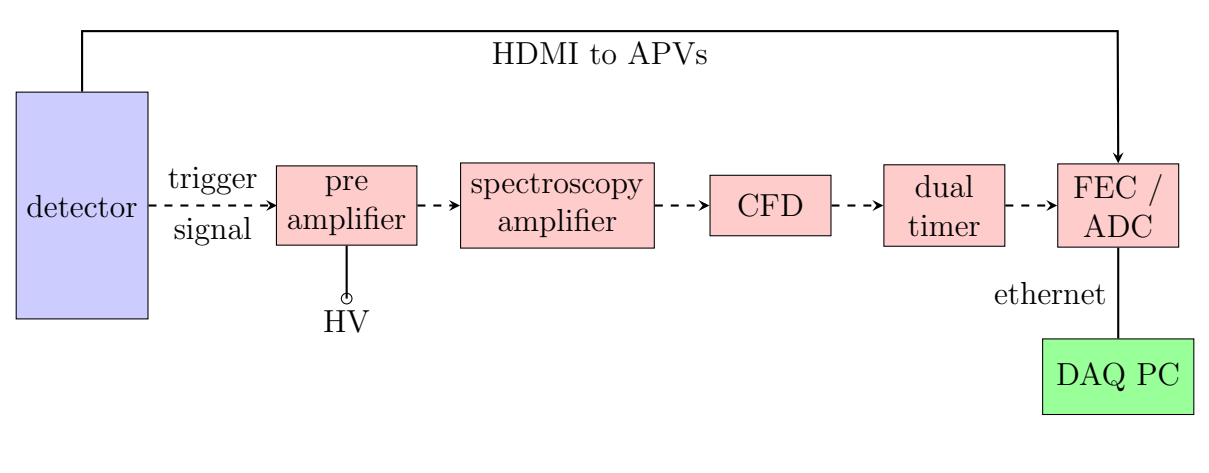
Another important calibration metric is the energy resolution res_E is defined as:

$$\operatorname{res}_{E} = \frac{\sigma_{5.9 \text{ keV}}}{\operatorname{mean}_{5.9 \text{ keV}}} \tag{6.2}$$

where a gaussian fit to the 5.9 keV peak gives σ and mean values. The energy resolution measures the broadening of the charge distribution around the peak. Typical values around 10% is observed for Micromegas detectors.

6.1.1 Measurement Setup

 55 Fe source was positioned above the detector cathode for the measurement. Two detectors were tested: the three-layer PADH and the five-layer PAD5. A high-voltage supply was connected to the anode and the cathode. The micromesh was grounded via a pre-amplifier. The positive current signal from the grounded mesh is pre-amplified and connected to a spectroscopy amplifier, where the signal is further amplified and shaped. This signal is passed on to a low threshold discriminator and is converted into a Nuclear Instrumentation Standard (NIM) pulse. This initially short NIM pulse is extended in time ($\approx 100 \mu s$) by a dual timer and is used as a trigger signal. The pulse is extended to stop more triggers before the data from one trigger is completed. This extended NIM signal provides the external trigger for the SRS. Using this trigger, the FEC reads signals directly from the APV25 boards on the detector. The DAQ acquires this signal for further analysis.



----: trigger signal
————: data signal

Figure 6.2: Schematic of the trigger and DAQ setup used for measurements with a 55 Fe γ -source. The pre-amplified micro-mesh signal is used for triggering. This pre-amplified signal is sent via LEMO cables to NIM modules. A dual timer extends the trigger pulse to prevent new triggers before processing the current event. The APV25 boards are connected via HDMI cables to the ADC card, which interfaces with the FEC (PCIe). The DAQ PC reads out the FEC via ethernet and receives the trigger signal from the dual timer.

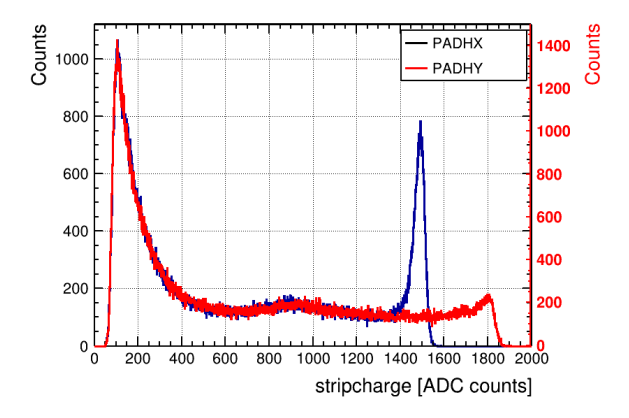
6.1.2 PADH

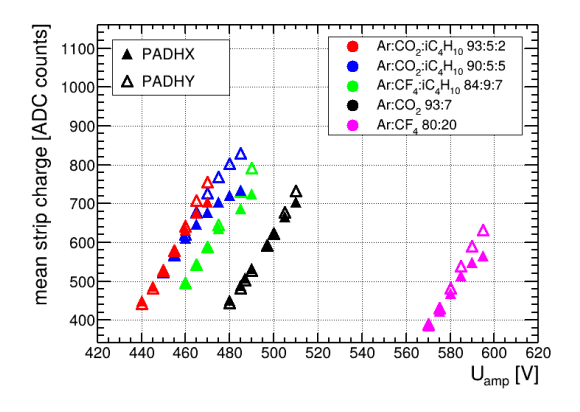
The hybrid pixel three-layer PADH detector was characterized using ⁵⁵Fe X-rays to evaluate its energy response and resolution capabilities. The 170 channels of the detector were read using two APV25 front-end boards. Different gas mixtures were used to characterize the performance of the optimal gas. Throughout the measurements, the APV25 board along the X direction saturated around 1500 ADC counts, while the APV25 board along the Y

direction saturated later, around 1800 ADC counts. Since the PADH has a hybrid design, it is essential to notice that the charges measured along the X and Y directions are the charges on the same pixel. To obtain a complete idea of the charge deposited by a particle, the cluster charges along X and Y directions should be added together.

Pulse Height Analysis

The saturation effect of the readout electronics is visible in Figure 6.3. The early onset of saturation along the X direction is clearly visible from the truncated charge at 1500 ADC counts, while the Y strips start to truncate the charge around 1800 ADC counts and saturate later. This indicates that the charges pixels receive, cannot be completely reconstructed since the charges along X are truncated around 1500 ADC counts, while this reconstruction is still possible for Y. Figure 6.3b clearly indicates this saturation effect, for different gases. The X charges can be seen to plateau, while a steady increase in charges along the Y direction is observed.



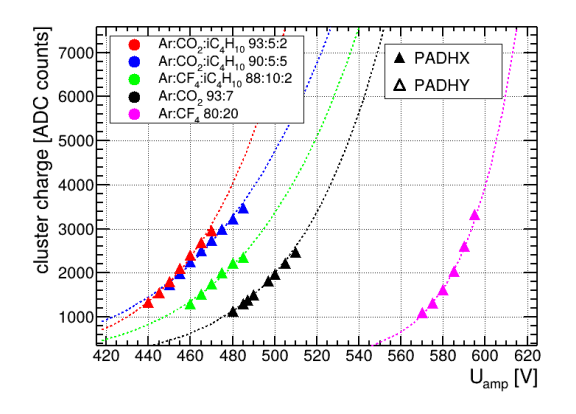


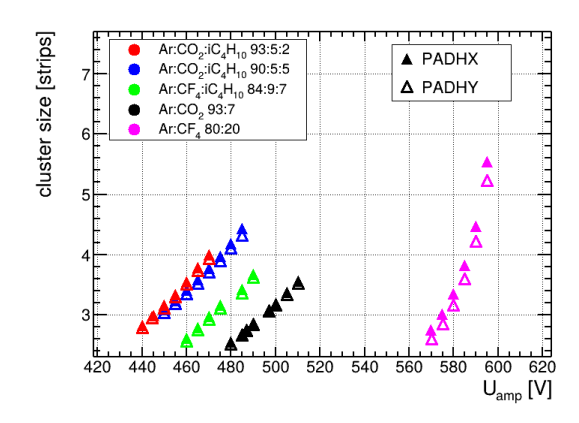
- (a) Strip charge distribution for a single ⁵⁵Fe measurement
- (b) Mean strip charge vs anode voltage for different gas mixtures

Figure 6.3: Strip charge analysis for PADH detector characterization. (a) Strip charges for a single ⁵⁵Fe measurement showing strip charges in both X and Y directions. (b) Mean strip charge as a function of anode voltage for various Ar-based gas mixtures. Saturation of X strips is visible as the charges plateau while charges in Y strips continues to scale.

Figure 6.4a shows the cluster charges along the X direction plotted against anode voltages. It follows the double exponential behavior, following the gas gain Equation 2.14. The cluster charges along the Y direction exhibit the same trend and can similarly be fit to a double exponential curve. Saturation of the charges along the X direction is visible from the deviation of the mean charges below the fitted curve at higher voltages. Higher cluster charges could be achieved with $Ar:CO_2:iC_4H_{10}$ in 93:5:2 and 90:5:5 vol.% under stable conditions. For similar strip charges, similar pulse heights are expected. The $Ar:CF_4$ (80:20 vol.%) mixture produces higher cluster charges despite lower strip charges compared

to other gas mixtures (see Figure 6.3b). This is due to the scintillation effects in CF₄-based gases. The scintillation light is emitted during the initial ionization in the drift region and during the ionization in the amplification region (Brunbauer et al. 2025). The emitted photons, with energies of $\mathcal{O}(1\text{--}10~\text{eV})$ are far below the 5.9 keV ⁵⁵Fe X-rays. These low energy photons interact with detector materials to produce additional photoelectrons. After amplification, these create low-amplitude background signals that expand the cluster size without proportionally increasing the strip charge. This effect grows with voltage: at low amplification voltages, photoelectrons from scintillation remain below detection threshold, but as voltage increases, they become detectable, causing cluster size to rise steeply (see Figure 6.4) while strip charge grows only gradually.





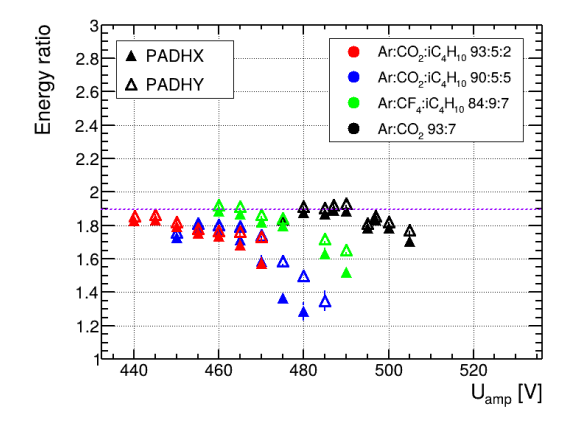
- (a) Cluster charge with double exponential fit
- (b) Cluster size evolution with anode voltage

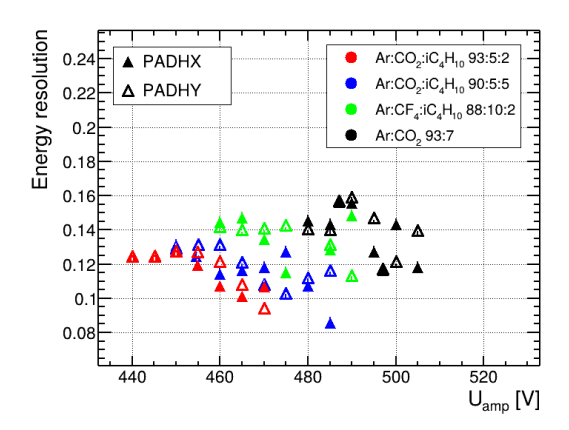
Figure 6.4: Cluster characteristics as a function of anode voltage for 55 Fe source. (a) X-direction cluster charge following the double exponential gas gain (Equation 2.14). Saturation of the charges is visible from the deviation of the mean charges below the curve at higher anode voltages except for Ar:CF₄ (80:20 vol.%) mixture. (b) Cluster size showing the increase with increasing. The huge increase in the cluster size for Ar:CF₄ (80:20 vol.%) mixture points to the scintillation effect.

Scintillation effects in Ar:CF $_4$ in 80:20 vol.% prevents proper resolution of the 55 Fe peaks. Hence this mixture was excluded from energy resolution analysis.

At very high cluster charge values, the energy ratio gets worse (see Figure 6.5a). This is because the two peaks cannot be resolved anymore due to the saturation of the APVs. The energy resolution initially improves with increasing amplification voltage as the gain increases. Figure 6.5b shows the energy resolution plotted against anode voltage for various gas compositions. The best resolutions are achieved with Ar:CO₂:iC₄H₁₀ in 93:5:2 and 90:5:5 vol.% ratios, due to their higher cluster charges. The PADH measurements reveal direction-dependent saturation thresholds (1500 ADC counts for X-direction, 1800 for Y-direction), due to the early saturation of the APV along the X direction. When too many strips saturate, the reconstructed pulse height clips the actual signal and underestimates it, resulting in energy resolution. This effect is more pronounced in the X direction, as

evidenced by earlier inflection points in the energy resolution curves and larger deviations from the theoretical energy ratio at high voltages.





(a) Energy ratio between the 5.9 keV and 3.0 keV peaks as a function of anode voltage. The theoretical value of 1.97 is shown as a dashed line. Different colors represent different gas mixtures. Deviation from the theoretical value at high voltages due to saturation can be seen, which are particularly pronounced in the X direction.

(b) Energy resolution as a function of anode voltage for various gas mixtures. The resolution improves with voltage until saturation effects degrade performance. Inflection points indicate optimal operating voltages without saturation for different gas compositions.

Figure 6.5: Energy performance characteristics of the PADH detector using $^{55}{\rm Fe}$ X-ray source.

6.1.3 PAD5

The five-layer PAD5 detector was read out using one APV25 front-end board in master configuration, owing to the 100 readout channels.

Gas mixture tests were conducted with primarily two gas mixtures: $Ar:CO_2:iC_4H_{10}$ in 93:5:2 vol.% and $Ar:CO_2:iC_4H_{10}$ in 90:5:5 vol.%. The enhanced stability and the higher achievable pulse heights motivated this choice.

Pulse Height Analysis

The cluster charge evolution as a function of anode voltage has been presented in Figure 6.6. The expected double exponential behavior, characteristic of gas avalanche multiplication processes described by Equation 2.14, was clearly observed across the full operational range. The observed cluster charge values with both gas mixtures are similar to the values observed for PADH (adding up the charges along X and Y). For PAD5, only one value

of charge is measured, in contrast to the directional measurements of the PADH detector, since the purely pixel readout measures the complete charge received by each pixel.

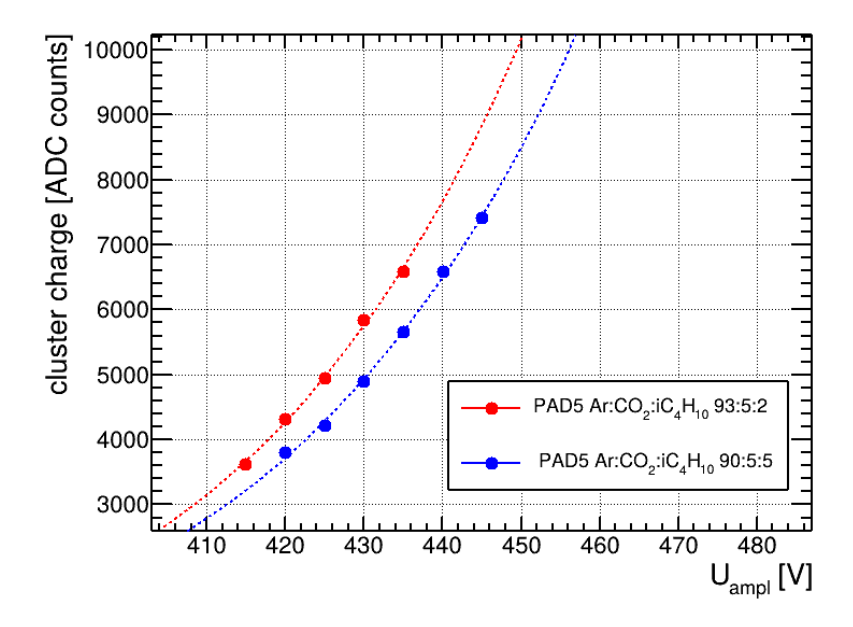


Figure 6.6: Cluster charge as a function of anode voltage for PAD5 detector with $Ar:CO_2:iC_4H_{10}$ gas mixtures (93:5:2 and 90:5:5 vol.%). The double exponential behavior follows the gas gain equation (Equation 2.14).

Figure 6.7 shows the energy ratio and resolution as functions of anode voltage. The energy ratio, determined through Gaussian fitting of the cluster charge spectra following the same methodology as PADH, shows good agreement with the theoretical value of 1.97. The energy resolution res_E , calculated using Equation 6.2, improves with increasing amplification voltage as expected.

PAD5 achieves superior energy resolution compared to PADH, reaching values below 10%. This improvement stems from the detector's five-layer charge-sharing architecture, where each readout pixel on layer 5 collects signals from 9⁴ (6561) smaller pixels on layer 1. This hierarchical structure ensures almost complete charge collection since charges generated in the smallest pixels cascade through intermediate layers before being collected at the readout layer. The extensive charge sharing minimizes signal loss, resulting in better energy resolutions than PADH.

6.1.4 X-Ray imaging with ⁵⁵Fe

To demonstrate the spatial resolution capabilities of the PAD detectors, X-ray transmission imaging was performed using a three-dimensional test object. A 3D-printed replica of "The Scream" by Edvard Munch, fabricated from PLA filament, served as an absorption mask positioned between the ⁵⁵Fe source and the detector (see Figure 6.8). The print thickness

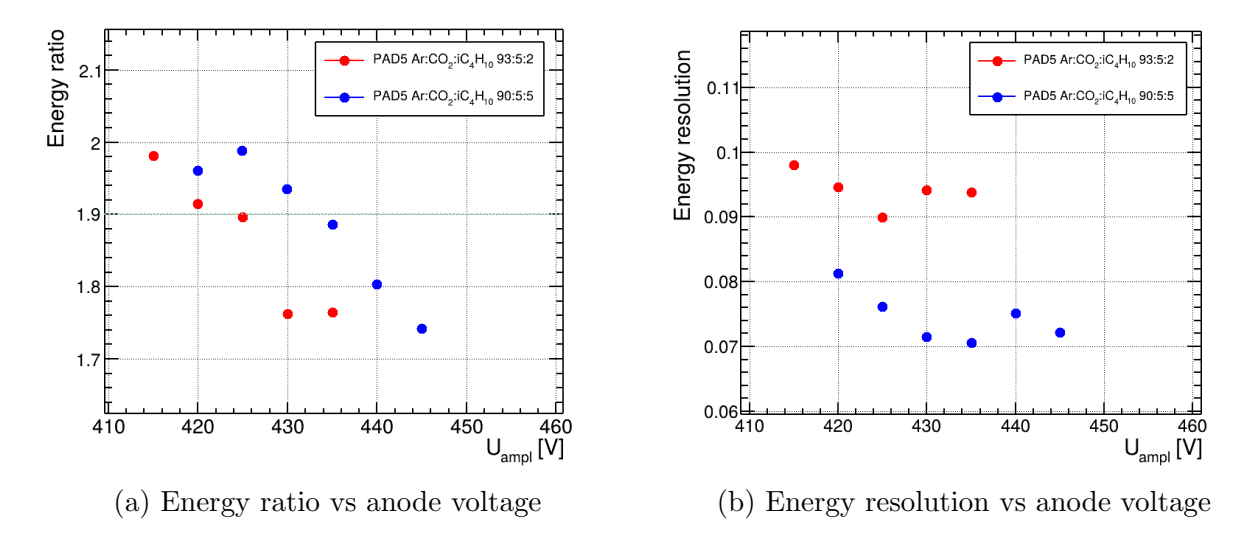
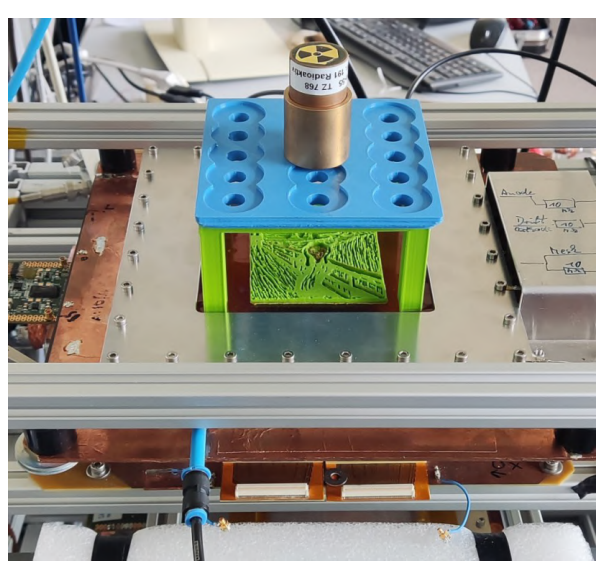


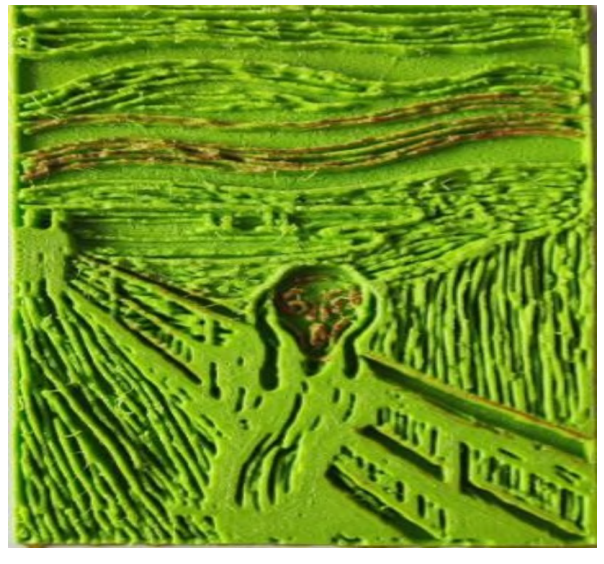
Figure 6.7: Energy metrics for PAD5 detector with Ar:CO₂:iC₄H₁₀ gas mixtures. (a) Energy ratio between the 5.9 keV and 3.0 keV peaks showing good agreement with the theoretical value of 1.97. (b) Energy resolution as a function of anode voltage, demonstrating superior performance with values below 10% at optimal operating conditions. The improved resolution compared to PADH is attributed to the five-layer charge-sharing architecture enabling complete charge collection.

was modulated from 0.5 mm to 2.9 mm, with thinner regions corresponding to lighter areas of the original painting and thicker regions to darker areas, creating a spatially varying X-ray absorption pattern.

The ⁵⁵Fe source was positioned to illuminate the detector through the 3D print. X-ray transmission through the material exhibited strong thickness dependence. This differential absorption produced a two-dimensional intensity pattern at the detector plane, effectively encoding the image information in the spatial distribution of detected photons.

Position reconstruction is shown in Figure 6.9. Support pillar locations appear as distinct inefficient regions in the reconstructed image. These structures, which prevent gas amplification in their immediate vicinity, were clearly resolved as localized efficiency drops in the photon distribution, further confirming the sub-millimeter position resolution capability of the PAD architecture. With the PADH detector, spatial resolution exceeds the pillar dimensions (approximately 200 µm diameter) and the features of the 3D print can be resolved with excellent accuracy. For the PAD5 detector, we cannot resolve all the features of the 3D print completely. This already gives an estimate of the resolution of the detector, where PAD5 is not able to resolve over 200 µm, which corresponds to the size of the pillars. For both the detectors, there are no inefficient areas where the source has illuminated the detector surface.





(a) Measurement setup

(b) 3D-printed absorption mask for "The Scream" by Edvard Munch

Figure 6.8: Test object for X-ray imaging demonstration. (a) Measurement setup for X-ray imaging.(b) 3D-printed PLA absorption mask with thickness modulation from 0.5 mm to 2.9 mm, where lighter regions of the painting correspond to thinner sections (higher X-ray transmission) and darker regions to thicker sections (lower transmission).

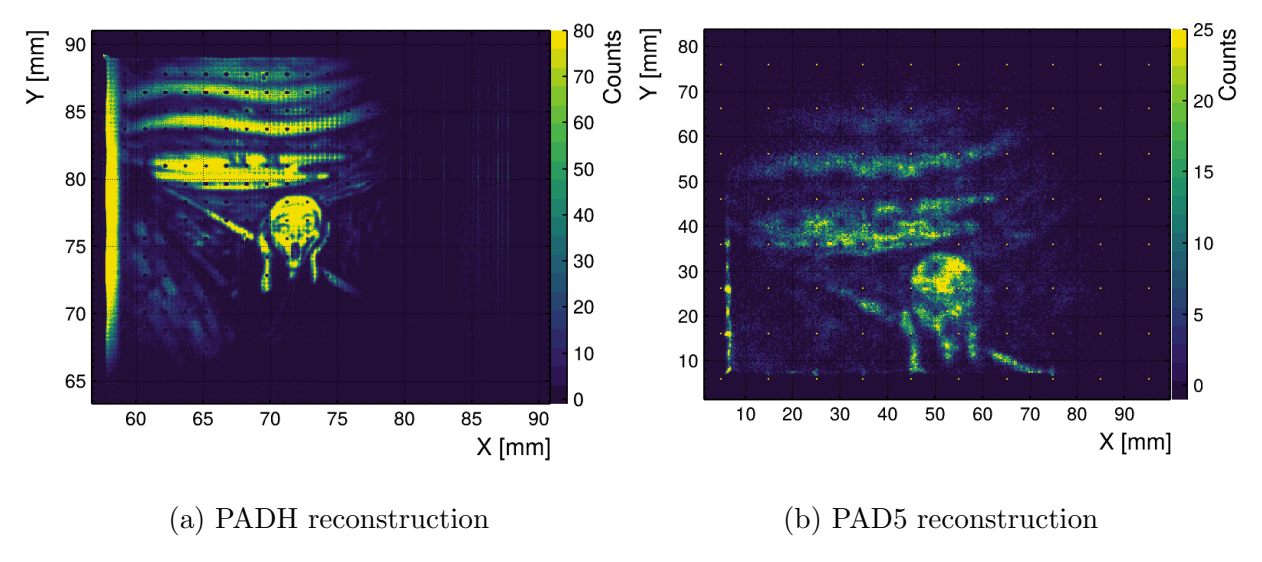
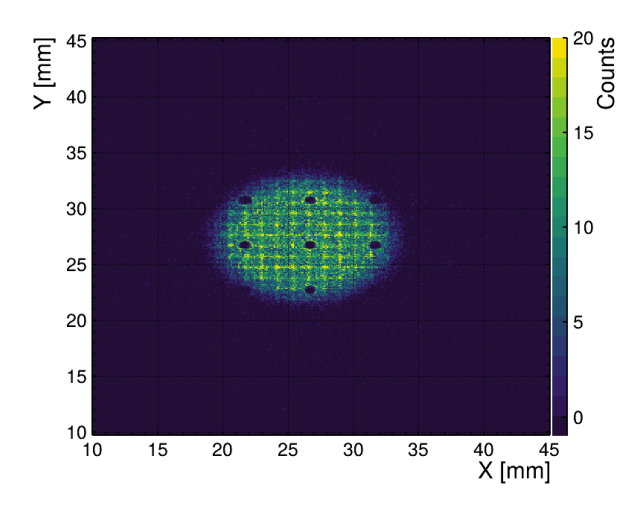
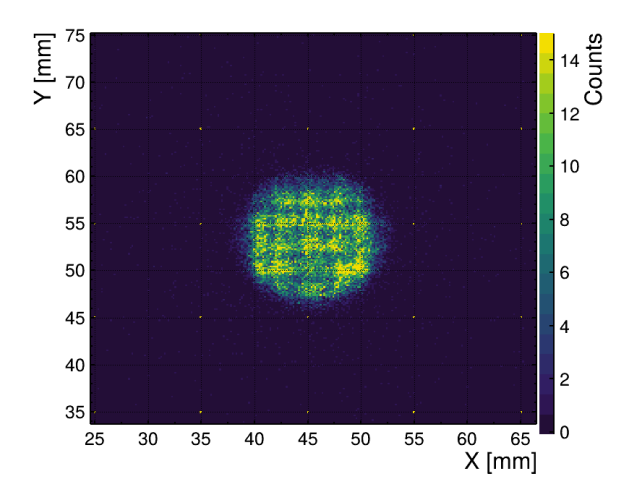


Figure 6.9: X-ray transmission imaging of "The Scream" test object using ⁵⁵Fe source with PAD detectors. (a) PADH detector reconstruction showing superior spatial resolution with clearly distinguishable features. The pillars can be identified as black dots in the picture. (b) PAD5 detector reconstruction with lower spatial resolution due to larger pixel size.

6.2 Hit Multiplicity with ⁵⁵Fe

The 2D hit map for PADH and with ⁵⁵Fe source (see Figure 6.10) show preferential positions in spatial reconstruction. This systematic behavior would be expected to affect the spatial resolution since some positions are reconstructed more often than the others, leading to a bias in the reconstructed position. This effect will be discussed in chapter 7 where the detector has been characterized with mono-energetic muons and precision tracking has been done. In Figure 6.10b, singular yellow dots are seen across the area of the detector. These points corresponds to pixel centers, again confirming the preferential position reconstruction.





(a) 2D hit map for PADH detector showing preferential position reconstruction patterns. The distribution reveals systematic clustering of reconstructed positions that correlate with the underlying 1.2 mm pixel pitch structure.

(b) 2D hit map for PAD5 detector exhibiting similar preferential position patterns. The 1.0 cm pixel pitch cannot be distinctly recogonized due to the small irradiated area. But structures within the pixel is more pronounced compared to the PADH.

Figure 6.10: Comparison of 2D hit maps for ⁵⁵Fe X-ray interactions showing preferential spatial reconstruction positions. Both detector architectures exhibit systematic clustering patterns. The higher resolution of the PADH detector is evident from the absence of observable pillars as dark spots in PAD5.

6.3 Characterization with Cosmic Muons

Cosmic muons provide a complementary characterization method to the localized energy deposits from ⁵⁵Fe sources. These naturally occurring minimum ionizing particles (MIPs) originate from cosmic ray interactions in the upper atmosphere and reach ground level with a typical flux of approximately 1 muon/cm²/minute (Particle Data Group et al.

2022). Cosmic muons generate extended ionization tracks with characteristic energy loss described by the Bethe-Bloch formula. The energy loss along muon tracks produces the characteristic Landau distribution in pulse height spectra, providing a metric for detector calibration. They traverse several detector layers and can be used to determine position resolution of the test detectors by using reference detectors for tracking.

6.3.1 Measurement Setup

The measurement setup consists of a tracking telescope configuration with two 2D DLC Micromegas detectors of dimensions 10×10 cm² as trackers, PAD5 detector and PADH detector of dimensions 10×10 cm² and two scintillators of dimensions 9×9 cm² stacked vertically, with the PAD5 and PADH detectors positioned between two reference tracking detectors (See Figure 6.11).

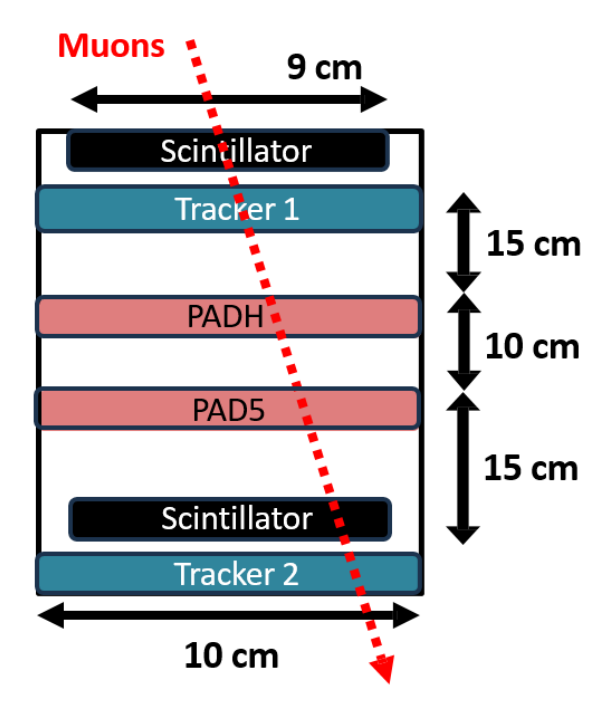


Figure 6.11: Experimental setup of the cosmic muon tracking telescope showing the vertical stack of four detectors (two Micromegas trackers, PAD5, and PADH) positioned between the top and bottom scintillator paddles. The detectors are mounted in a rigid aluminum frame to ensure coarse alignment upto a few mm precision.

An external trigger was provided by the scintillators positioned above and below the detector stack, operating in coincidence mode to select muon candidates that pass through both scintillators. The trigger logic is illustrated in Figure 6.12. This trigger logic effectively suppresses random backgrounds, ensuring genuine cosmic muon events. Given the active area of the scintillators and the geometric acceptance of $\pm 20^{\circ}$, a trigger rate for all incident angles was measured to be 0.07 Hz.

Near-perpendicular tracks were chosen by implementing a stringent angular selection criterion of $\pm 5^{\circ}$ from perpendicular incidence, during data analysis. This selection was enforced to reconstruct muon trajectories without the effect of non-homogeneous ionization along inclined tracks. However, the observed event rate after angular selection was significantly lower.

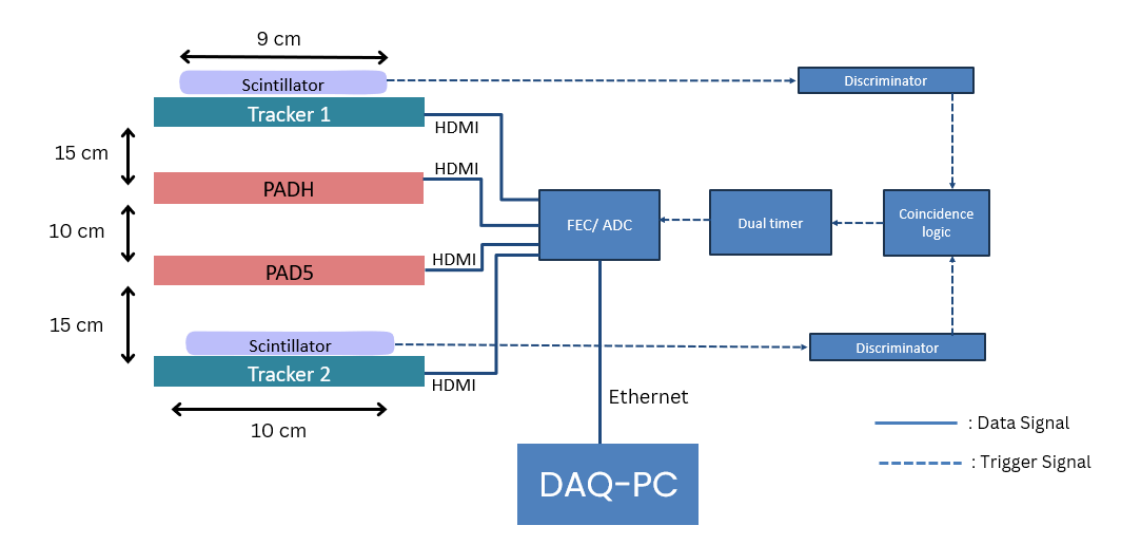


Figure 6.12: Schematic diagram of the trigger logic for cosmic muon measurements. The coincidence unit requires simultaneous signals from both scintillators.

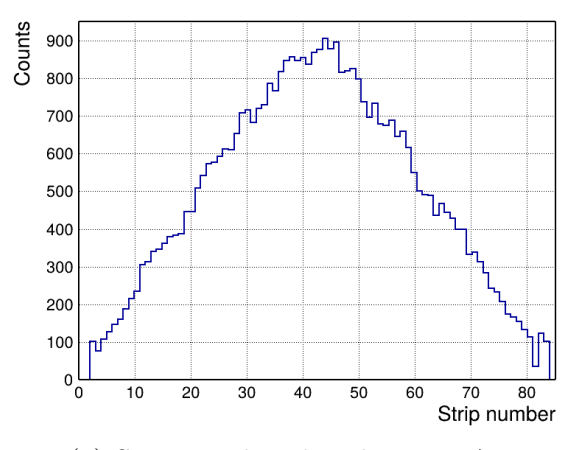
6.3.2 Cosmic Muon Measurements

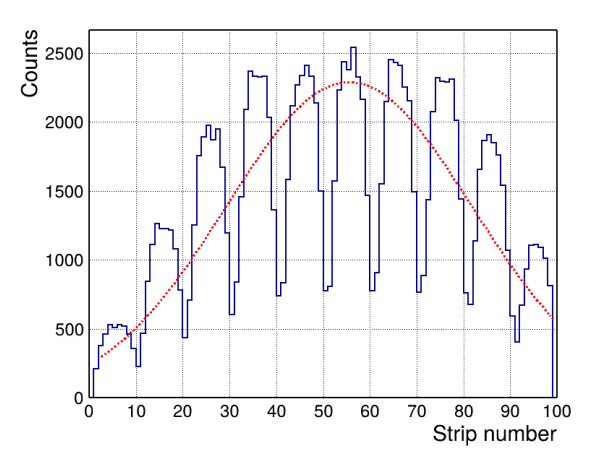
Cosmic muon measurements were conducted on both detector configurations to characterize their performance with minimum ionizing particles. The PADH detector was tested with two gas mixtures: $Ar:CO_2$ (93:7 vol.%) and $Ar:CO_2:iC_4H_{10}$ (90:5:5 vol.%), while PAD5 measurements were performed exclusively with $Ar:CO_2:iC_4H_{10}$ (90:5:5 vol.%). The addition of isobutane as a tertiary quenching component in the $Ar:CO_2:iC_4H_{10}$ mixture demonstrates significant operational advantages, enabling scaling to substantially higher cluster charge values at correspondingly lower operational voltages due to enhanced quenching efficiency.

For the PADH detector, clustering methods analogous to strip detectors were employed to reconstruct muon hit positions. The PAD5 detector, with its 10 mm readout pixels, employed the DFS algorithm for pixel clustering as the primary reconstruction method (see section 4.3).

Figure 6.13 shows the spatial distribution of muon hits in the PADH and PAD5 detectors. The strip number distribution demonstrates higher hit density in the central region due to the detector's positioning within the telescope setup, where coincidence scintillators preferentially trigger on muons passing through the detector center because of the angular

acceptance cone. The intermittent structures in the PAD5 distribution is because of the way the pixels are read-out along each column. An envelope over this pattern will again give us the central hit pattern in PAD5 detector.





- (a) Strip number distribution PADH
- (b) Strip number distribution PAD5

Figure 6.13: Spatial distribution of cosmic muon hits in PADH and PAD5 detectors with an angular acceptance of $\pm 20^{\circ}$. (a) Strip number distribution in PADH detector demonstrating higher hit density in the central region due to detector positioning within the telescope setup. (b) Strip number distribution in PAD5 detector showing similar central enhancement with intermittent structures due to column-wise pixel readout patterns. The red curve shows the envelope over the distribution, which is the hit pattern of the detector.

Pulse Height Analysis

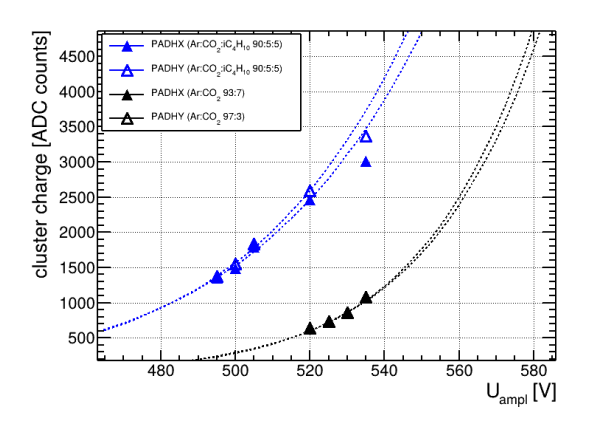
The cluster charge distribution for cosmic muon events follows the characteristic double exponential gas gain behavior described by Equation 2.14. Figure 6.14 presents the cluster charge evolution as a function of anode voltage for both PADH and PAD5 detectors.

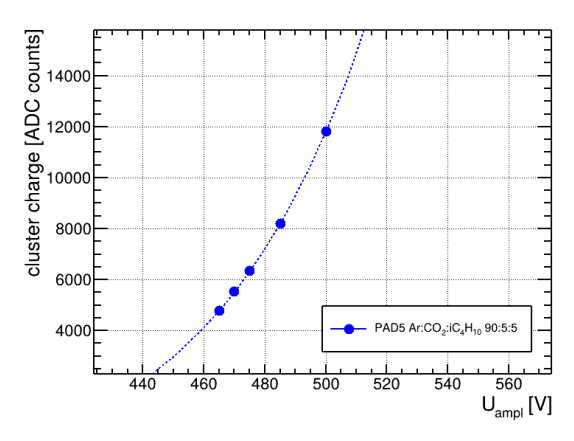
The five-layer charge-sharing structure of PAD5 produced substantially higher cluster

charges compared to those observed in PADH. This enhancement is attributed to the increased charge collection from 9⁴ shared pixels in the smallest layer compared to the 9² shared pixels in PADH and a wider drift gap leading to more primary ionization.

Spatial Resolution And Efficiency

Spatial resolution is determined by the centroid method (section 4.3). The measurements reveal distinct performance characteristics between the two detector configurations. The PADH detector, with its three-layer charge-sharing architecture, achieved superior spatial resolutions compared to PAD5. This improvement can be attributed to a finer pixel pitch in the collection layer for PADH (0.3 mm) compared to PAD5 (0.625 mm) and a reduced





- (a) PADH detector cluster charge evolution
- (b) PAD5 detector cluster charge evolution

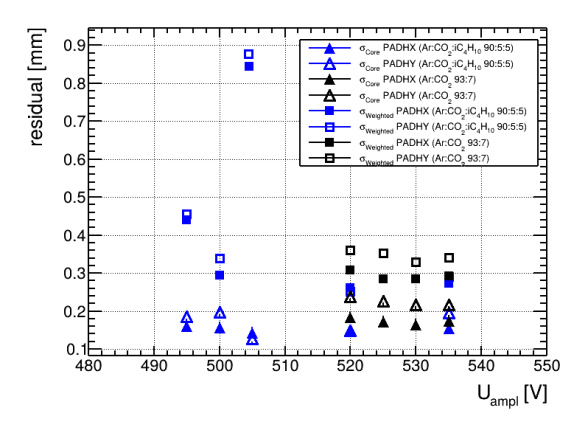
Figure 6.14: Cluster charge evolution as a function of anode voltage for cosmic muon events. (a) PADH detector measurements with Ar:CO₂ (93:7 vol.%) and Ar:CO₂:iC₄H₁₀ (90:5:5 vol.%) mixtures, demonstrating superior performance of the isobutane-containing mixture. (b) PAD5 detector measurements with Ar:CO₂:iC₄H₁₀ (90:5:5 vol.%) mixture, showing substantially higher cluster charges due to the five-layer charge-sharing architecture.

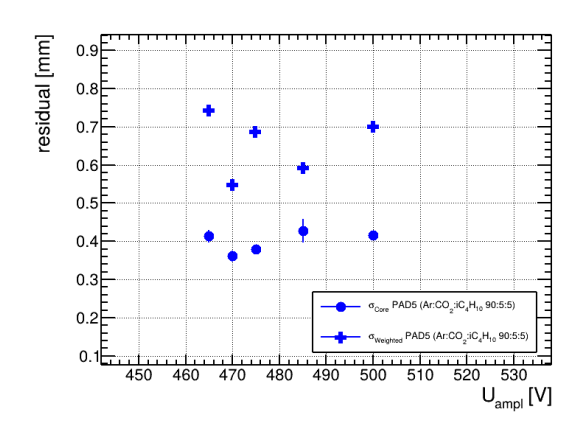
number of charge-sharing layers in PADH, which minimizes charge dispersion and preserves spatial information more effectively than the five-layer PAD5 configuration.

Figure 6.15 shows the spatial resolution measurements for both detectors. For PADH, resolution improves with increasing anode voltage as expected, with the Ar:CO₂:iC₄H₁₀ mixture showing better results than the Ar:CO₂ mixture due to higher achievable cluster charges. The relationship between resolution and cluster charge demonstrates the fundamental trade-off between signal amplitude and position accuracy. PAD5 measurements show worse resolution distributions compared to PADH. Spatial resolution for PADH at 505 V show an abnormal behavior. This is due to the low statistics of the measurement, which is evident from the very high weighted resolution value.

Detection efficiency (subsection 4.6.1) was calculated with the number of entries within a residual window of ± 3 mm. The measurements demonstrate the operational benefits of both detector designs. The PADH detector achieved efficiencies exceeding 80% with the Ar:CO₂ the isobutane-containing mixture. PAD5 measurements with the optimized gas mixture showed comparable efficiency performance, reaching detection rates above 80%. The anomaly at 505 V for PADH, as seen from resolutions, is attributed to the low statistics.

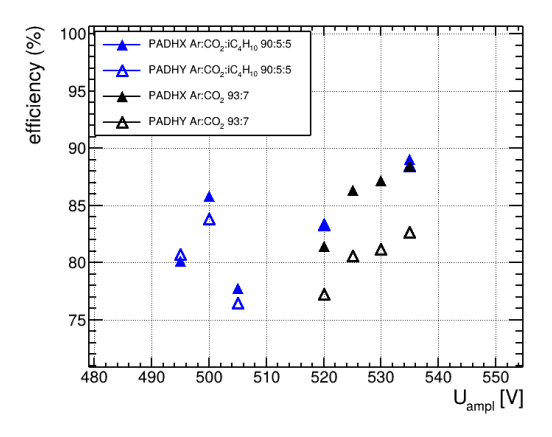
However, statistical limitations from the low cosmic muon rate of 0.07 Hz and strict angular selection criteria prevent detailed characterization of efficiency plateaus or identification of optimal operating points for both detector configurations. The week-long measurement periods required for each voltage setting limits cosmic muon characterization compared to controlled source measurements. The next chapter discuss a detailed study of the detectors under 120 GeV monoenergetic muons.

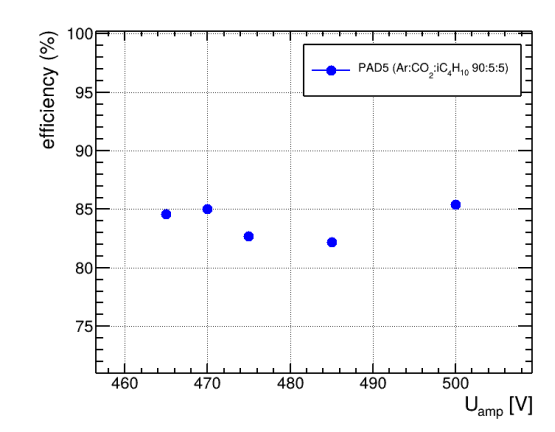




- (a) PADH spatial resolution vs anode voltage
- (b) PAD5 spatial resolution vs anode voltage

Figure 6.15: Spatial resolution comparison between PADH and PAD5 detectors with cosmic muons. (a) PADH detector showing resolution for both gas mixtures, with superior performance achieved using the isobutane-containing mixture. (b) PAD5 detector measurements using $Ar:CO_2:iC_4H_{10}$ (90:5:5 vol.%), showing broader resolution distributions due to the five-layer charge-sharing architecture.





- (a) PADH detection efficiency vs anode voltage
- (b) PAD5 detection efficiency vs anode voltage

Figure 6.16: Detection efficiency as a function of anode voltage for cosmic muon measurements using a ± 3 mm residual window. (a) PADH detector performance with Ar:CO₂ and isobutane-containing gas mixtures, showing efficiencies exceeding 80% (b) PAD5 detector efficiency with optimized gas mixture, achieving detection rates above 80%. Statistical limitations from the low cosmic muon rate (0.05 Hz) for perpendicular incidence and measurement duration constraints are evident in both datasets.

Chapter 7

Characterization with 120 GeV Muons at the CERN SPS H4 beam line

Following the characterization of the detectors with the ⁵⁵Fe source and cosmic muons, the detector is tested under 120 GeV muons and pions. While cosmic muons limit the systematic studies of the detector due to their broad energy spectrum, varying angle of incidence, and low rate, the controlled muon beams provide a precisely defined particle flux, energy, and incident angle. At 120 GeV, muons can be treated as minimum ionizing particles (see section 2.1), creating uniform track signatures for precise measurements of spatial resolution, detection efficiency, and charge-sharing performance.

The detector was characterized by varying the amplification voltages, and the results for spatial resolution and efficiency performance for perpendicular and inclined tracks are presented in this chapter.

7.1 Experimental Setup

The experiment was carried out with a high-intensity muon beam produced through the decay of charged pions and kaons created when the primary proton beam from the CERN Super Proton Synchrotron (SPS) interacts with a production target at the H4 beamline. This high-energy beam allows for particle tracking with the test detectors and four reference trackers with almost negligible effects from multiple scattering.

The hodoscope had four 2D resistive DLC Micromegas detectors of dimensions 10 cm \times 10 cm, PAD5 detector and PADH detector also of dimensions 10 cm \times 10 cm (only the setup relevant to this thesis is discussed here) and two scintillators. The detectors were flushed with Ar:CO₂:iC₄H₁₀ in 93:5:2 vol.% (see Figure 7.1).

All the detectors were read out using the APV25 hybrid boards (see section 4.1) using 2 FEC cards. The DAQ PC acquired the output signal from the FEC through ethernet cables. Ethernet cables of equal length were carefully chosen to synchronize the data

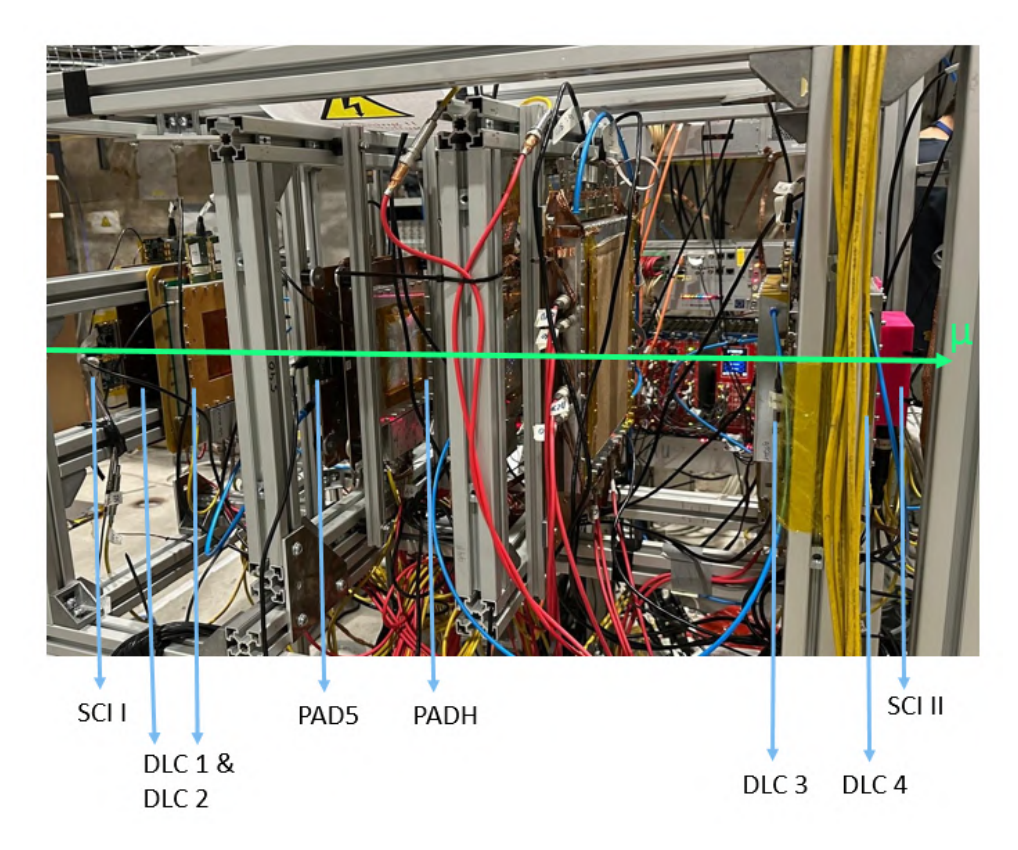


Figure 7.1: Experimental setup at the CERN SPS H4 beamline showing the detector telescope configuration. The setup consists of four 2D resistive DLC Micromegas reference detectors $(10\times10~{\rm cm^2})$, the PAD test detectors (PADH and PAD5, $10\times10~{\rm cm^2}$), and two scintillators $(9\times9~{\rm cm^2})$ for triggering. The 120 GeV muon beam traverses the detector stack, with reference detectors maintained perpendicular to the beam axis, while test detectors can be rotated around one axis for angular studies. All detectors are operated with Ar:CO₂:iC₄H₁₀ in 93:5:2 vol.% gas mixture. The other detectors visible are not relevant to the scope of this thesis.

arriving from the FEC cards. The scintillators were used to trigger on the signal. This scintillator signal is converted to a NIM signal by a discriminator following the discussion from section 4.1. A coincidence of signals from both the scintillators was required (see section 4.1), which was used for further trigger logic (See Figure 7.2). 200000 events were recorded for each measurement. The scintillators had dimensions $9 \text{ cm} \times 9 \text{ cm}$. Since this is smaller than the active area of the detectors, a position bias is introduced in the events registered in the detectors.

The position reconstruction in the reference detectors employs the centroid method (section 4.3). The reference track was reconstructed using the χ^2 minimization technique (subsection 4.4.1). Figure 7.3 shows the track error calculated using subsection 4.4.1. The estimated track error was $\approx 27 \,\mu m$ for PAD5 and PADH. While the test detector can be

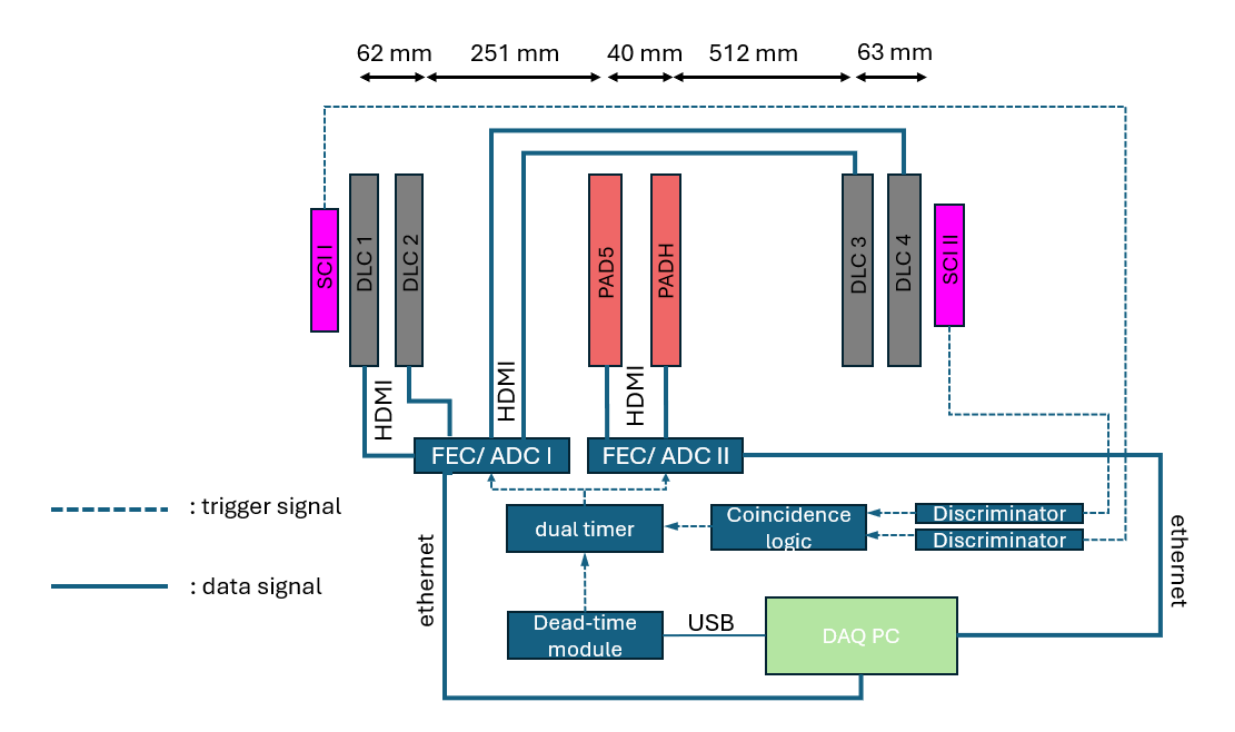


Figure 7.2: Trigger logic schematic for the H4 beamline measurements. Signals from the scintillators are converted to NIM signals via discriminators and fed into a coincidence unit. The coincidence output provides the external trigger for the SRS readout system, ensuring that only events with particles traversing both scintillators are recorded. The smaller scintillator area $(9\times9~\text{cm}^2)$ compared to the detector active area $(10\times10~\text{cm}^2)$ introduces a geometrical bias toward central region events.

rotated to various incident angles to study the charge-sharing performance as a function of track inclination, the reference detectors are deliberately maintained in their perpendicular orientation relative to the beam axis.

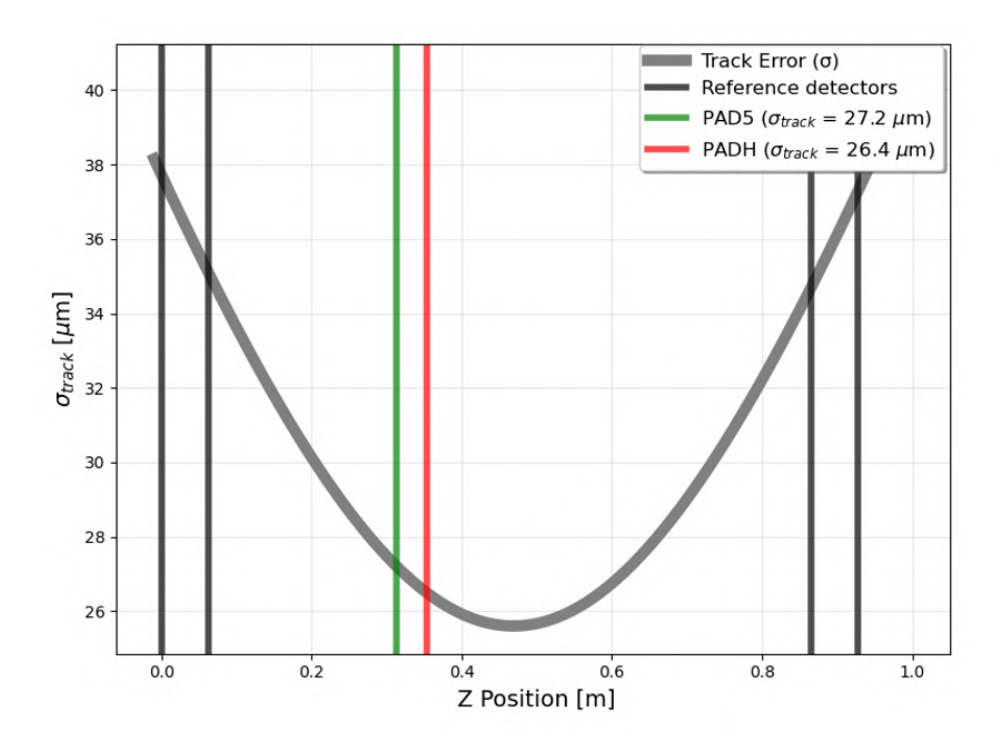


Figure 7.3: Track error plotted against Z position (along the beam) for the measurement at CERN SPS with 120 GeV muons. Track error of $\approx 27 \, \mu \text{m}$ was observed for both PAD5 and PADH detectors.

7.2 Perpendicularly Incident Particles

In this section, perpendicularly incident muons will be looked at for PADH and PAD5. Muons from the H4 beamline provide almost exactly perpendicular, mono-energetic incident particles. This allows for simple particle reconstruction with no unknown parameters. This provides a method to exactly characterize the detectors with minimal effects like multiple scattering, non-homogeneous ionization, etc. The detector is characterized, and the performance of the detector in terms of the spatial resolution and the efficiency of the detector is discussed.

7.2.1 PADH

The 3-layer PADH is examined using clustering methods analogous to strip detectors because of the strip-like readout structure. The clustering has been done with an allowed minimum cluster size of one strip. This can be attributed to the big pixel pitch of 1.2 mm in the PADH detector. Since a spread of 0.4 - 0.7 mm from an avalanche of a single muon is expected (Rinnagel 2023), this is reasonable. But such single pixel events are relatively small < 4%. The 2D beam profile of the muon beam is shown in Figure 7.4a and the pion

beam is shown in Figure 7.4b. The muon beam has a big waist in both X and Y directions and has a broad spatial spread. The pion beam, on the other hand, is very narrow with a beam width of approximately 3 cm. This matches with the expected beam profile¹. The study has been primarily carried out with the muon beam.

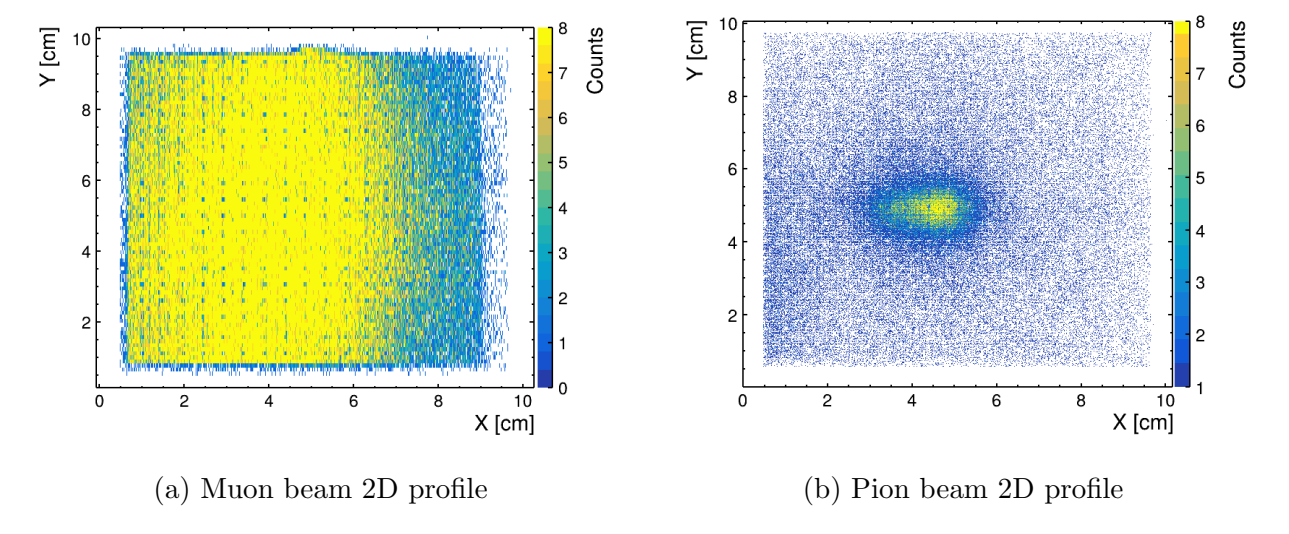


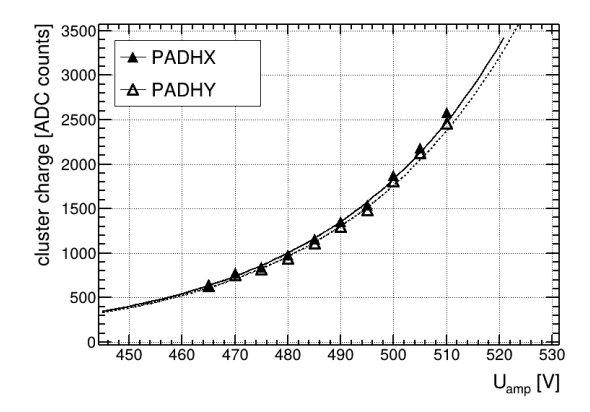
Figure 7.4: 2D beam profiles showing the spatial distribution of muon and pion beams. The muon beam (left) exhibits a broad spatial spread with a large waist in both X and Y directions, effectively covering the entire active area of the PADH detector. In contrast, the pion beam (right) is highly collimated with a narrow beam width of approximately 3 cm, resulting in a much narrower distribution on the detector surface compared to the muon beam. The hit map registers events only in an area of 9×9 cm² due to the size of the scintillators. Pillars are visible in both beam profiles as dark spots.

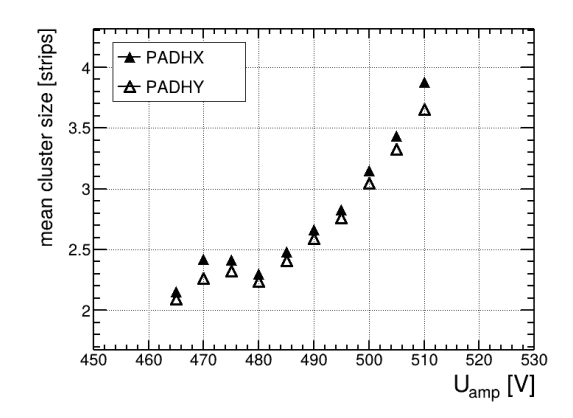
Pulse Height Analysis

A cluster is formed by grouping multiple adjacent strips together, where the sum of charges from all constituent pixels provides the total charge deposited by the muon. This clustering approach (See section 4.3) combines the individual pixel responses to reconstruct the complete charge signature of the muon. The resulting cluster charge distribution increases with an increase in the amplification voltage, exhibiting the characteristic double exponential behavior, consistent with the gas gain mechanism described by Equation 2.14. This behavior can be clearly observed in Figure 7.5a.

The cluster size represents the spatial extent of a particle hit across the detector strips. It is the span of strip numbers occupied by a cluster, measured from the first to the last strip in the cluster group. The increase in cluster size with the corresponding increase in the anode voltage is evident from Figure 7.5b. Higher anode voltages lead to broader

¹Internal communication





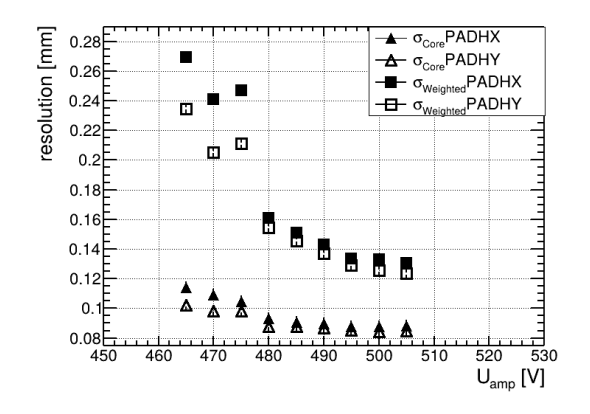
- (a) Cluster charge as a function of anode voltage in both X and Y directions
- (b) Cluster size as a function of anode voltage

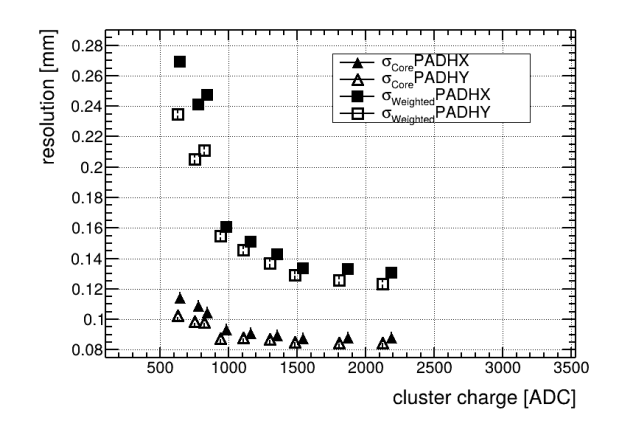
Figure 7.5: Cluster characteristics as a function of anode voltage for perpendicularly incident 120 GeV muons in the PADH detector. (a) Shows the double exponential increase in cluster charge with higher anode voltage due to avalanche amplification. (b) Demonstrates the corresponding increase in cluster width.

avalanches, leading to this behavior. Measurements between 465 V and 495 V were taken at a different time. This might lead to the kink that is observed in this range in Figure 7.5b. Different pressure and/or moisture could influence the gas gain. Owing to the segmentation of the pixels on the PADH detector, the total charge received on the whole pixel is split into two. So the sum of cluster charge along the X and Y directions gives the complete information about the charge deposited by a muon.

Spatial Resolution

The spatial resolution has been determined by interpolating the particle tracks built by the reference detectors (see section 4.5). The spatial resolution determined by the centroid method as a function of the anode voltage and cluster charge is shown in Figure 7.6. As seen in Figure 7.6a, spatial resolution improves with an increase in anode voltage since the hit position becomes more defined as the charge on a single pixel increases (Bortfeldt 2015). The improvement in spatial resolution with charge can be seen in Figure 7.6b. Slightly better resolutions along the Y direction can be observed in Figure 7.6. This is within the reconstruction error. Spatial core resolutions (subsection 4.5.1) of up to 85 μ m and up to 130 μ m weighted resolution can be achieved at anode voltages ~ 500 V. Beyond this point, the resolution plateaus.



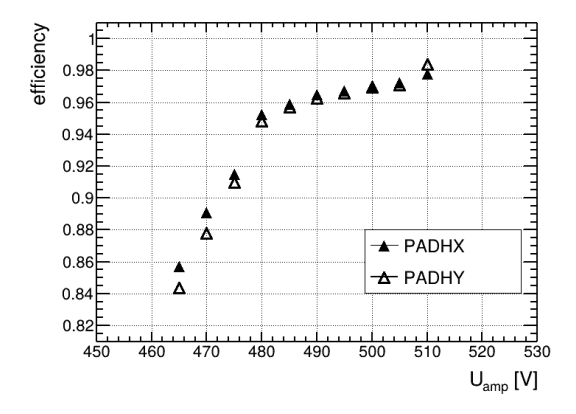


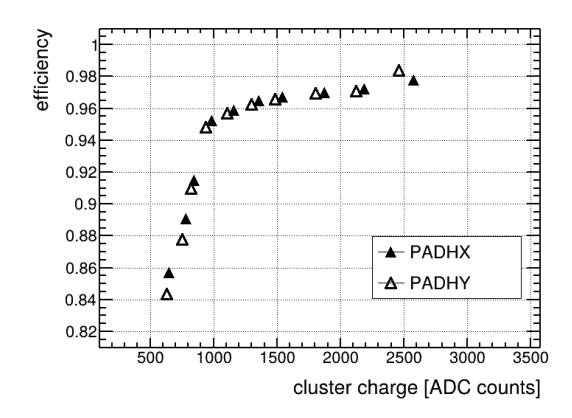
- (a) Spatial resolution as a function of anode voltage
- (b) Spatial resolution as a function of cluster charge

Figure 7.6: Core and weighted spatial resolutions of the 3-layer PADH detector for perpendicularly incident 120 GeV muons. Core resolutions of $\sigma_{\rm core} < 85~\mu m$ are achieved in both layers. The weighted residual also follows a similar pattern. (a) Resolution as a function of anode voltage, showing improvement with increasing voltage. (b) Resolution as a function of cluster charge, demonstrating the correlation between charge collection and position reconstruction accuracy. The resolution is determined using the charge centroid method with reference tracks extrapolated from the tracking hodoscope.

Efficiency

The detection efficiency has been evaluated by comparing the number of reconstructed clusters within a residual window of \pm 3mm, to the total number of reference tracks passing through the detector's active area. The efficiency, determined using the method described in Equation 4.16, as a function of anode voltage and cluster charge is shown in Figure 7.7. The efficiency sharply increases with anode voltage, reaching a plateau at approximately 96% at voltages above 490 V (seeFigure 7.7a). At lower voltages, the efficiency drops due to insufficient charge amplification. The efficiency as a function of cluster charge shows a sharp transition from low to high efficiency around 1000 ADC counts, corresponding to the effective threshold for reliable cluster reconstruction for the detector (Figure 7.7b). Even for high amplification voltages, 100% efficiencies are not achievable due to the presence of supporting pillars, which create dead/passive regions in the detector. Events in these passive regions cannot be reconstructed, leading to a loss in efficiency.





- (a) Detection efficiency as a function of anode voltage
- (b) Detection efficiency as a function of cluster charge

Figure 7.7: Detection efficiency of the 3-layer PADH detector for perpendicularly incident 120 GeV muons. (a) Efficiency as a function of anode voltage, showing the characteristic plateau behavior above 500V where the gas gain provides sufficient charge for reliable detection. (b) Efficiency as a function of cluster charge shows improving efficiencies with higher charges.

7.2.2 PAD5

The 5-layer PAD5 employs a purely pixel readout configuration, where each pixel is individually read out by an APV channel. Clustering is performed using the Depth-First Search (DFS) algorithm section 4.3, which groups all the connected pixels that receive charge to reconstruct particle trajectories. The minimum allowed cluster size is set to one pixel to accommodate the large 1 cm pixel dimensions. Since a spread of 0.4 - 0.7 mm from an avalanche of a single muon is expected (Rinnagel 2023), this is reasonable. But such single pixel events are rare < 1%, since charge sharing always ensures that the charge spread increases as it couples to bigger layers subsection 5.3.1.

The charge-sharing architecture demonstrates its effectiveness in Figure 7.8, where position information can be reconstructed to a precision of a few hundred micrometers despite the coarse 1 cm pixel pitch. A surface map of the pixels can be seen. This sub-pixel resolution capability is enabled by the unique charge distribution patterns created by the layered architecture, as discussed in subsection 5.3.5. In Figure 7.8b, it can be observed that more events are reconstructed at the center of the pixels. This behavior is exactly the same seen in Figure 6.10b. According to simulations for a three-layer charge share detector by (Menzer 2025), this effect arises due to the inherent electric field configuration within the coupled pixels. This effect was seen to increase with an increase in the number of layers, making it more prominent in the five-layer PAD5 detector.

Measurements with 120 GeV muons were performed using two gas mixtures: Ar:CO₂:iC₄H₁₀ in 93:5:2 vol.% and Ar:CO₂ in 93:7 vol.%. The latter measurements were conducted dur-

ing the 2023 H4 beamtime and provide a comparative baseline for evaluating the detector performance under different operational conditions.

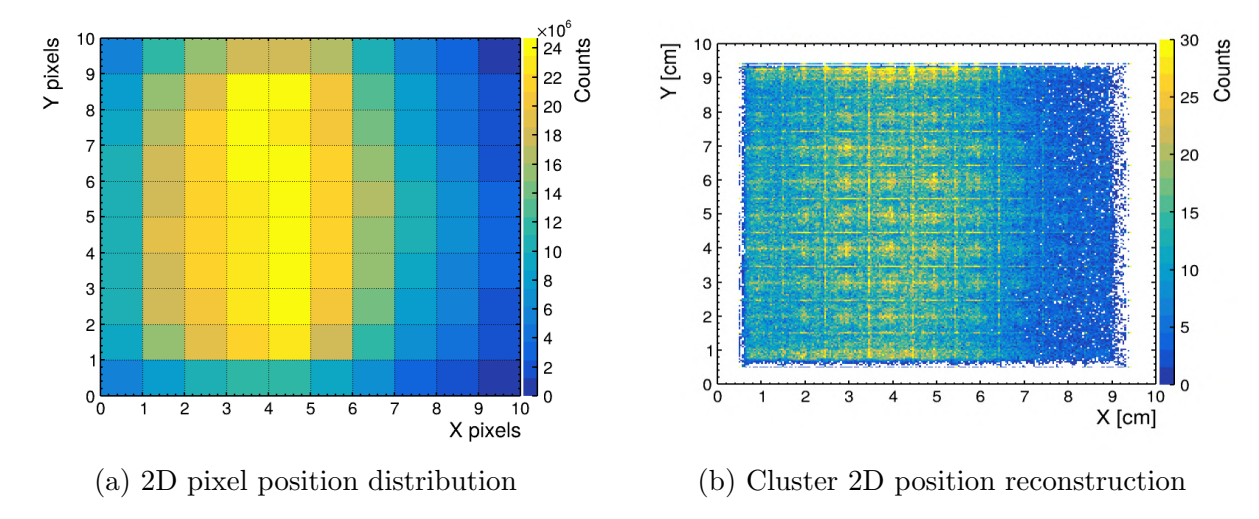


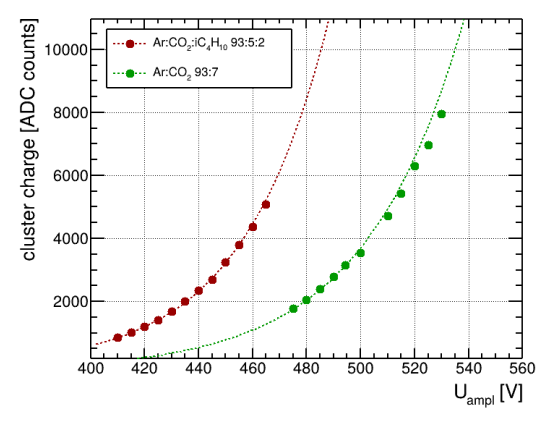
Figure 7.8: PAD5 detector position reconstruction capabilities. The left figure shows the 2D pixel position distribution from the coarse 1 cm pixel readout, while the right figure demonstrates the reconstructed cluster 2D positions. Despite the large pixel pitch of 1 cm, the position information can be reconstructed to a precision of a few hundred micrometers through charge sharing between adjacent pixels. The clustering is performed using the Depth-First Search (DFS) algorithm with a minimum cluster size of one pixel. Measurements shown are from muon beam data using $Ar:CO_2:iC_4H_{10}$ in 93:5:2 vol.% gas mixture. More events are reconstructed at the center of the pixels. The hit map registers events only in an area of 9×9 cm² due to the size of scintillators.

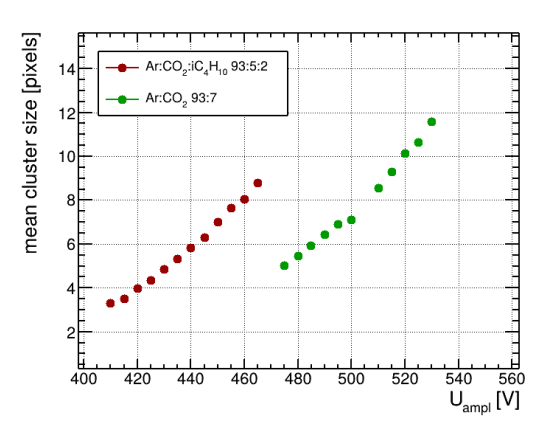
Pulse Height Analysis

Cluster size for PAD5 shows the number of pixels in a cluster. This gives a measure of the charge spread. The cluster size and cluster charge evolution with anode voltage, presented in Figure 7.9a and Figure 7.9b, show the increased cluster charges and expanded charge cloud, leading to enhanced lateral charge spread across neighboring pixels, due to an increase in the amplification voltage. Five layers of capacitively coupled pixels, lead to a broader spread of the charges across pixels on the readout layer (layer 5), which can be observed in Figure 7.9b. The double exponential behavior of gas amplification can be clearly seen in the cluster charge plot Figure 7.9a. The saturation of the charges because of the APVs can be noticed at voltages above 460 V for Ar:CO₂:iC₄H₁₀ in 93:5:2 vol.%. For the Ar:CO₂ in 93:7 vol.% mixture, this saturation is observed above 500 V. This values correspond to similar values of cluster charge as a result of different gas gains for the different gases.

Following the discussion in section 3.3, each bigger layer is shared between 9 pixels in the smaller layer (see section 5.1). In the five layer configuration, one pixel on the fifth layer is

shared between 9⁴ smaller pixels on layer 1. This is different from the 3 layer PADH where one pixel on the third layer is shared between 9² smaller pixels on layer 1. Furthermore, there is no segmentation of the pixel in PAD5. This might lead to a potential loss, due to higher number of layers, in the charge information since before collecting the full charge, the electronics go into saturation.





- (a) Cluster charge as a function of anode voltage
- (b) Cluster size as a function of anode voltage

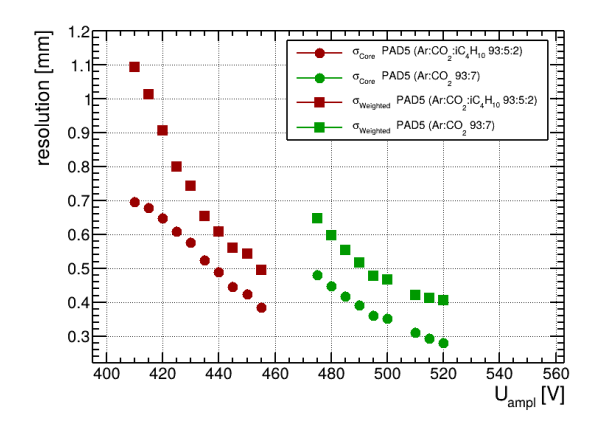
Figure 7.9: Cluster characteristics as a function of anode voltage for perpendicularly incident 120 GeV muons in the 5-layer PAD5 detector. (a) Shows the increasing cluster charges following the double exponential behaviour from gas gain. Saturation effects can be observed as deviation from the fit. (b) Demonstrates the cluster size, which is the number of pixels in a cluster, evolving with increasing anode voltages. The high number of pixels per cluster indicates an unprecedented spreading of the charge.

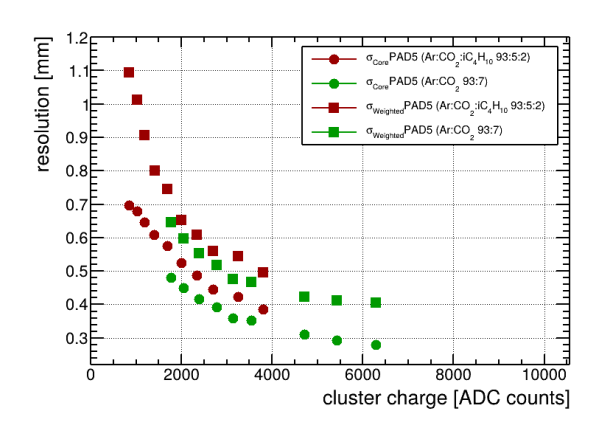
Spatial Resolution

The spatial resolution of PAD5 is determined through charge-centroid position reconstruction (See section 4.3). Figure 7.10a shows the resolution as a function of anode voltage, achieving values approaching 400 µm at optimal operating conditions for Ar:CO₂:iC₄H₁₀ in 93:5:2 vol.% mixture. For Ar:CO₂ in 93:7 vol.% gas mixture, resolutions better than 300 µm are achieved at higher cluster charges. The APVs saturate around 3500 ADC counts. Typically, electronic saturation would be expected to degrade spatial resolution. However, a worsening of the resolution is not observed. On the contrary the resolutions get better beyond the saturation point of the electronics. It can be argued that, due to charge sharing, even though the central pixels are saturated, the surrounding pixels receive more charge on them, adding them to the cluster. So when the position is determined through the centroid method (section 4.3), the surrounding pixels lead to an improved position reconstruction. But this requires further in depth study.

The spatial resolution of PAD5 plateaus around 290 μ m, which is three times coarser than the spatial resolutions obtained for PADH ($\approx 85\mu$ m). This coarse resolution can be

attributed to two major reasons. The pixels in layer 1 of PAD5 is 0.625 mm compared to the pixel size of 0.3 mm in PADH. Furthermore, PAD5 has a bigger 1 cm readout pixel compared to 1.2 mm readout pixel size in PADH. So, in the best-case scenario, resolutions are expected to be at least twice as bad for PAD5 compared to PADH, by merely comparing the pixel sizes in the collection layer. In addition, looking at Figure 7.12 and Figure 7.13, we see a periodic substructure when the residual is plotted against position, which might also affect the achievable resolution. This will be discussed in more detail in section 7.3.





- (a) Spatial resolution vs anode voltage
- (b) Spatial resolution vs cluster charge

Figure 7.10: Spatial resolution of the 5-layer PAD5 detector for perpendicularly incident 120 GeV muons. (a) Resolution as a function of anode voltage for both gas mixtures, showing improved performance with $Ar:CO_2$ in 93:7 vol.% achieving values under 300 μ m compared to approximately 400 μ m for $Ar:CO_2:iC_4H_{10}$ in 93:5:2 vol.%. (b) Resolution as a function of cluster charge, demonstrating continued improvement even beyond APV saturation.

Efficiency

The detection efficiency has been evaluated by comparing the number of reconstructed clusters within a residual window of \pm 3 mm, to the total number of reference tracks passing through the detector's active area, similar to the PADH. The efficiency determined using the method described in Equation 4.16 as a function of anode voltage and cluster charge is shown in Figure 7.11. The efficiency sharply increases with anode voltage, reaching above 94% at voltages above 450 V. At lower voltages, the efficiency drops due to insufficient charge amplification.

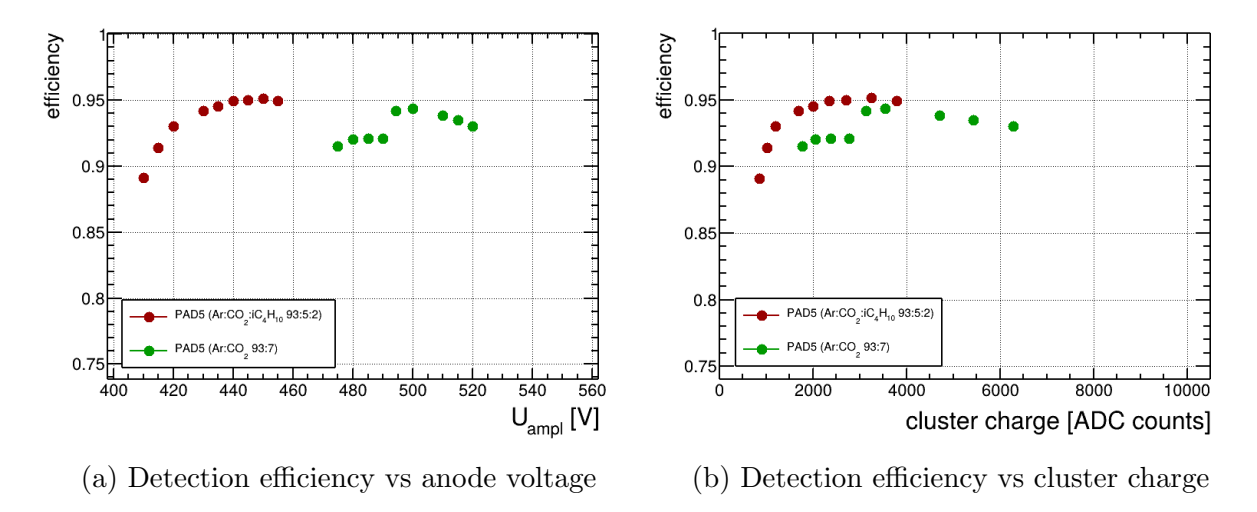


Figure 7.11: Detection efficiency of the 5-layer PAD5 detector for perpendicularly incident 120 GeV muons. (a) Efficiency as a function of anode voltage, reaching plateau values above 94% at voltages exceeding 450V for both gas mixtures. (b) Efficiency as a function of cluster charge, showing the characteristic threshold behavior around the minimum charge required for reliable cluster reconstruction. The efficiency is determined by matching reconstructed clusters to reference tracks within a 3 mm residual window.

7.3 Periodic Substructures

The residual distributions as a function of position reveal a distinctive periodic substructure that correlates directly with the detector's pixel pitch, as shown in Figure 7.12 and Figure 7.13. This periodic substructure introduces a systematic position-dependent bias that can affect the inherent resolution of the detector. Looking at the figures, two types of periodicity can be noticed. Big jumps in the residual distribution that repeats after 1.2 mm, which is the pixel pitch in the three layer PADH, while the same pattern is noticeable at 10 mm interval for PAD5, which corresponds to its pixel pitch. At the same time, a small internal pattern can also be observed which increases linearly within the pixel pitch of the readout layer. Looking at Figure 7.12b, we can see huge oscillations with an amplitude of 0.6 mm. But within a period, linearly increasing internal structures are observed with a maximum amplitude of 0.1 mm. According to the simulations studies on three layer capacitive-sharing pixel Micromegas detector done by (Menzer 2025), these structures have been simulated. They arise as a result of the electric field configuration on smaller pixel layers due to the multiple layers (see chapter 8). A similar pattern can be observed with PAD5 (see Figure 7.13b), where the amplitude of the big oscillation at intervals of 10 mm is in the range of 4 mm, while the small internal structure oscillates between 2 mm. Any further details cannot be resolved from visual inspection of the plots.

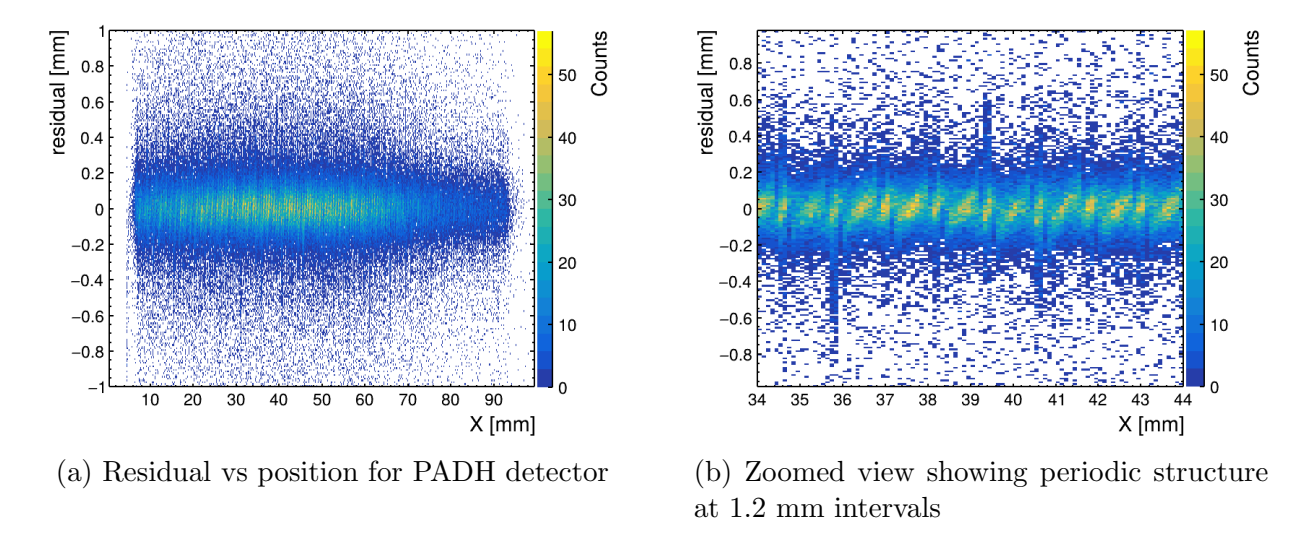


Figure 7.12: Periodic substructure in position residuals for the 3-layer PADH detector with 1.2 mm pixel pitch. (a) Full range residual distribution showing systematic modulation across the detector. (b) Zoomed view revealing the periodic pattern with wavelength exactly matching the pixel pitch. The substructure within the 1.2 mm is also visible.

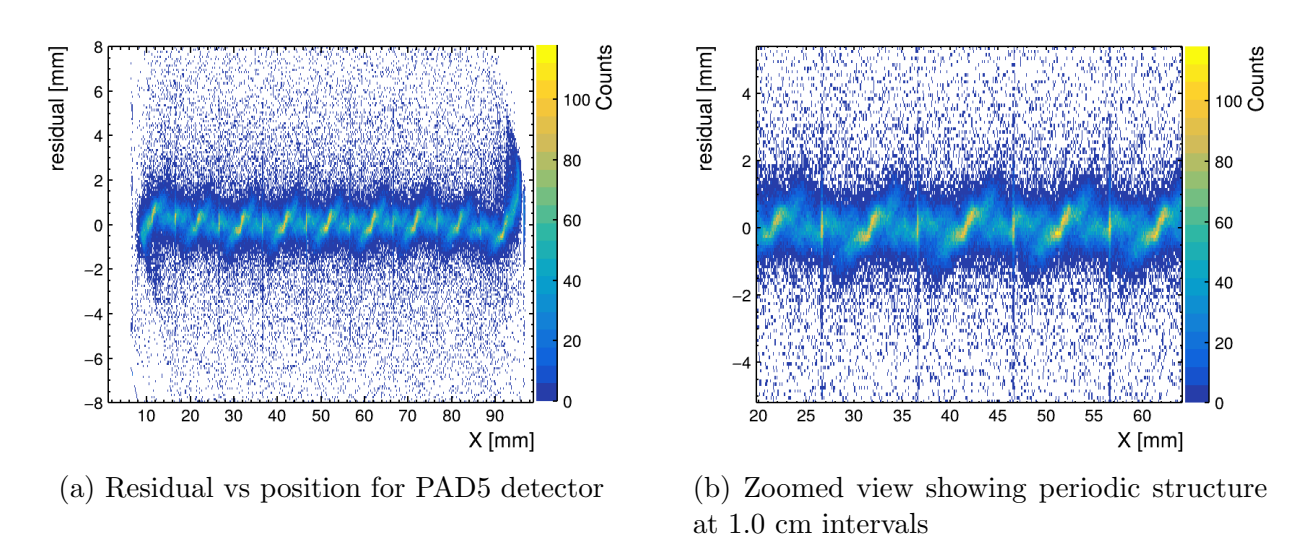


Figure 7.13: Periodic substructure in position residuals for the 5-layer PAD5 detector with 10 mm pixel pitch. (a) Full range residual distribution demonstrating the systematic position-dependent bias across multiple pixels. (b) Zoomed view highlighting the periodic pattern with 10 mm wavelength corresponding to the pixel dimensions. The substructure within the 10 mm pixel pitch is also visible. The multi-layer architecture of PAD5 shows similar effects but with different wavelengths.

Correcting for these effects can further improve the resolution of the detector. The huge

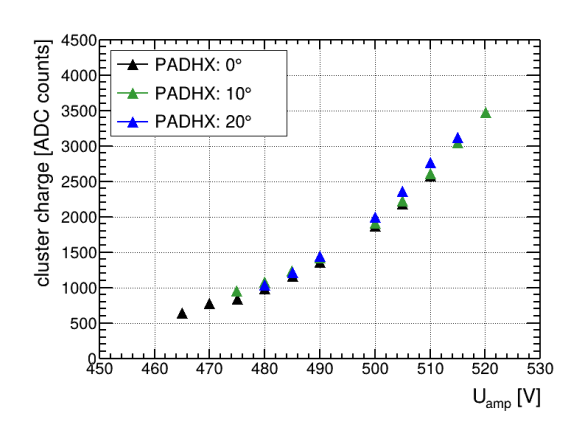
amplitudes of oscillation for PAD5 might be a contributing factor for the worse internal resolution of the detector compared to PADH. In Figure 7.13a the edge effects of the pixels can be identified. At 10 mm and 90 mm, the last pixels collect the charge since the pixel pitch is 10 mm. This cannot be seen on PADH since beyond 90 mm, there are more pixels since the pitch is 1.2 mm.

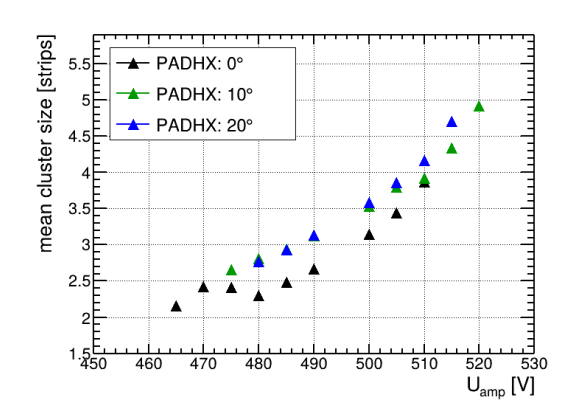
7.4 Inclined incident particles

In addition to perpendicular incidence muons, PADH detector was characterized also with inclined incidence muons. The test detectors were mounted in the tracking hodoscope such that they could be rotated. Only the test detectors were rotated along the Y axis. As a result, the rotation can only be resolved in the X direction and not in the Y direction. The trackers were maintained perpendicular to the muon beam. Measurements were taken with a rotation of $\Theta = 10 \pm 1^{\circ}$ and $\Theta = 20 \pm 1^{\circ}$.

7.4.1 Pulse Height Analysis

Following the discussion from section 4.6, inclined particles traverse a greater distance within the drift gap. When particles enter the detector at an angle, their path length through the drift gap increases, leading to enhanced ionization along the extended trajectory, and consequently, larger apparent cluster sizes are observed in the readout plane. This leads to an increase in the cluster charge and cluster size.





(a) Cluster charge as a function of anode voltage for different incident angles

(b) Cluster size as a function of anode voltage for different incident angles

Figure 7.14: Comparison of cluster characteristics in X direction for perpendicular (0°) and inclined $(10^{\circ}, 20^{\circ})$ particle incidence in the 3-layer PADH detector. (a) Increasing cluster charge, with an increase in anode voltage. Effects of incline cannot be seen. (b) Cluster size increases with incident angle due to the extended particle track and the resultant charge coupling to the upper layers.

Cluster charge vs anode voltage is plotted in Figure 7.14a. But no evident trend can be seen between inclination and cluster charge. The increase is well within the systematic uncertainties since the measurements were taken on different days, leading to different pressure and humidity conditions. In Figure 7.14b the cluster size exhibit systematic increase compared to perpendicular incidence at the same anode voltages due to more charge spreading as more pixels in layer 1 see the charge.

7.4.2 Spatial Resolution

Following the discussion in section 4.6, the spatial resolution for inclined particle has been determined using the time corrected centroid method and compared to the charge-centroid position reconstruction (See section 4.3). The time-corrected position reconstruction method leads to improved spatial resolution compared to the simple centroid method for inclined tracks.

Figure 7.15 presents a comparison between the standard centroid method and the time-corrected reconstruction for different incident angles. For perpendicular tracks (0°) , both methods yield identical results as expected, since no timing correction is applied. However, significant improvements are observed at higher inclinations, where the time-corrected method improves the spatial resolution.

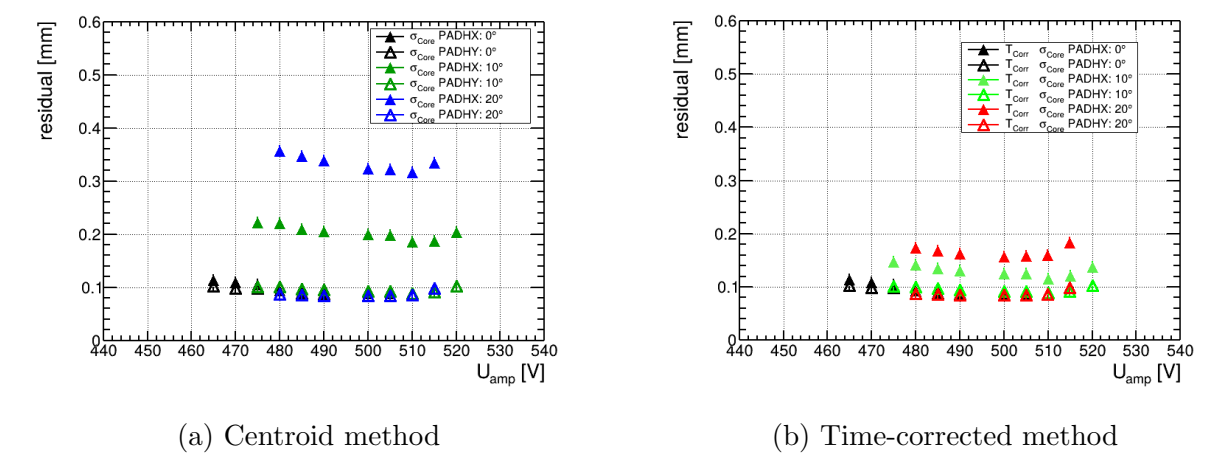


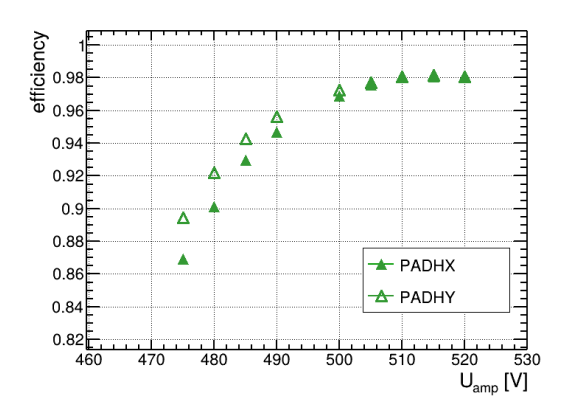
Figure 7.15: Comparison of spatial resolution for different track inclination angles using (a) the standard charge centroid method and (b) the time-corrected reconstruction method. At 0° , both methods yield equivalent resolution of approximately 85 µm. For inclined tracks, the centroid method shows degraded resolution reaching 300 µm at 20° , while the time-corrected method maintains resolution below 180 µm by compensating for drift-time variations. The measurements demonstrate the effectiveness of timing corrections in preserving spatial resolution for inclined particle tracks. Y direction sees similar resolutions as to that of perpendicularly incident particles.

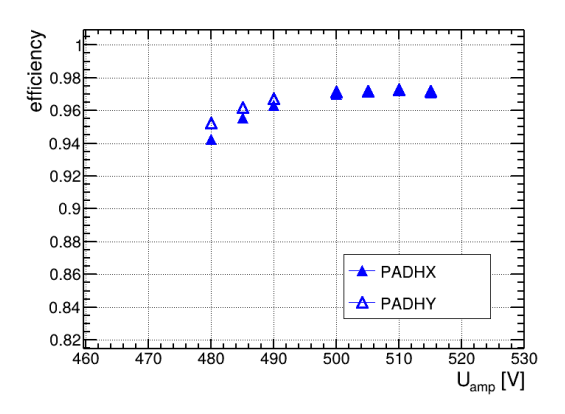
The resolution degradation observed with the centroid method at higher angles directly

results from the uncorrected position bias. At 20° inclination, the centroid method resolution deteriorates to over 300 µm. In contrast, using the time-corrected method, resolutions below 180 µm even at 20° can be achieved. Similarly, for 10° inclination, a clear improvement in the resolution from 200 µm to under 120 µm is visible using the time-corrected method. The difference in resolutions after applying time correction is only visible along X since the detector is rotated around the Y axis. The orthogonal Y direction still see perpendicular incidence of particles.

7.4.3 Efficiency

The efficiency for inclined particle tracks follow a similar trend to that of perpendicularly incident muons. The detector achieves efficiencies around 98% for particles at 10° inclination. 100% efficiencies cannot be attained due to the insulating pillars, leading to non reconstructed particles in this region. Efficiencies above 96% is achieved for particles at 20° inclination. The slight reduction in the efficiency is due to being rotated out of the beam at this angle.





- (a) Detection efficiency at 10° inclination
- (b) Detection efficiency at 20° inclination

Figure 7.16: Detection efficiency of the 3-layer PADH detector as a function of anode voltage for inclined particle tracks. (a) Efficiency at 10° inclination showing the efficiency plateau above 510 V, maintaining values above 95%. (b) Efficiency at 20° inclination demonstrating similar behavior.

Chapter 8

Summary and Outlook

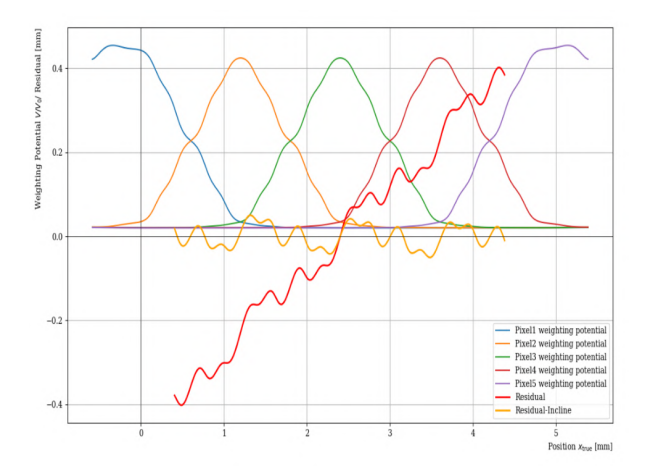
In this thesis, the performance of a three-layer hybrid PADH detector and a five-layer PAD5 capacitively coupled pixel detectors has been investigated. By implementing a multi-layered charge-sharing architecture, capacitively coupled pixel detectors decouple spatial resolution from readout channel count through controlled capacitive coupling between pixelated layers of progressively increasing size.

The unique position reconstruction through charge coupling was successfully verified by testing two prototype detectors. Both detectors demonstrated excellent performance with ⁵⁵Fe source. PADH achieved energy resolutions below 12% while PAD5 achieved energy resolutions below 10%. Tests with 120 GeV muons were performed at CERN SPS. PADH detector achieved spatial resolutions up to 85 µm and detection efficiencies exceeding 96% for perpendicular tracks. Inclined particle tracks of up to 20° were tested, achieving spatial resolutions under 160 µm and detection efficiencies exceeding 96%. These results are comparable to traditional strip-based gaseous detectors, confirming that the charge-sharing mechanism does not compromise detector performance. The five-layer PAD5 detector, despite having coarse 1 cm readout pixels, achieved spatial resolutions up to 300 µm with detection efficiencies above 95%. This demonstrates that the detectors can effectively maintain good spatial resolution even with very large readout pixels, validating the concept of decoupling resolution from readout granularity.

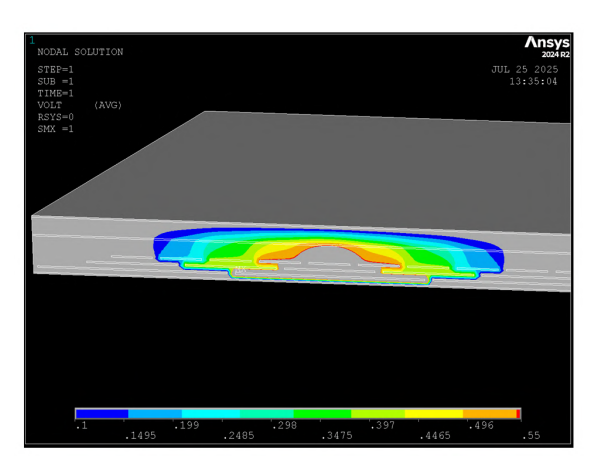
The characterization performed in this work of PADH and PAD5 detectors has revealed significant potential for further optimization and development. While both detector architectures demonstrate promising performance characteristics, several systematic effects have been identified that require future investigation and correction.

During detector characterization studies using ⁵⁵Fe X-ray sources and muon test beams, distinctive periodic substructures were observed in the residual distributions at multiple length scales. Primary periodic patterns with wavelengths corresponding precisely to the detector pixel pitch (1.2 mm for PADH and 1.0 cm for PAD5) were identified, accompanied by smaller-scale substructures observable within individual pixel regions (See Figure 6.10, Figure 7.13, Figure 7.12). These substructures potentially pose a fundamental limitation to the achievable spatial resolution. It is therefore essential to understand the origin of these substructures and develop appropriate correction strategies.

Simulation studies for Micromegas with three layers of capacitively coupled pixels with 5×5 readout pixels by (Menzer 2025) have demonstrated that these systematic position-dependent biases arise from the inherent electric field configuration within the pixel architecture. The field-induced charge collection patterns create preferential positions for spatial reconstruction that introduce systematic effects in the position reconstruction.



(a) Comparison of residual distributions and weighting potential across 5 pixels. The raw residual (red) and inclination-corrected residual (orange) demonstrate clear oscillating behavior that correlates with pixel boundaries. Plateau regions in the weighting potential create steep gradients in the residual distribution, as identical positions are reconstructed across each plateau.



(b) Weighting field distribution for pixel 3 in the normalized interval [0.1, 0.55]. The stretching effect of the electric potential due to the constant potential boundary conditions on adjacent smaller pixels is clearly visible, particularly at the DLC (Diamond-Like Carbon) layer height. The horizontal stretching of the contour (orange, yellow, green, and blue) corresponds directly to the plateau features observed at positions {2.4, 2.7, 3.0, 3.3} mm in the pixel 3 weighting potential (green curve) shown in subplot (a).

Figure 8.1: Correlation between residual behavior and weighting field structure. (a) Position residuals showing plateau-induced effects in the reconstruction. (b) Two-dimensional weighting field visualization demonstrating the physical origin of the plateau effects observed in the residual distributions. Figures adapted from (Menzer 2025)

Detailed analysis of the simulation results reveals distinct characteristics for the three prominent plateaus at 2.4 mm, 2.7 mm, and 3.0 mm positions in Figure 8.1a. The plateau at 2.4 mm exhibits the most pronounced behavior, characterized by the flattest and widest profile. This enhanced plateau formation results from the alignment of all pixel layers at this position, where the overlapping electric field contributions from multiple pixels reinforce each other, creating a particularly stable potential region (see Figure 8.1b). Similarly, the plateau at 3.0 mm demonstrates significant amplitude due to the combined influence of the middle and small pixel layers, amplifying the field effect and forming a common,

well-defined plateau structure.

In contrast, the plateau at 2.7 mm appears less pronounced and more difficult to distinguish, as it originates primarily from the contribution of only the small pixel layer without substantial reinforcement from other detector layers. This layered contribution pattern directly correlates with the corresponding oscillation amplitudes observed in the residual distributions: flatter and wider plateaus generate steeper residual gradients and more prominent oscillations, while narrower plateaus like the one at 2.7 mm produce only slight oscillatory effects. This plateau structure fundamentally reflects the underlying multi-layer detector architecture, with the most significant effects occurring at positions where multiple detector layers are spatially aligned. This insight explains why the five-layer PAD5 detector exhibits higher amplitude oscillations compared to the three-layer PADH system, as the increased number of contributing layers enhances the cumulative field effects and plateau formation. The results of the simulation correspond to actual measurements as it gives an insight into the different amplitudes of the substructures. The next step would be to scale up the simulation to study the actual detector geometry and characterize this behavior further so that it can be corrected exactly to potentially achieve better resolutions.

Bibliography

- Alexopoulos, T. et al. (June 2011). "A spark-resistant bulk-micromegas chamber for high-rate applications". In: Nuclear Instruments and Methods in Physics Research Section A: Accelerators, Spectrometers, Detectors and Associated Equipment 640.1, pp. 110–118. ISSN: 0168-9002. DOI: 10.1016/j.nima.2011.03.025. URL: https://www.sciencedirect.com/science/article/pii/S0168900211005869.
- Allison, W. W. M. and J. H. Cobb (Nov. 1980). "Relativistic charged particle identification by energy loss". English. In: *Annu. Rev. Nucl. Sci.; (United States)* 30:1. Institution: Nuclear Physics Laboratory, University of Oxford, Oxford, United Kingdom OX1 3RH. ISSN: ARNUA. DOI: 10.1146/annurev.ns.30.120180.001345. URL: https://www.osti.gov/biblio/6872361.
- Alviggi, M. et al. (Aug. 2019). "Small-pad resistive Micromegas for high rate environment: Performance of different resistive protection concepts". In: Nuclear Instruments and Methods in Physics Research Section A: Accelerators, Spectrometers, Detectors and Associated Equipment. Frontier Detectors for Frontier Physics: 14th Pisa Meeting on Advanced Detectors 936, pp. 408-411. ISSN: 0168-9002. DOI: 10.1016/j.nima. 2018.10.052. URL: https://www.sciencedirect.com/science/article/pii/S0168900218313676.
- Berger M.J., Hubbell J.H. (2010). In.
- Beringer, J. et al. (July 2012). "Review of Particle Physics". In: *Physical Review D* 86. ADS Bibcode: 2012PhRvD..86a0001B, p. 010001. ISSN: 1550-79980556-2821. DOI: 10.1103/PhysRevD.86.010001. URL: https://ui.adsabs.harvard.edu/abs/2012PhRvD..86a0001B.
- Bortfeldt, Jonathan (Apr. 2014). "Development of floating strip micromegas detectors". PhD thesis. Ludwig-Maximilians-Universität München.
- (2015). The Floating Strip Micromegas Detector: Versatile Particle Detectors for High-Rate Applications.
 en. Springer Theses. ISSN: 2190-5053, 2190-5061. Cham: Springer International Publishing. ISBN: 978-3-319-18892-8 978-3-319-18893-5.
 DOI: 10.1007/978-3-319-18893-5.
 URL: https://link.springer.com/10.1007/978-3-319-18893-5.
- Brice, Maximilien and Julien Marius Ordan (2021). New Small Wheel (NSW) descent into ATLAS' "side A" of the experimental cavern. URL: https://cds.cern.ch/record/2775525.

92 BIBLIOGRAPHY

Brunbauer, F. M. et al. (Apr. 2025). "Primary and secondary scintillation of CF4-based mixtures in low-pressure gaseous detectors". English. In: Frontiers in Detector Science and Technology 3. Publisher: Frontiers. ISSN: 2813-8031. DOI: 10.3389/fdest.2025. 1561739. URL: https://www.frontiersin.org/journals/detector-science-and-technology/articles/10.3389/fdest.2025.1561739/full.

- Carnegie, R. K. et al. (Feb. 2005). "Resolution studies of cosmic-ray tracks in a TPC with GEM readout". In: Nuclear Instruments and Methods in Physics Research Section A: Accelerators, Spectrometers, Detectors and Associated Equipment 538.1-3. arXiv:physics/0402054, pp. 372-383. ISSN: 01689002. DOI: 10.1016/j.nima.2004.08.132. URL: http://arxiv.org/abs/physics/0402054.
- Čerenkov, P. A. (Aug. 1937). "Visible Radiation Produced by Electrons Moving in a Medium with Velocities Exceeding that of Light". In: *Physical Review* 52.4. Publisher: American Physical Society, pp. 378–379. DOI: 10.1103/PhysRev.52.378. URL: https://link.aps.org/doi/10.1103/PhysRev.52.378.
- CMS Collaboration (2008). "The CMS experiment at the CERN LHC". In: Journal of Instrumentation 3.08, S08004. DOI: 10.1088/1748-0221/3/08/S08004.
- Collaboration, ATLAS (May 2024). "The ATLAS Experiment at the CERN Large Hadron Collider: A Description of the Detector Configuration for Run 3". In: *Journal of Instrumentation* 19.05. arXiv:2305.16623 [physics], P05063. ISSN: 1748-0221. DOI: 10.1088/1748-0221/19/05/P05063. URL: http://arxiv.org/abs/2305.16623.
- Fermi, Enrico (Mar. 1940). "The Ionization Loss of Energy in Gases and in Condensed Materials". In: *Physical Review* 57.6. Publisher: American Physical Society, pp. 485–493. DOI: 10.1103/PhysRev.57.485. URL: https://link.aps.org/doi/10.1103/PhysRev.57.485.
- Flierl, Bernhard (Apr. 2018). "Particle tracking with micro-pattern gaseous detectors". PhD thesis. Ludwig-Maximilians-Universität Munich. URL: http://nbn-resolving.de/urn:nbn:de:bvb:19-221980.
- Giomataris, Y. et al. (1996). "MICROMEGAS: a high-granularity position-sensitive gaseous detector for high particle-flux environments". In: Nuclear Instruments and Methods in Physics Research Section A: Accelerators, Spectrometers, Detectors and Associated Equipment 376.1, pp. 29–35. ISSN: 0168-9002. DOI: https://doi.org/10.1016/0168-9002(96)00175-1. URL: https://www.sciencedirect.com/science/article/pii/0168900296001751.
- Gnanvo, Kondo et al. (Feb. 2023). "Performance of a resistive micro-well detector with capacitive-sharing strip anode readout". In: Nuclear Instruments and Methods in Physics Research Section A: Accelerators, Spectrometers, Detectors and Associated Equipment 1047, p. 167782. ISSN: 0168-9002. DOI: 10.1016/j.nima.2022.167782. URL: https://www.sciencedirect.com/science/article/pii/S0168900222010749.
- Griffiths, David J. (June 2017). *Introduction to Electrodynamics*. en. ISBN: 9781108333511 Publisher: Cambridge University Press. DOI: 10.1017/9781108333511. URL: https://www.cambridge.org/highereducation/books/introduction-to-electrodynamics/3AB220820DBB628E5A43D52C4B011ED4.

BIBLIOGRAPHY 93

Grupen, Claus and Boris Shwartz (2008). *Particle Detectors*. 2nd ed. Cambridge Monographs on Particle Physics, Nuclear Physics and Cosmology. Cambridge: Cambridge University Press. DOI: 10.1017/CB09780511534966. URL: https://www.cambridge.org/core/books/particle-detectors/3431B735771D61076439E7B918D796AF.

- Gutierrez, R. M., E. A. Cerquera, and G. Mañana (July 2012). "MPGD for breast cancer prevention: a high resolution and low dose radiation medical imaging". In: *Journal of Instrumentation* 7. Publisher: IOP ADS Bibcode: 2012JInst...7C7007G, p. C07007. DOI: 10.1088/1748-0221/7/07/C07007. URL: https://ui.adsabs.harvard.edu/abs/2012JInst...7C7007G.
- Horvat, Sandra (2005). "Study of the Higgs Discovery Potential in the Process $pp \to H \to 4\mu$ ". PhD thesis. Zagreb Univ. URL: http://cds.cern.ch/record/858509.
- Jagfeld, Christoph (May 2023). "Research and development of a segmented GEM readout detector". de. Text.PhDThesis. Ludwig-Maximilians-Universität München. URL: https://edoc.ub.uni-muenchen.de/31894/.
- Jones, L (2001). APV25-S1: User guide version 2.2. Chilton: RAL Microelectronics Design Group. URL: http://cds.cern.ch/record/1069892.
- Kawamoto, T. et al. (June 2013). "New Small Wheel Technical Design Report". In.
- Kleinknecht, K. (1998). Detectors for Particle Radiation. Detectors for Particle Radiation. Cambridge University Press. ISBN: 978-0-521-64854-7. URL: https://books.google.de/books?id=RIO5DW7rtmMC.
- Klitzner, Felix (2019). "Development of novel two-dimensional floating strip micromegas detectors with an in-depth insight into the strip signal formation". PhD Thesis. Munich U. DOI: 10.5282/edoc.24286.
- Kumar, Eshita (2026). "Research and Development of a Capacitive-Sharing Pixel Micromegas Detector". PhD thesis. Ludwig-Maximilians-Universität München.
- Leo, William R. (1994). Techniques for Nuclear and Particle Physics Experiments: A Howto Approach. en. Berlin, Heidelberg: Springer. ISBN: 978-3-540-57280-0 978-3-642-57920-2.
 DOI: 10.1007/978-3-642-57920-2. URL: https://link.springer.com/10.1007/978-3-642-57920-2.
- Manjarres, J. et al. (Mar. 2012). "Performances of Anode-resistive Micromegas for HL-LHC". In: *Journal of Instrumentation* 7.03. arXiv:1202.1074 [physics], pp. C03040–C03040. ISSN: 1748-0221. DOI: 10.1088/1748-0221/7/03/C03040. URL: http://arxiv.org/abs/1202.1074.
- Martoiu, S. et al. (Mar. 2013). "Development of the scalable readout system for micropattern gas detectors and other applications". en. In: *Journal of Instrumentation* 8.03, p. C03015. ISSN: 1748-0221. DOI: 10.1088/1748-0221/8/03/C03015. URL: https://dx.doi.org/10.1088/1748-0221/8/03/C03015.
- Melissinos, Adrian C. (1966). Experiments in modern physics. eng. Open Library ID: OL5953060M. New York: Academic Press.
- Menzer, Max (2025). Simulation Studies of a Capacitive-Sharing Pixel Micromegas Detector. URL: https://www.etp.physik.uni-muenchen.de/publications/bachelor/download_auth_etp/bac25_mmenzer.pdf.

94 BIBLIOGRAPHY

Navas, S. et al. (Aug. 2024). "Review of Particle Physics". en. In: *Physical Review D* 110.3, p. 030001. ISSN: 2470-0010, 2470-0029. DOI: 10.1103/PhysRevD.110.030001. URL: https://link.aps.org/doi/10.1103/PhysRevD.110.030001.

- Particle Data Group et al. (Aug. 2022). "Review of Particle Physics". In: *Progress of Theoretical and Experimental Physics* 2022.8, p. 083C01. ISSN: 2050-3911. DOI: 10.1093/ptep/ptac097. URL: https://doi.org/10.1093/ptep/ptac097.
- Raether, H. (Heinz) (1964). *Electron avalanches and breakdown in gases*. ENG. London Butterworth. URL: http://archive.org/details/electronavalanch0000raet.
- Ramsauer, C. and R. Kollath (1929). "Über den Wirkungsquerschnitt der Edelgasmoleküle gegenüber Elektronen unterhalb 1 Volt". en. In: *Annalen der Physik* 395.4. _eprint: https://onlinelibrary.wiley.com/doi/pdf/10.1002/andp.19293950405, pp. 536-564. ISSN: 1521-3889. DOI: 10.1002/andp.19293950405. URL: https://onlinelibrary.wiley.com/doi/abs/10.1002/andp.19293950405.
- Rinnagel, Maximilian Paul (Aug. 2023). "Development of an inverted ring imaging Cherenkov Micromegas". de. Text.PhDThesis. Ludwig-Maximilians-Universität München. URL: https://edoc.ub.uni-muenchen.de/32286/.
- Scharenberg, L. et al. (Mar. 2025). "Towards MPGDs with embedded pixel ASICs". en. In: *Journal of Instrumentation* 20.03. Publisher: IOP Publishing, p. C03025. ISSN: 1748-0221. DOI: 10.1088/1748-0221/20/03/C03025. URL: https://dx.doi.org/10.1088/1748-0221/20/03/C03025.
- Sjue, S. K. L., R. N. George, and D. G. Mathews (Sept. 2017). "Analytic saddlepoint approximation for ionization energy loss distributions". In: *Nuclear Instruments and Methods in Physics Research Section B: Beam Interactions with Materials and Atoms* 407, pp. 270–275. ISSN: 0168-583X. DOI: 10.1016/j.nimb.2017.06.013. URL: https://www.sciencedirect.com/science/article/pii/S0168583X17306882.
- Townsend, John Sealy Edward (1910). The theory of ionization of gases by collision [mi-croform] / by John S. Townsend. English. Type: Book, Microform. Constable London.
- Vogel, Fabian (Feb. 2024). "Long-term irradiation studies of large-area Micromegas detectors for the ATLAS NSW upgrade". de. Text.PhDThesis. Ludwig-Maximilians-Universität München. URL: https://edoc.ub.uni-muenchen.de/33296/.

Acknowledgements

At this point, I would like to thank all the people who supported me during my thesis. A special thanks to:

- Prof. Dr. Otmar Biebel for giving me the opportunity to write my master thesis in his group and for giving me important inputs for my thesis.
- Dr. Ralf Hertenberger for his support throughout the project and for his invaluable inputs and ideas.
- My supervisor Eshita Kumar for the many hours spent on me.
- Dr. Fabian Vogel for his guidance during my thesis.
- I also thank other members of the working group, especially: Dr. Valerio D'Amico, Stefanie Götz, Dr. Alexander Lory, Nick Schneider, Celine Stauch and Dr. Chrysostomos Valderanis.
- I thank all my friends especially Daniel Grewe for all the help I cannot repay and Beatrice Locatelli for the most amazing lunch breaks without whom Garching would have been much more glum, Luca, Sara for all the post-22:00 dinners, Ananya, Avalon, Bhavya, Divya, Rohan, Sofia, Joachim, Farhan, Maerpreet, Manilla, Hamzah and anyone else I missed, for their friendship over the last few years.
- I am most grateful to my parents Jancy PV and Renji Mathew for their enduring support and encouragement and my sister Dr. Jewel Elizabeth for the sisterly wisdom and love.
- My girlfriend Sannia Sajive for all the late night calls and support and love throughout this journey.

Declaration

I hereby declare that this thesis is my own work, and that I have not used any sources and aids other than those stated in the thesis. AI (GPT-40) was used to find synonyms and identify linguistic errors. All improvements and changes were carried out by myself.

Nirmal Renji Mathew

München, den 15. September 2025